The Dissertation Committee for Alán Dávila Leyva
certifies that this is the approved version of the following dissertation:

Jet characterization in Au + Au collisions at STAR

Committee:

Christina Markert, Supervisor

Duane Dicus

Gerald Hoffmann

Sacha Kopp

Karol Lang

Milos Milosavljevic

Jet characterization in Au + Au collisions at STAR

by

Alán Dávila Leyva, B.S.

DISSERTATION

Presented to the Faculty of the Graduate School of

The University of Texas at Austin

in Partial Fulfillment

of the Requirements

for the Degree of

DOCTOR OF PHILOSOPHY

The University of Texas at Austin

May 2013

Dedicated to my mother, María Herminia Leyva Martínez.

Acknowledgments

I am very grateful to my dissertation adviser, Christina. She allowed me to grow as a scientist by providing me with excellent guidance and fomenting constructive debates. It has been a pleasure to be a part of the Relativistic Heavy Ion Physics group at the University of Texas at Austin. Jerry, Jo, Lanny, Drew, Dylan, Martin, Alex, Michael, Kohei, Liang, Prabhat, Liz and Masa where always there to support me when I needed them. My dissertation work was possible thanks to my colleagues at the STAR experiment, some of whom I had the pleasure to meet at meetings, data taking shifts and over the phone.

I would not have started my doctoral adventure if my undergraduate adviser at the University of Texas at El Paso, Jorge, had not given a physics talk at a debate group I belonged to in high school. He has been a great mentor and friend ever since I showed up at his office to ask about a career in physics.

My lunch friends were an important part of my success. Graduate School would not have been as fun without the many lunch hours that ended up with heated conversations about all kinds of topics. Thanks for keeping me in touch with the world outside physics, Rafael, David, Nacho and Erick. I will miss our debates.

I want to thank my father for trusting in me and helping me during my undergraduate studies. My uncle Raul and aunt Lupita who where very supportive while growing up. I want to extend my gratitude to my brothers Marco and Luis. I could not have asked for better brothers. I enjoy seeing how they approach life and I am always learning from them. I also want to thank my mother, she propelled me to where I am with patience, love and encouragement as I was growing up and today.

I am very grateful to Tara, she has been the best companion in the last stretch of the road. I am really looking forward to enjoy the fruits of our hard work together.

Jet characterization in Au + Au collisions at STAR

Alán Dávila Leyva, Ph.D.
The University of Texas at Austin, 2013

Supervisor: Christina Markert

The present study combines modern jet reconstruction algorithms and particle identification (PID) techniques in order to study the enhancement of proton/pion ratio at mid transverse momentum ($p_T \sim$ 1.5 - 4.0 GeV/c) observed in central Au + Au collisions at $\sqrt{s_{NN}} = 200$ GeV. The ratio enhancement is thought to be caused by recombination processes and/or parton fragmentation modification of jets in relativistic heavy ion collisions. The fragmentation modification hypothesis is tested in this analysis by reconstructing and selecting energetic jets presumably biased to fragment outside of the medium created in Au + Au collisions and comparing their particle composition to the recoiling (medium-traversing) jets. The bias assumption is confirmed by comparing jets in central collisions, where the effect of proton/pion enhancement is present, with peripheral ones where no medium effects are expected. The selected jets are reconstructed by using the anti-k_T algorithm from the modern FASTJET package. The PID in the p_T region of interest is possible by combining measurements of the particles' energy deposition and velocity from

the Time Projection Chamber and the recently installed (2009-2010) Time of Flight detectors at STAR. The acceptance of these detectors, $|\eta| < 1.0$ and full azimuth, make them extraordinary tools for correlation studies. These features allow for the measurement of relative azimuth ($\phi_{jet} - \phi_{pion,proton}$) distributions by using the selected jet axis in order to disentangle the uncorrelated background present in the high multiplicity heavy ion collisions. The proton/pion ratios in two different centrality bins and p_T = 1.2 - 3.0 GeV/c are presented for biased (vacuum fragmenting) jets and their recoiling counterparts.

Table of Contents

List of Tables

List of Figures

Chapter 1

Introduction

The Relativistic Heavy Ion Collider (RHIC) was designed and built to look for a new state of matter under extreme conditions of temperature and pressure. This state of matter consists of deconfined quarks and gluons and has been labeled the Quark Gluon Plasma (QGP). Since the inception of RHIC many novel phenomena not present in more elementary collisions (i.e, p + p , $e^+ + e^-$, p + $\bar{p}$, etc.) have been discovered. This section will introduce the reader to some of these observations and the current status of the QGP search.

1.1 QGP

One of the goals of heavy ion physics is to study matter in extreme conditions and search for the formation of a QGP. In a QGP (as predicted by QCD) quarks and gluons are not constrained to neutral color states (like the hadrons seen in regular "cold" nuclear matter) but are deconfined instead. This state of matter could be formed when nuclear matter reaches high enough energy densities. Understanding a QGP could also extend our understanding of the evolution of the universe which might have been in a similar state a few microseconds after the big bang.

Besides heavy ion collisions, QGP can also be formed in neutron stars. Neutron stars can be a dense as 10^{16-17} g / cm^3. Under these conditions of density, the neutrons have to overlap creating what was hypothezised to be a "quark soup" since the 70's [1]. Heavy ion collisions provide us with a way to observe it in the laboratory.

The energy density obtained in Au + Au collisions at $\sqrt{s_{NN}} = 200$ GeV (center of mass energy per nucleon pair) at RHIC is theoretically high enough (assuming a lifetime of the collision of the order of 1 fm/c) to produce such state of matter. Local thermal equilibrium of the quarks and gluons present in the collisions can only be obtained if the mean free path ($\lambda = \sigma\rho$, where σ is the interaction cross section and ρ the particle density) is much less that the total collisional region length traversed by the partons. Normal nuclear matter has a density ~ 0.14 GeV/fm^3 while RHIC reaches a density of ~ 1 GeV/fm^3.

1.2 Experimental Signatures

Proving the creation of a QGP in heavy ion collisions is a challenge. One of the difficulties arises from the short lifetime of the plasma ($\sim 10^{-22}$ seconds). Observable would need to be resilient enough to survive the QGP yet still contain information about the QGP.

The inter quark potential in a QGP (which keeps quarks confined inside color neutral mesons and baryons on regular matter) is modified, this is referred to as potential screening. This screening would split normally bounded

quark-antiquark states. As an example if a bound state made of charm and anti-charm quarks is created in a QGP, both quarks will detach. The J/Ψ meson is composed of a charm and anti-charm quarks pair. The presence of a QGP would leave a signature as a J/Ψ production suppression in heavy ion collisions with respect to its production in p+p collisions at the same energy [2]. Measurements of Au+Au collisions at 200 GeV show such suppression. Nevertheless, p+Au collisions show the suppression as well. This means that the suppression is at least partially due to cold nuclear matter interactions and not just from a possible QGP. For example, the J/Ψ could be dissociating via collisions with the Au nucleons. Measurements by PHENIX showed the suppression of J/Ψ production in Cu+Cu collisions and compared it with p+p. An attempt was made to take into consideration the cold nuclear matter contribution to the suppression via fits to d + Au data. This analysis implies that the suppression of J/Ψ can be explained by cold nuclear matter effects for all but the most central collisions [3].

Another signature of QGP formation is the enhancement of particles with strange quark content. Strange quarks are more copiously produced than up or down quarks in an equilibrated QGP. This increase in strange quark production (in comparison to a QGP free p+p collision) can induce more hadrons with strange quark content production at hadronization. Measurements of particle production scaled by the reciprocal of the number binary collisions in Au+Au and p+p collisions at the same energy provide information about strange quark production enhancement. Enhancement of k^0_s, Λ and $\bar{\Lambda}$ has been

reported in 200 GeV Au+Au and Cu+Cu collisions [4]. This is not a definite signature of QGP formation due to the fact that the enhancement can be due to either an increase of strange quark production in heavy ion collisions or a decrease of strange quark production in p+p collisions [5]. Nevertheless, it might be harder to conserve strangeness in the p+p collision small "volume" and this would lead to a suppression of strangeness in p+p collisions. This is due to a lack of sufficient phase space for strange quark production in such a small volume.

A third signature of possible QGP formation is jet quenching where a jet is a collimated spray of hadrons produced from a scattered parton (quark or gluon). A hard scattered parton drifting through a QGP could lose energy by colliding with other quarks and gluons and/or by radiating gluons in the colored medium. This collision and radiation loses would decrease the parton's (jet) final energy. This in turns would have an impact on particles production (modified fragmentation). Among the signals to be expected from such a scenario are the disappearance of signal from back to back jets on the medium traversing side and suppression of binary scaled high p_T particles spectrum. Both signals are observed in heavy ion collision at RHIC as will be further discussed on section 1.6. The amount of suppression depends on the processes cross section and medium density as well as the length of the medium traversed. It is worth nothing that the suppression of hadronic particles production at high p_T hints to a modified fragmentation function or recombination scenarios but does not by itself imply thermalization or creation of a QGP.

According to the 2005 assessment of the evidence of QGP formation on RHIC collisions, it was premature to conclude that QGP had been formed in the laboratory [6]. The conclusions from the heavy ion collisions community by the end of 2012 were that there are hints of the hadronic matter transition to a QGP. These hints were explained to mean that the interpretation of the results that led to the conclusion that QGP was indeed produced at RHIC remains open to questions [7]. The case for continuation of RHIC operations stated that, collectively, the elliptic flow measurements in heavy ion collisions, yield and flow of meson and baryon scaling with number of constituent quarks, hydrodynamic models fits to photon production and particle jets quenching have established that RHIC collisions have produced deconfined QGP matter that behaves like a nearly perfect fluid [7].

Relativistic heavy ion collisions show clear deviations from simple p+p binary scaling. There are many new phenomena that emerged from heavy ion collisions. Nevertheless, a definite measurement that proves without reasonable doubt that QGP has been formed at RHIC is still pending.

1.3 Kinematic Observables

Relativistic heavy ion collisions are produced by steering beams of particles into a collision region. A coordinate frame can be built by taking the beam directions as the z axis and a plane whose normal is in the beam direction as the transverse plane. The momentum of any particle produced in a collision can be decomposed into a longitudinal part (parallel to the beam axis) and

a transverse part (projection of the momentum in the transverse plane). The information of a particle's momentum is often registered by measuring the transverse momentum or p_T, the polar angle (angle of the momentum with respect to the beam axis) and the azimuth angle of the particle. The azimuth angle is the angle between an axis in the transverse plane and the direction of the particle projected in that plane.

A widely used variable in particle physics is the pseudorapidity. The pseudorapidity of a particle is related to its polar angle and it is equivalent to the rapidity on the high energy limit ($p >> m$). The rapidity of a particle is defined on Eq. 1.1. It is an analog to velocity (actually, rapidity approaches the longitudinal velocity in the limit of non relativistic energies) that has the nice property of being modified by an additive constant under Lorentz transformations. An important feature of the rapidity (and pseudorapidity) is that the rapidity distribution of particles coming from a collision does not change under a longitudinal Lorentz boost. Therefore, the pseudorapidity distributions can be measured either in the center of mass frame or in the lab frame (modulo a shift in the rapidity variable) [8].

$$y = \frac{1}{2} ln \left(\frac{E + p_z}{E - p_z} \right) \tag{1.1}$$

The precise measurement of a particle's rapidity requires knowledge of its species. Since this information is not always available the pseudorapidity defined by Eq. 1.2 is used instead. For a particle whose momentum direction

has an angle θ relative to the beam, the pseudorapidity (η) is related to it by Eq. 1.3. This relationship is important as it is usually easier to measure a track's angle relative to the beam than to identify its mass (species) [8].

$$\eta = \frac{1}{2} ln \left(\frac{|p| + p_z}{|p| - p_z} \right) \tag{1.2}$$

$$\eta = -ln \left[tan \left(\theta / 2 \right) \right] \tag{1.3}$$

1.4 Centrality in Heavy Ion Collisions

The notion of centrality is widely used in the study and characterization of heavy ion collisions. Centrality refers to a classification of heavy ion collisions into classes that represent a given percentage of the total cross section of the reaction. The metric for classification is the number of charged particles produced in the collisions. It is further assumed that each class corresponds to a degree of overlap of the colliding nuclei. In this way, a high multiplicity collision represents a head on collisions and a low multiplicity one represents a peripheral (or glancing) collision.

Glauber models attempt to create the correspondence between geometrical aspects of the collision with collision's observables. The nuclear charge densities (measured in electron scattering experiments) have to be specified for any Glauber calculation as well as the nucleon-nucleon inelastic cross section at the energy of interest (for example, it is ~ 42 mb at $\sqrt{s_{NN}} = 200$ GeV). The

nuclear charge density used for Au nucleus at RHIC is a Fermi distribution. The model to calculate the number of produced particles in a given collision using the Glauber model assumes that the nucleons in the nucleon follow linear trajectories and are not deflected after a collision [9].

There are two distinct Glauber models, the optical limit and the Monte Carlo Glauber. In the optical limit the density function of the colliding nucleus and the impact parameter are used to calculate a so called thickness function. This function is the integral of the densities in the overlapping area of the collision. Multiplying this function by the inelastic nucleon-nucleon cross section gives the probability of having any two nucleons colliding. If the given colliding nucleus have A and B nucleons respectively, the probability of having N nucleon-nucleon collisions is represented by the Binomial distributions taking N pairs out of AB (all pair of nucleons possible). The probability of interaction of both nuclei is just the sum of the probabilities of having 1 to AB nucleon-nucleon collisions. The average number of nucleon-nucleon collisions (N_{bin}) and number of wounded or participant nucleons (N_{part}) can be derived from this probability [9].

The Monte Carlo Glauber model generates nucleons' positions by using the two colliding nuclei density distributions. An impact parameter is picked and then the two nucleus are made to "collide" by assuming the nucleons have straight trajectories. A collision happens whenever two nucleons from different nuclei are separated by a distance smaller than the radius of a circle of area equal to the nucleon-nucleon inelastic cross section. Many such collisions are

simulated and the average N_{bin} and N_{part} are computed [9].

The last part to complete the Glauber model is to find the relationship between the number of binary collisions and/or number of participants and the real events' multiplicities. The strategy consists on measuring the distributions of the number of charged particles in an event ($N_{charged}$) from the data and calculate it from the Glauber model. The distribution is divided in centrality classes, which are defined to be some percent of the total inelastic cross section of the collision. Corresponding centrality classes can be matched between data and Glauber model. The average impact parameter, number of binary collisions and number of participants in each Glauber class is assigned to the corresponding data class [9].

The present analysis will not be concerned with the specific number of collisions in the centrality classes used in it. The collisions(events) are divided in two centralities. The 0-20% most central collisions (head on like) and the 20-80% most central collision (mid peripheral to peripheral). Comparisons of particle production among those two classes will be presented.

1.5 Jets

A jet is a narrow spray of particles produced via fragmentation (splitting) of a gluon or quark (both of which are called partons). Back to back jets are created in elementary high energy collisions and nucleus - nucleus collisions via parton - parton hard scatterings.

1.5.1 Theory

A jet can be defined at the parton level (a gluon or quark coming out of a hard scattering is a jet) and at the hadron (or experimental) level. The reconstruction of the total four momentum of the jet's hadrons should ideally give back the four momentum of the original parton that fragmented into them. A good jet definition involves a jet algorithm and some resolution parameter. The algorithm gives a recipe for clustering particles into the jet and the resolution parameter gives a cut off distance (whose definition depends on the algorithm too) to cluster a hadron into a jet. An important feature for a jet algorithm is that it should not change the jet's cross section in the presence of infinitely soft extra particles in the event or if a massless parton is replaced by two massless collinear ones. These two features make the algorithms amendable to theoretical computations [10]

1.5.2 Algorithms

As described above, a jet algorithm is a well defined set of rules that takes a set of particles onto a set of jets [11]. There are many different jet finding algorithm in the literature. The FASTJET C++ package includes most of them. Among the different algorihtms that can be chosen there are two main categories: sequential recombination and cone algorithms. The former uses a distance metric and sequentially merges particles (tracks, or towers) into clusters until some cut off criteria is achieved. The cone-like algorithms use a geometrical angular distance to cluster the particles into jets [11].

The jet finding algorithm of choice in the present work is the $Anti-k_T$ algorithm. A distance is defined as in Eq. 1.4 where p_{Ti} is the transverse momentum of the i^{th} particle present on the event where we are trying to find the jets, ΔR_{ij} is defined as $R_{ij}^2 = (\phi_i - \phi_j)^2 + (\eta_i - \eta_j)^2$, and R is the "radius" parameter. A distance of each particle (or cluster) with the beam is also defined as $d_{iB} = p_{Ti}^{-2}$. The minimum of the distances of every particle with respect to every other particle in the event is found. If it corresponds to a d_{iB} then that particle is labeled as a jet and removed form the particles' list, otherwise, the i and j particles from the minimal distance are merged. The way the particles are merged is called the jet algorithm scheme. The E-scheme uses a simple 4 momentum vector sum assuming masses = 0 and it is the scheme used in the present analysis. This procedure is repeated until all particles in the event have been promoted to jets.

$$d_{ij} = d_{ji} = min(p_{Ti}^{-2}, p_{Tj}^{-2}) \frac{\Delta R_{ij}^2}{R^2} \tag{1.4}$$

1.5.3 Jets in Heavy Ion Collisions

The purpose of doing full jet reconstruction (instead of using high p_T hadrons as proxy) is to study jet quenching with a well calibrated probe that can be directly compared to p + p collisions. Jet quenching refers to the phenomenon by which a jet looses some of its initial energy by interacting with the medium created in Au + Au collisions. A difficult task for jet-medium interaction studies is to select a jet population using a jet finding algorithm

that does not bias the jet population even in the presence of quenched jets. This is important for analysis that look for signals of jet quenching in the jets p_T distributions [12].

The study of heavy ion collisions by jet reconstruction at STAR has evolved over the past few years. The main systematic for precise jet energy reconstruction at RHIC energies is the smearing of the jet's energy due to the uneven (in $\eta - \phi$ space) heavy ion background.

The FASTJET jet finding software package implementation was developed having the LHC in mind. As a result, it includes event by event background characterization techniques that were designed for pile up subtraction in jet reconstruction in p+p collisions at the LHC. The background estimation techniques turned out to be useful in the heavy ion collisions' environment as well. The background in heavy ion collisions consists of particles produced from soft processes or other jets that land in close proximity to the jet axis in $\eta - \phi$ space. A background subtracted jet will still suffer from smearing due to non uniformity of this background. One way to avoid these jet energy fluctuations is to apply a cut on the p_T of the tracks used for jet reconstruction. This cut comes at the price of biasing the selected jet population [13].

There are different ways to measure jets and each measurments comes with its own bias. Instead of a low p_T track cut at reconstruction, the jets can be required to have a high p_T track(or tower) among its constituents. The distortion in the fragmentation of this jets is expected to be minimal [14]. The heavy ion collision background is estimated by defining a background density

measure. This density is obtained by calculating the median of the distribution of the ratios $\rho = p_{T,jet}^{reco}/A_{jet}$ on an event by event basis. The variable A_{jet} is the area of a given jet in the event [15] and $p_{T,jet}^{reco}$ is the jet's transverse momentum. The transverse momentum of the reconstructed jets are background corrected as shown on Eq. 1.5. The resulting jet population still suffers from a smearing produced by the heavy ion background fluctuations. The magnitude of the fluctuation can be estimated by embedding a known probe into a real Au + Au event and computing $\delta p_T = p_T^{meas} - \rho A_{jet} - p_T^{embed}$. Fortunately, the irresolution measure is independent of the fragmentation pattern of jets. Therefore, the irresolution can be used to deconvolve the measured p_T^{jet} and recover the original(un-smeared) jet distribution [12].

A recent data driven study with a toy Monte Carlo model for the heavy ion background and using embedded PYTHIA jets demonstrated the feasibility of the jet reconstruction described above. The toy Monte Carlo model consisted of jets embedded in a thermal background with $\langle p_T \rangle$= 500 MeV/c. For the deconvolution of the smeared distribution to recover the original one, the jets had to be biased to include a 4 GeV/c track on them. Once this is done, the ratio of the original to deconvoluted jet p_T distributions agreed to within 10% [14]. Another option to study jet quenching is to trigger the Au + Au events by a high p_T track and looking at the recoiling jet distribution. The recoiling jet's fragmentation is then free of the trigger bias. Any change in its fragmentation can be attributed to medium-jet interactions. The recoiling jet is usually accepted in a $\phi_{hadron} - \phi_{jet} - \pi < \pi/4$ window. The per trigger jet

distributions are then analyzed [14].

$$p_{T,jet}^{measured} = p_{T,jet}^{reco} - \rho A_{jet} \tag{1.5}$$

A more indirect but effective way to study jet fragmentation in heavy ion collisions consists of measuring jet-hadron $\Delta\phi = \phi_{jet} - \phi_{hadron}$ distributions for different track p_T bins. The distributions in 200 GeV p + p collisions or 200 GeV peripheral Au + Au collisions are compared to central Au + Au collisions. The jets are reconstructed by cutting out all particles below 2 GeV/c (to avoid background fluctuations) and are also required to have a tower with $E_T > 5$ GeV on them (to bias the trigger population to the surface). The highly triggered jets from p + p collisions embedded in minimally biased Au + Au collisions have comparable p_T distribution to the triggered jets in Au + Au events. A model function is used to fit the $\Delta\phi$ distributions and extract jet yields for the trigger and recoiling jet. This studies have already been used to show that the recoiling jets (medium-traversing) suffer form associated hadron's high p_T suppression accompanied by low p_T enhancement [16]. The methodology just describe is very similar to the one used in this thesis. The novel feature included in the present analysis is the use of particle identification to study possible jet composition modification in the presence of the heavy ion collisions environment.

1.5.4 Jet hadro-chemistry

Among the motivations to study jet's particle composition at RHIC are the predictions that jet-quenching at LHC can induce modifications on the jets fragmentation. Jet quenching has also been observed in Au + Au collisions at RHIC and it is natural to ask whether the fragmentation has changed as well. A model where the parton splitting functions are modified to account for parton - medium interactions predicts that the p/π ratios for E_T = 50 GeV jets at LHC energies can be enhanced by a factor of 2 compared to the vacuum fragmentation reference Fig. 1.1 shows particle ratios for jets of different energies on top of a Pb + Pb at $\sqrt{s_{NN}}$ = 5.5 TeV background with and without modified fragmentation function. The background is simulated by a hadron distribution consisting of a an exponential at low p_T and a power law at high p_T [17, 18].

1.6 Hard Probes results from RHIC

One of the most exciting discoveries at RHIC was the suppression of π^0 production at p_T >2 GeV/c in central Au + Au collisions. The suppression is measured by taking the ratio of the p_T distribution in Au + Au collisions with respect to the distribution in p + p collisions at the same energy but scaled by the number of binary collisions present in Au + Au. The suppression is contrasted with direct gammas (produced in the collision and not via π^0 decays) production where no suppression is observed (see Fig. 1.2). The direct gammas are not expected to interact strongly with the quarks and gluons.

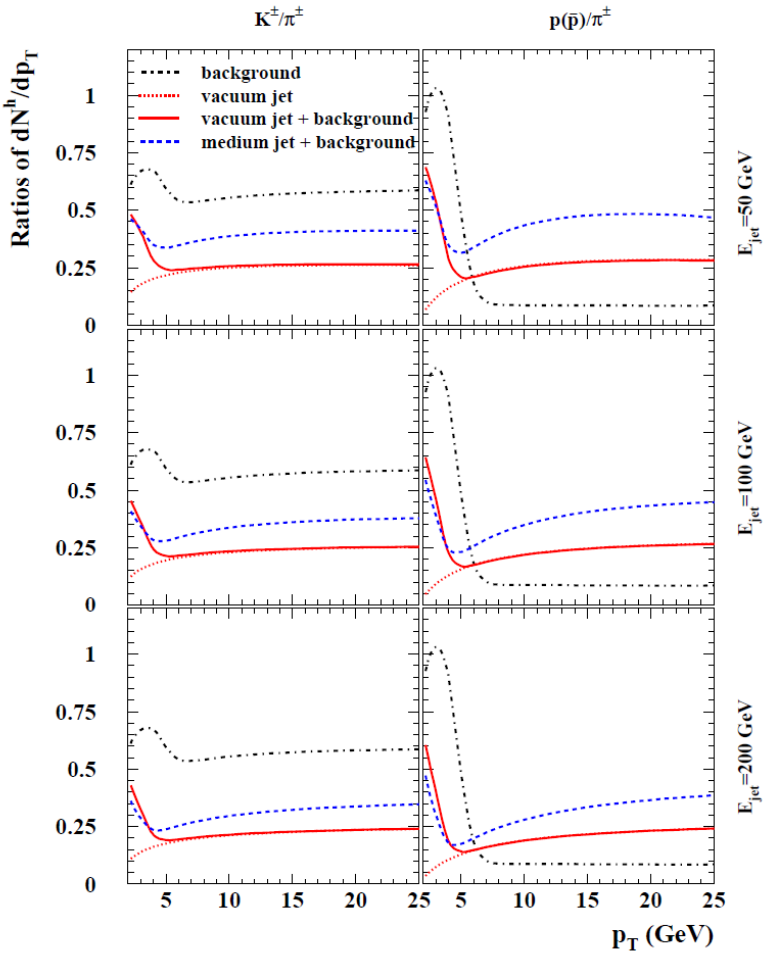

Figure 1.1: Particle ratios on jets of different energies present in $\sqrt{s_{NN}} = 5.5$ TeV Pb+Pb collisions. The $K^{\pm}/\pi^{\pm}$ and $p(\bar{p})/\pi^{\pm}$ ratios get enhanced in the presence of medium-induced fragmentation modification.

This is further evidence that the pion suppression is probably due to parton - medium interactions [19]. Regardless of which kind of medium might be present on Au + Au collisions, this result shows that there is some strong force interaction happening in Au + Au collisions that does not correspond to a simple linear superposition of p+p collisions.

Another measurement that demonstrates the interaction of hard scattered partons in the Au + Au collisions medium is the back to back signal from two particle azimuth correlations. A clear jet's signal around $\Delta\phi \sim 0$ and $\Delta\phi \sim \pi$ is observed in p + p events and d + Au events while the peak at $\Delta\phi \sim \pi$ disappears in central Au + Au events (at $\sqrt{s_{NN}}$ 200 GeV). Fig. 1.3 shows the jet's signals for the three collision systems. This measurement indicates that the recoil jet signal suppression is a final state effect and not due to cold nuclear matter or the Cronning effect [20].

1.7 Enhancement of p/π ratio in central Au + Au collisions

The particles' production mechanism in heavy ion collisions can be tested by measuring the p_T dependent particle ratios. The enhancement of p/π ($\bar{p}/\pi^-$) at intermediate p_T and mid-rapidity was observed for the first time in central $\sqrt{s_{NN}}$ = 130 GeV Au+Au collisions [21]. This enhancement is not present in p+p collisions for a wide range of energies. Measurements at PHENIX have shown that the p/π ratio increases with p_T up to $\sim$ 3.0 GeV/c in the 0-10 % most central Au+Au collisions while it increases and saturates with

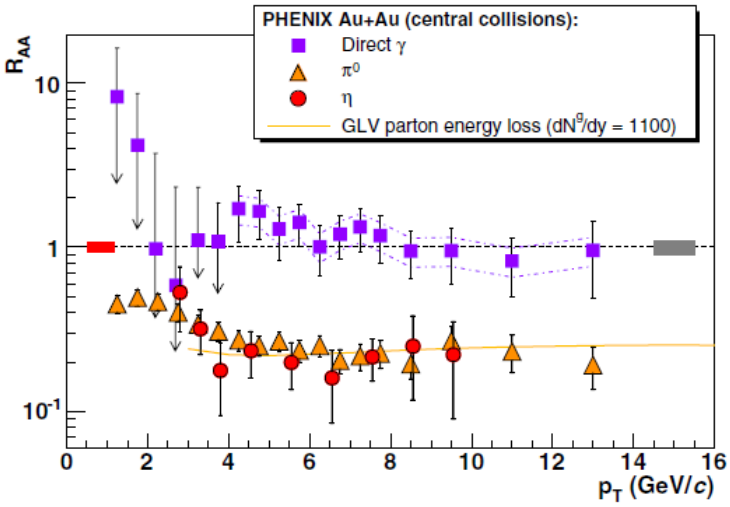

Figure 1.2: Nuclear modification factor (R_{AA}) for π^0 and η mesons and direct γ's. There is a meson production suppression in central Au+Au collisions (taken form [19])

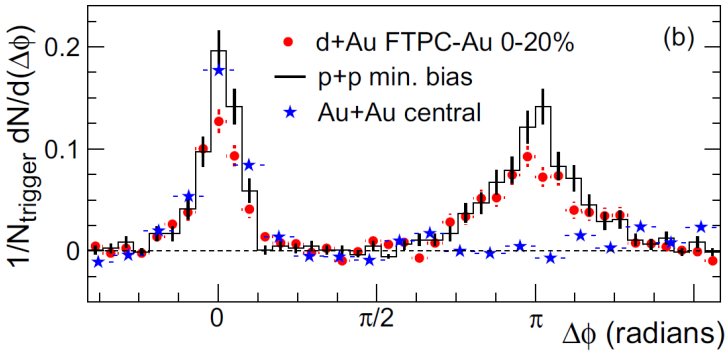

Figure 1.3: $\Delta\phi$ distribution of associated particles ($2 < p_T^{assoc} < p_T^{trigger}$) with respect to a high p_T trigger ($4 < p_T^{trigger} < 6$ GeV/c). The suppression on the recoiling side for central Au+Au events is clearly seen

a value ~ 0.4 at $p_T \sim 1.5$ GeV/c in the 60 - 92 % centrality [22]. The fact that the ratio of central over peripheral binary scaled p_T spectra (R_{CP}) of protons is close to 1 in the p_T range of $\sim$ 1.5 - 4.0 GeV/c suggests that protons are either less suppressed than pions or that protons are more copiously produced in central Au + Au collision than what is expected from fragmentation [22].

The p/π measurements were extended to a higher p_T by the STAR collaboration, reaching the region where particle production is dominated by jet fragmentation ($p_T \geq 6$ GeV/c) [23]. The new measurements showed the complete p_T neighborhood where the unexpectedly high p/π is found. The p/π ratio gets enhanced at intermediate p_T (1.5 - 4.5 GeV/c) in 0-12 % most central Au+Au collisions compared to peripheral (60-80%) and d+Au collisions at $\sqrt{s_{NN}}$= 200 GeV. The ratio peaks at $\sim 2-3$ GeV/c in central Au+Au and then decreases to approach the value measured in peripheral and d+Au collisions at about $p_T = 5$ GeV/c. The fact that the p/π ratio is the same at this high p_T suggests that the hadron production mechanism is the same in central and peripheral collisions and that the partons fragmenting into the final state proton and pion lose the same amount of energy while passing through the medium in central Au+Au collisions.

There have been attempts to explain the p/π anomalous enhancement by coalescence or recombination models and partonic energy loss effects on the p and π spectrum [24–26]. According to some studies [25] parton recombination is the predominant mechanism for hadron production if the partons follow a thermal distribution. As soon as the distribution becomes a power

law, fragmentation dominates. This recombination model predicted a decrease in p/π ratio at $p_T \sim$ 4-5 GeV/c and saturation afterwards since the fragmentation processes are expected to take over. The predictions were confirmed by experiment [27]. A very similar coalescence model [24] proposes that it is the coalescence of minijet partons with thermal quarks what causes the anomalous p/π enhancement seen in central Au + Au colisions. The $\bar{p}/\pi$ ratio in central $\sqrt{s_{NN}}$ = 200 GeV Au+Au collisions is well described up to p_T = 4.0 GeV/c with a suitable choice inverse slope parameter for the intermediate thermal antiprotons. The same coalescence model predicted an increase (decrease) of p/π ($\bar{p}/\pi^-$) at intermediate p_T when going from 200 to 62 GeV [28]. STAR measurements to date confirm the general trend of the predictions of the coalescence and recombination models but show quantitative disagreement [29]. Another possible cause of the p/π enhancement is the effect of parton energy loss on the hard component of particle spectrum of Au+Au collisions. The measured spectra can be described by a soft (scaling with number of participant pairs) + a hard (scaling with number of binary collisions) components. The hard part is isolated and its modification with respect to N_{bin} scaling is related to a negative boost in the hard component hadrons' p_T. The modification of the hard component shows up as an increase of protons in the p_T region of p/π enhancement [26].

The study presented in this thesis attempts to improve our understanding of the production mechanism giving rise to the p/π enhancement by studying this ratio in a vacuum fragmenting jet and a medium traversing one. This

will allow us to look for medium modification effects on the p/π ratio. We will study 0-20 % most central Au+Au collisions at $\sqrt{s_{NN}}$ = 200 GeV and compare the particle production in the direction of a surface bias (near side) jet and its recoiling partner (away side) in the p_T region where the p/π ratio peaks.

Chapter 2

RHIC

The RHIC accelerator has the capability of colliding protons as well as heavy ions. Reactions of p+p , Au+Au, Cu+Cu and U+U at relativistic speeds have been produced at RHIC. The energy range for Au+Au collisions extends from $\sqrt{s_{NN}} \sim 7$ GeV to 200 GeV. Protons have been collided with energies as high as $\sqrt{s_{NN}} = 500$ GeV. RHIC is versatile enough to produce asymmetric collisions as well. RHIC has successfully produced d+Au and Au+Cu collisions.

2.1 Facility

The Relativistic Heavy Ion Collider is a particle accelerator located at Brookhaven National Laboratory (BNL), Upton, New York and it is funded by the U.S. Department of Energy's Office of Science [30].

RHIC's circumference is 2.4 miles [30] and has 1740 superconducting magnets (for focusing and steering the ions or protons beams). The superconducting magnets have to be cooled to a temperature of -452 F° (4.3 K°) by liquid helium [31,32].Beams of ions (or protons) circulate in opposite directions in the beam pipe. The bean is made up of at most 111 bunches of ions. Each

bunch has $\sim 10^9$ ions and they are made to collide at a crossing rate of ~ 80 kHz [32].

The heavy ions have to go trough a series of accelerating stages before they can be injected into RHIC.

2.1.1 Linac

The Linac is Brookhaven's linear accelerator. It is 144.8 meters long and it is used to acceletare protons from a pre-injection energy of 0.75 MeV to an output energy of 200.3 MeV and a 100 mA peak beam current [33].

The protons are produced in a pulsed duoplasmatron. A duoplasmatron consists of a chamber where plasma is created and ions are accelerated through a small aperture by means of electric fields. The part of the chamber preceding the small aperture has a conical shape. Hydrogen gas is leaked into the chamber that contains a heated filament cathode which is heated to 900° C and expels electrons. The chamber's small aperture is at high positive potential and the whole chamber is surrounded by a solenoid magnet. The magnetic (B) field created by this magnet is parallel to the chamber walls. The electrons follow a helix path around the B field lines while traveling toward the tip of the chamber where the electric field gets concentrated. The electrons ionize hydrogen atoms inside and at a region just outside of the chamber as they traverse it. More electrons are concentrated at the tip of the chamber and hydrogen ionization is maximized in that region producing a highly dense plasma there. A cylindrical electrode at a very negative voltage extracts the positive

charged ions (protons) from the high concentration of plasma and accelerates them. The beam of (now) protons is 250 mA at this stage and has energy of 750 KeV. The beam is already pulsed instead of continuous at this stage with a frequency of 10 Hz and pulse width of 250 μsec [33, 34].

The protons being generated at the duoplasmatron are accelerated by a pre-injector (Cockcroft-Walton generator) and then they are taken to the Linac. The Linac is a drift tube accelerator that has 9 different accelerating cavities of cylindrical shape and $\sim$ 278(18) full (half) drift tubes of varying lengths [33]. The cavities are powered with RF power supplies and maintain an electromagnetic wave guide inside them traveling along the pipe. The drift tubes serve as shielding for the proton beam when the time varying electric field points in the direction opposite of their travel. Each time a beam pulse passes through a gap between drift tubes it experiences the cavities' field. The axial electric field is synchronized so that the protons feel an accelerating force when they traverse the gaps. Each drift tube contains a focusing quadrupole and each cavity has additional 4 quadrupoles for beam focusing. The cavities operate at a 200 MHz [33]. The Linac's beam tube has to be mantained at a 10^{-8} torr vacuum.

The protons that successfully exit the Linac have a final energy spread of $\pm$ 1% at 200 MeV and beam pulse length and rate of 200 μsec and 10 Hz [35].

2.1.2 EBIS

RHIC was upgraded on 2012 with an electron beam ion source (EBIS) for the production of the Au ions beam. The upgrade was necessary in order to achieve higher luminosities by dispensing the use of electron-stripping foils. Besides sparing the foils, EBIS has the advantage of producing different ion species (He to U). U+U collisions on Run 12 (year 2012) were possible due to this upgrade. The EBIS can change ion species on a pulse by pulse basis. This allows to fill the accelerator with different ion species bunches on the clock-wise and counter clock-wise accelerator drift tubes. Au-Cu collisions were achieved this way on Run 12 as well [36].

The EBIS consists of and electron gun, solenoid, drift tubes and ion trap chamber, electron collector, ion injection systems and ion extractor. Low charged ions are produced on an external ions source (i.e. Hollow Cathode Ion Source) and then are injected to the EBIS for further ionization and acceleration.

A beam of electrons is made to traverse the cylindrically shaped ion trap in the EBIS and it is collected afterwards. The chamber has several drift tubes in it and it is maintained at a high vacuum. There are anodes at both ends on the traps to generate a potential barrier and keeps the ions inside. The energetic electron beam still makes it out of the trap. Previously produced, low charge, ions are injected to the trap on the opposite side to electron beam injection. The electron beam further ionizes the ions (from Au^{+1} to Au^{+32} at RHIC) and the space charge produced by the electron beam provides a radial

potential that keeps the newly created ions confined. After a few ms, there are highly ionized atoms in the middle of the electron beam inside the trap. The ions are then extracted by increasing the potential in the ion trap at each drift tube sequentially. The changing potential pushes the ions outside of the trap at the lower potential end. Varying the rate at which the potential in the drift tubes is modified allows to control the pulse time spread and makes the beam's energy spread smaller compared to just lowering the potential at the end of the trap to let the ions escape [37].

The EBIS electron gun can provide a beam current up to 20 A. The electron beam current density required to ionize heavy nuclei is high (i.e. $\sim$ 600 A/cm^2 for U^{+45}) [38]. The gun is designed to have a convex cathode followed by a 37.5 kV anode for electron acceleration and it is surrounded by its own solenoidal coils that provide a B field independent of the main ion trap magnetic field [39].

The EBIS ion trap is maintained at a $\sim 10^{-9}$ torr pressure and can capture up to 10^{12} charges at a time. A superconducting solenoid surrounding the ion trap provides a 5 Tesla axial magnetic field that focuses the electron beam in the middle of the trap. The chamber is 1 m long and the trapped ions confinement time used is $\sim$ 30 ms. The way the EBIS was designed at RHIC provides good control over the pulse width as well as fix charge extraction that are crucial for injection at the Booster [36].

The ion beam that exits the EBIS contains 3.4 x 10^9 Au^{+32} ions on pulses of 10-40 μsec width for a beam current of 1.7 - 0.42 mA and have

an energy of 17 keV/u. The beam extracted from the EBIS is directed to a 100 MHz, 3 m long radio frequency quadrupole that provides bunching , focusing and acceleration. At this stage, the ions have an energy of 300 keV/u. Afterwards, the beam is passed trough the Linac before it is injected to the Booster with an energy of 2 MeV/u. [36]. The beam pulses before injection are now down to 2.7 x 10^9 ions. The energy spread is $\pm$ 2 keV/u and the pulse remains the same as the onde produced at the EBIS [36].

2.1.3 Booster

The Booster is an accelerator that was originally built to increase the proton beam intensity, the mass number of the ions that can be accelerated and the injection energy at the AGS (Alternating Gradient Synchrotron) . It now serves the purpose of ramping up the energy of the ions coming from the EBIS for injection at the AGS. The Booster is a synchrotron accelerator with a total of 36 dipoles and 48 quadrupoles, with a circumference of 201.78 m. The protons (ions) get accelerated in about 60 (620) ms. The Au ions are ejected from the Booster completely ionized (charge of +79) and with an energy of 95 MeV/u. The stripping foil used to detach the last remaining electrons from the Au ions consists of cooper 70 mg/cm^2 and is placed in the transfer line between the Booster and the AGS. The number of particles per bunch after acceleration in the buster is of the order of $\sim 10^9$ [40].

2.1.4 AGS

The AGS is bigger than the booster with a circumference of half a mile. It was the most energetic proton accelerator in the world until 1968. Its beam bending magnets produce magnetic fields on the range of 1.2 x 10^{-2} - 1.3 T during the injection-acceleration-ejection phases. The beam circulates in a vacuum chamber (tube) at $\sim 10^{-6}$ torr. The vacuum chamber consists of 12 different divisions with four high vacuum pumping stations each. The AGS design takes advantage of the alternating grading principle [41].

The alternating grading focusing principle states that particles close to a idealized stable orbit on an circular accelerator can be made to oscillate in proximity to that orbit by employing alternating focusing and defocusing elements. The focusing forces in an alternating gradient synchroton are bigger and therefore the betatron oscillation amplitudes are smaller. Betatron oscillations are deviations with respect to an ideal equilibrium orbit on a plane transverse to the beam direction that travels with the beam [42]. The AGS betatron oscillations per revolution are 8 - 0.75 compared to less that one for previous synchrotrons [41] allowing for smaller beam pipe cross sections and magnets.

Particles injected into this kind of accelerators are maintained in orbit by focusing forces due to the magnetic field gradients. The gradients are characterized by an index defined as n = -(r/B)($\partial B/\partial r$) where B is the dipole magnetic field and r is the particles' radius of curvature [42].

Defining y and x as the local vertical and horizontal directions on a moving frame that travels with a particle following an ideal equilibrium orbit in a synchrotron an increasing r corresponds to higher values of x. If negative values of x are taken to point towards the center of the accelerator then a positive value of n implies that the y component of the B field increases with increasing x. Therefore, the further away a particle is from the ideal trajectory the greater is the push to keep it away (defocussing). On the other hand, the x component of the B field also increases as the particles' orbit deviates towards positive y values. The force exerted on these particles pulls toward the stable orbit (focusing). If n changes sign the situation is reversed. A net effect of focusing in both directions can be obtained by alternating n between high negative and positive values [42]. This principle works since particles are further away from the equilibrium orbit in focusing sections that in defocussing sections [41].

The AGS also accelerated the bunches injected into it. The acceleration of the particles is done by 12 RF accelerating cavities that have two gaps where a potential difference increases the kinetic energy of the the traversing particles. The voltage gain at each gap is 4 keV for a 90 keV gain per revolution in the synchrotron [41]. The cavities have drift tubes inside them so that the protons(or ions) are shielded from any electric and magnetic field while traversing them. The beam thus only experiences the accelerating electric field while traversing the gaps as in the Booster and Linac. The RF of the accelerating cavities has to be modulated so that the protons see and accelerating

field at each gap and to keep up with the protons increasing velocity. The higher the velocity the higher the frequency has to be so that the particles keep coinciding with an accelerating potential at each gap. The frequency of the cavities varies from 1.4 to 4.46 MHz during the accelerating cycle [41].

The amount of energy gained at each gap depends on the phase difference between the RF signal and the time at which a given proton reaches the gap. The phase difference stable point at AGS is chosen to be 30° [41]. A proton that arrives at a time such that the phase difference is slightly bigger than 30° will get accelerated more that a proton in that stable phase. It will travel around more quickly and will arrive with a phase difference below 30° next time it goes through the gap. At this time the proton will get less forward acceleration than a proton in the stable orbit. This results in a back and forth motion in phase (or relative time of arrival) and energy difference around the ideal stable orbit. This motion is called the synchrotron oscillations.

For a particle arriving with a slightly greater than the stable orbit phase the radius of the orbit will also increase. At low velocities (compared to the velocity of light) the increase of the path length is not important. Small oscillations in the particles' orbit are desired so that particles do not consistently pass through the same imperfections that could be present in the magnets. If there is place in the beam trajectory where the magnetic field is distorted a particle traversing it every cycle could get an undesired kick and drift out of orbit.

The injection energy of 50 MeV is increased to a ejection energy of 30

GeV for protons being accelerated at the AGS [41].

2.1.5 RHIC

RHIC began operations in the year 2000. It was built with two identical rings of super conducting magnets separated by 90 cm from each other with 6 intersection sections where each ring's beam is deflected for collisions. It is capable of accelerating protons and different ion species all the way up to Uranium to 100 GeV/u of center of mass energy . Gold ions are accelerated from an initial injection kinetic energy of 10.8 GeV per nucleon while protons increase their kinetic energy from 28.3 GeV up to 250 GeV/u [43].

The beam is injected on pulses coming from the AGS and it remains bunched at RHIC. There are usually 60 - 110 (120) bunches at each ring for gold (proton) storage [43]. The disparity for ions is due to the fact that they have a higher intra beam Coulomb scattering interaction so bunches spread more. The luminosity of the accelerator is proportional to the number of particles in each of the colliding bunches to the circulating frequency and inversely proportional to the beam transverse size. The number of gold ions (protons) per bunch is 1.0 x 10^9 (1.0 x 10^{11}) [44]. The beam transverse size is $\sim 15\mu m$ [43]. The longitudinal beam size and energy spread is also important to maintain the bunches close to the stable orbits around the accelerator. The bunch size changes as the particles get accelerated and the frequency of the RF cavities increases. The gold bunch size at injection is 5.62 meters with an energy spread of ± 1.49 x 10^{-3}. The proton bunch's size at injection is 2.58 m

and the energy spread is ± 1.26 x 10^{-3}. At top energy (200 GeV/u) the bunch has been reduced to 0.19 (0.1) m for gold ions (protons), and the energy spread lowered to ± 1.49 x 10^{-3} (± 0.83 x 10^{-3}) for gold (proton) [44]. The luminosity for heavy ions runs to be used in this analysis is of the order of 10^{26} - 10^{27} $cm^{-2}s^{-1}$ [43].

At RHIC energies, particles' momentum is so high that it is necessary to use superconducting magnets to keep the radius of curvature within a reasonable achievable size. The dipoles and quadrupoles are made with coils of Nb-Ti alloy cable. This alloy becomes a superconductor below 9.2° K. All the magnets are maintained below their nominal operating temperature of 4.6° K via a helium refrigerator. The cool down procedure to reach operational temperature takes about 17-18 days [44]. The maximum magnetic field that the dipoles generate, for example, during 100 GeV/u acceleration, is 3.45 T [43].

The quadrupoles produce non-uniform magnetic fields for beam focusing; they produce a B field gradient of 71 T/m during beam transit at top energy using a current of 4.72 kA (or about 1/7 of the average current on negative lightning).

RHIC makes use of RF cavities to accelerate the particles in the beam bunches. The frequency of the cavities varies from 28 MHz at injection and increases during the acceleration phase. Once the particles have been accelerated to the top energy, the cavities are set at 198 MHz for beam storage [43]. The peak voltage of the RF cavities also has to vary during the acceleration stage starting at 300 kV at injection and ramping up to 6 MV during the beam

storage and collisions [44].

The beam pipes in the experimental region are made of beryllium to make them more transparent to passage of collision products and are 7 cm wide. The interaction regions area maintained at 10^{-10} torr [44].

Nuclear and coulomb scattering of beam with residual gas particles degrades the beam quality. Therefore, a high vacuum in necessary in the beam pipe. The beam passes trough parts operating at room temperature (16 % of the beam line) and low temperature. The vacuum requirements are differenct in cold and warm sections. The room temperature vacuum has to be on average 5 x 10^{-10} torr while the 4° K temperature vacuum has to be at $\leq 10^{-11}$ torr (for comparison the vacuum at 1000 Km altitude is 10^{-10} torr). The residual gases in the warm or room temperature regions are 90% H_2, 5% CO and 5% CH_4. The residual gases in the cold regions are H_2 and He [44].

The energy stored in the beam during a given run is 350 kJ per ring of ions. This is roughly the equivalent of leaving an iron on for about 6 minutes. This much energy has to be dumped once the luminosity has decreased to undesirable levels or the beam is not stable. Protons beam's energy per ring is 900 kJ. The beam is deflected at beam dump towards a graphite composite called carbon-carbon (C-C) which is stress or high thermal shock resistant. The C-C material is 0.5 m long and after it there is a slab 2.7 m long made of graphite and finally an extra slab 2 m long of steel [44].

2.2 Collisions

In summary, the first stage of ion beam production is the creation and acceleration of ions. Negatively charged ions are created at the pulsed sputter ions source. The ions are accelerated in a differential potential in the EBIS and the Linac and some of its electrons are stripped off by traversing a foil. The energy per nucleon is 1 MeV and for the case of Au ions the charge is +32 (32 electrons have been removed from the Au atom) by the time they are ready be injected at the Booster. The ions are then injected in the Booster that increases its energy to 95 MeV per nucleon. More electrons are stripped from the ion so that its charge becomes +77 (only two electrons remaining) at the end side of the Booster. The ions are transfered to the Alternating Gradient Synchrotron where they reach the energy of 10.8 GeV/u. The ions remaining electrons are fully stripped before they are finally injected to RHIC for final acceleration, storage and collisions [45] [31].

Chapter 3

STAR

The Solenoidal Tracker at RHIC (STAR) is a multipurpose detector particularly well suited to study high multiplicity heavy ion collision events. It consists of many sub detectors placed under a magnetic field created by cylindrically shaped aluminum magnet coils. STAR can measure the energy and momentum of charged particles via the Time Projection Chamber(TPC) and the transverse energy deposition of neutral particles vie the Barrel Electromagnetic Calorimeter(BEMC). The neutral particles detected mainly consist of direct photons and photons coming from π^0 decays. The electromagnetic calorimeter and the time projection chamber have full azimuth coverage. This makes STAR an great tool to study correlations of particles in relative azimuth.

3.1 BBC

The BBC (Beam Beam Counter) detector is used as a minimum bias collision trigger and to measure proton beam polarization when operating on p+p collisions mode. The BBC consist of two sets of scintillators located around the beam pipe at 3.75 meters from the STAR interaction point on the east and west sides from the Time Projection Chamber. Each set of

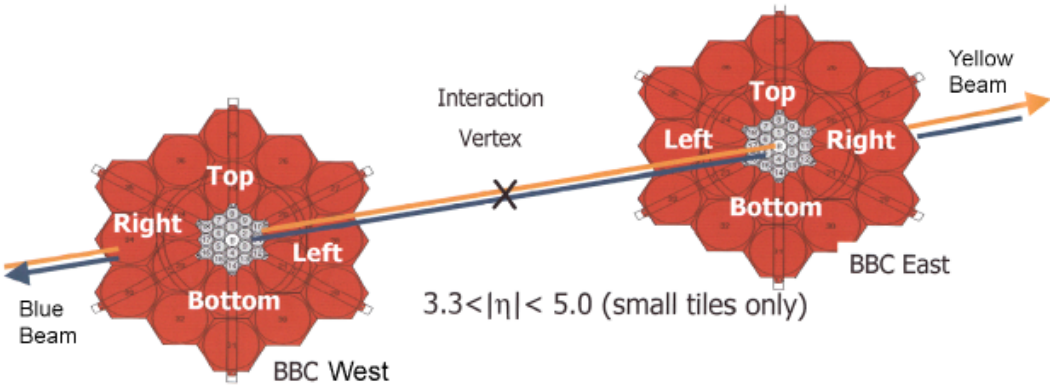

Figure 3.1: BBC east and west sets of scintillators positions with respect to the interaction vertex. The yellow and blue beams pass right through the middle. Whenever a collision occurs, high η particles hit the scintillators (taken form [46])

scintillators is made of 2 concentric annuli and each annuli is composed of two rings of hexagonal tiles with 6 tiles in the first ring and 12 tiles in the second ring for a total of 36 tiles (see Fig. 3.1). The light produced at each tile when it is hit by a particle coming from a collision is transmitted by 4 optic fiber strips connected to a single photomultiplier. The minimum bias trigger is fired whenever a hit is recorded in at least one of the scintillator tiles in both the east and west BBC (a coincidence hit) [46]. The firing of this trigger sends a signal to other detectors communicating the presence of a collision.

3.2 BEMC

The Barrel Electromagnetic Calorimeter is a cylindrical detector used to measure the transverse energy, η and ϕ of electrons and neutral particles(γ's,

π^0 decays) present in a collision. It is localized between the Time Of Flight detector and the magnet coils (see Fig. 3.2). Charged hadrons typically deposit a small amount of energy in the detector as minimum ionizing particles; while electrons and γs typically deposit all of their energy in the detector by creating electromagnetic showers. The expected energy resolution of the calorimeter is around $14\%/\sqrt{E}+1.5\%$ [47].

The BEMC has an acceptance of $|\eta|$ <1.0 and full azimuth. It is segmented into 4800 towers of 20 radiation lengths at mid rapidity. The towers are distributed in 120 modules of $\Delta\eta = 1.0$ and $\Delta\phi \sim 0.1$ rad (26 cm wide, 293 cm long and 23.5 cm depth). Each tower subtends an area of $\Delta\eta$ x $\Delta\phi$ = 0.05 x 0.05 and have a geometry such that they project back to the interaction region. The towers are made of alternating lead and scintillator layers made of Kuraray SCSN81. There are 19, 5 mm, thick lead layers and 20, 5 mm, thick scintillator layers plus two scintillator layers of 6 mm. The bigger scintillator layers are positioned in front of a pre-shower detector. When energetic electrons pass through the lead layers of a BEMC tower they produce photons via bremsstrahlung and the photons create $e^+ + e^-$ pairs. The electrons further excite the atoms in the scintillator layers that emit light at relaxation. The light from each scintillator is collected and transported by a wavelength shifting fiber (WLS). The WLS connects to multi-fiber optical connector which transmits the light to the photomultipliers (PMT's). Each tower of the BEMC is connected to a single PMT [47].

The BEMC is used to trigger on events that contain a single tower (or

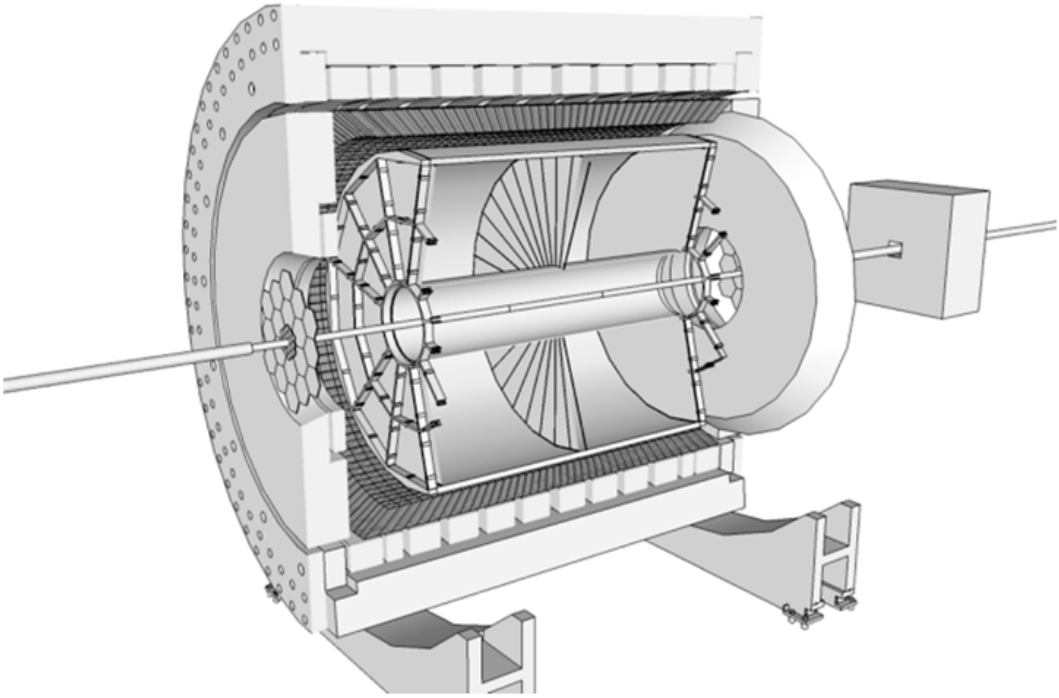

Figure 3.2: The Barrel Electromagnetic Calorimeter surrounding the Time Projection Chamber and being surrounded by the magnet coils. Credit goes to Tai Sakuma

cluster of towers forming a patch) in which a high deposition of energy has occurred. The tower whose recorded energy triggered the event is called the high tower. High tower triggered events were selected for the analysis presented in this dissertation, this is done in order to bias the events to contain a high population of highly energetic jets.

3.3 TPC

The Time Projection Chamber (TPC) is 3 dimensional camera that takes pictures of all of the particles' trajectories coming out of a given collision. It was the world's largest time projection chamber before the construction of the Large Hadron Collider at CERN. A time projection chamber reconstructs charged particles' trajectories by recording the gas ionization energy depositions that they leave on their fly path.

The TPC at STAR has full azimuth and $|\eta| < 1.8$ acceptance. It has a cylindrical shape and is made of an inner cylinder enclosed within a bigger cylinder and closed at the ends. The TPC has a length of 4.2 m and a total radius of 2 m. The inner cylinder radius is 50 cm leaving space for the beam pipe to traverse it at the middle (see figures 3.2 and 3.3). The smaller cylinder is called the inner field cage and the bigger one is called the outer field cage. The cylinder cavity is divided in two halves by a central membrane that is kept at 28 kV. Both ends of the TPC are segmented into 12 sectors. Each sector is 30° wide and is divided into the inner sector going from the inner field cage up to a radius of $\sim$ 1.3 m and a outer sector that extends to the outer field cage. Trajectories of charged tracks whose p_T ranges from 100 MeV/c up to $\sim$ 30 GeV/c can be reconstructed at the TPC [48].

The time projection chamber is immersed in a 0.5 Tesla B field produced by the surrounding solenoid magnet and parallel to the TPC axis and beam direction. The gas used for track induced ionization consists of P10 gas(90% Ar 10% CH_4) which is maintained at 2 mbar above atmospheric pressure.

STAR operates the TPC at the peak of the P10 gas drift velocity vs. E field/pressure curve so that the drifting electrons' velocity does not vary too much with small changes in pressure and temperature. A typical electron drift velocity measured during Au + Au or p + p collision is ~ 5.5 cm/μsec [48].

The electrons ionized by charged particles coming out of a collision are pulled by the induce E field to drift towards the ends of the TPC where they are collected. The E field inside the TPC is produced by setting the potentials of the central membrane, ground wires placed at the end cap sectors and concentric cylinders at the outer field cage that go from the central membrane to the end cap sectors. The magnitude of the E field produced this way is 135 V/cm in the direction towards the central membrane (electrons drift towards the sectors and positive ions drift towards the central membrane) [48].

The end caps where electron collection takes place have four layers, the pad plane, anode wires, ground wires and gating grid wires. The anode wires are perpendicular to the radial direction for better momentum determination of high p_T tracks and are 4 mm apart. The ground grid wires are 75 μm in diameter and they help to define the TPC potential. The gating grid is another set of wires 6 mm apart from the ground grid. These wires are set to change their potential to allow or disallow passage of electrons from the TPC volume to the anode wires. Their regular voltage of 110 V is increased and decreased on alternating wires by $\pm$ 75 V. This change in voltage "closes" the TPC by attracting the electrons and preventing them to ever getting to the anode wires. The TPC gating grid is at nominal voltage during data taking and at

shifted voltage the rest of the time and can change its voltage at a rate of 0.5 V/ns. Note that positive ions created close to the anode wires are too slow to drift into the TPC volume while the gating grid is "open". The anode wires are at high enough E field that further ionization takes place. This creates an avalanche of electrons enhancing the image charge signal seen at the pads created by the slower moving ions formed around the anode wires. The anode wires are just 20 μm in diameter; this gives a 1000 to 3000 amplification [48].

The hits measured at the anodes in the sectors are used to track reconstruction. A charged hadron traversing the TPC volume follows a helix path due to the Lorentz force produced by the magnetic field present. The track ionizes atoms in the P10 gas leaving clusters of ions-electrons along its path. The electrons drift towards the end cap sectors. They get trapped by anode wires producing an image charge that is read out in a pad close the anode wires. Up to 45 different clusters of charge ("hits") can be obtained from a single track. The x and y positions of each hit can be obtained from pads's positions. The time of arrival of the charged clusters is recorded. An electron that drifts along the largest possible path length in the TPC will suffer a transverse and longitudinal deflection of: $\sigma_T = 3.3mm$ and $\sigma_L = 5.2mm$. The electron drift velocity is used to calculate the hits' z position. Sub millimeter track hit reconstruction precision is achieved. A track finding algorithm has to be used to look for close by hits and fit them to a helix. Once you have a given tracks' trajectory you can determine its momentum by measuring its curvature under the B field [48].

A track's p_T is proportional to the magnetic field and the radius of curvature of a track: $p_T(GeV/c) = 0.3B\rho(Tm)$. The radius of curvature is computed by measuring the sagitta of the track's trajectory between two points at a distance L. It turns out that $s \sim (0.3L^2B)/(8p_T)$ at a high enough $p_T \sim 1$ GeV/c. Another function of The TPC is to provide a measurement of the collision vertex position by using and extrapolation of all the reconstructed tracks in an event (after quality cuts). Vertex resolution is sub-millimeter going down to about 300 microns for high multiplicity events where there are about 1000 tracks in a single event (for example a central Au+Au collision) [48].

Another feature of the TPC is its ionization energy deposition PID capability. Hadrons traversing the gas-filled TPC volume loose $\sim$ 25 eV of energy for each atom ionized (or 2.5 eV per cm of gas traversed). The energy lost by ionization is well described by the Bichsel formula. This energy loss (dE/dx) depends on β so plotting it against momentum gives rise to different bands for different particles. This happens since different particles (masses) have different momentum at the same β. TPC has PID capabilities up to about 1.2 GeV/c for proton-pion using dE/dx. The dE/dx is measured by recording the amount of charge seen in the pad rows after taking into consideration the gain due to the amplification at the anode wires. The truncated mean of the hits in 45 distinct points of the track's trajectory is used as the dE/dx measure. The truncated mean is the mean after the highest 30% dE/dx cluster signals have been removed [48].

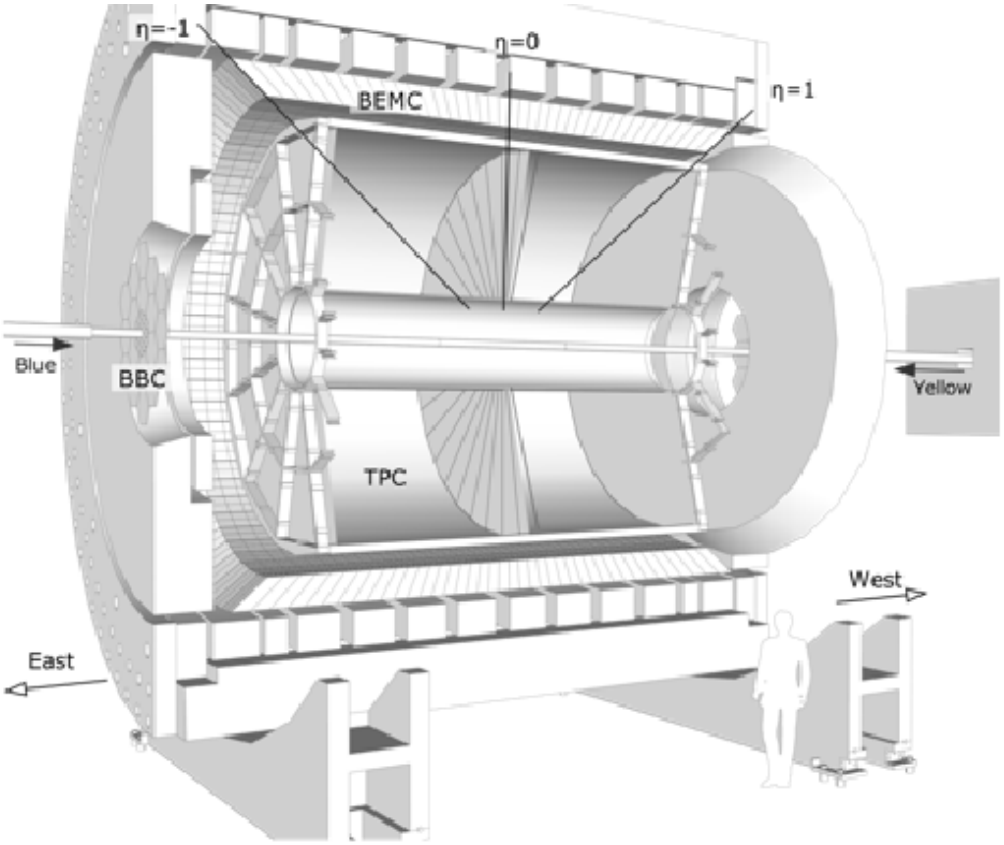

Figure 3.3: A different cut view of the STAR detector. The TPC chamber with its inner cylinder and central membrane is observed in the center of the figure. Credit goes to Tai Sakuma

3.4 TOF

The Time of Flight (TOF) measures the time that it takes for charged hadrons to travel from the collision vertex point to the place in the detector that they hit. The TPC provides us with information about charged particles' path length and momentum. Using the TOF we can get the velocity β which combined with the momentum can be used to identify the particle ($p = \beta\gamma mc$) even in a momentum range where dE/dx cannot be used for that purpose.

TOF consist of two sub-systems: the Vertex Position Detector (VPD) that measures the time at which a collision happened and the TOF detector that measures the time at which a particle hits the detector. The VPD's are placed around the beam pipe and are located 5.6 m away from the center of STAR. Currently, the upgraded VPD has 19 photomultiplier detectors in the east and west sides at a $4.24 < |\eta| < 5.10$. The photomultipliers are placed before a lead cap and scintillator material. Photons coming out of the collision interact via pair production in the lead which generates electrons and positrons that produce light while interacting with the scintillator. This produces an increased signal in the PMT [49].

The TOF detector is segmented into 120 trays surrounding the TPC. Each tray is 2.4 m long 21.3 cm wide and 8.5 cm deep. Each tray is placed at a radius of 2.14 m from the beam line with a coverage of $|\eta| \sim 0.9$ and 2π in azimuth. A single tray has 32 modules. Each module has six channels (pads) and is made of Multigap Resistive Plate Chambers (MRPCs). The MRPC module is 9.4 x 21 cm. It consist of a stack of five 0.54 mm thick glass

layers surrounded by two outer glass layers of 1.1 mm thickness, a graphite electrode, six copper pads a PC board and honey comb material. The inner glass layers are separated by 220 microns [50]. High voltage is applied to the electrodes that generate an electric field at each gap between plates. The trays are completely filled with 90% tetra-fluoro-ethane ($C_2H_2F_4$), 5% iso-Butane and 5% of SF_6 gas [51]. When a charged particle passes through a given MRPC it ionizes the gas and the strong electric field generates avalanches at each glass-glass gap. The signal induced in the pads is the sum of the signals from each avalanche [50].

The time of flight of each charged particle is assigned by extrapolating the tracks reconstructed in the TPC and matching them with a TOF hit. The time of flight resolution is 100 ps and even less for high multiplicity ion + ion collision events [50]. The variable $\Delta\beta^{-1}/\beta^{-1}$ will be used for PID purposes in the analysis presented in this thesis. The higher contribution to this variable resolution comes from the time of flight resolution for tracks above p $\sim$ 1 GeV/c.

The TOF system allows pion, kaon and proton discrimination up to p $\sim$ 1.8 GeV/c and pion plus kaon and proton discrimination up to $\sim$ 3.0 GeV/c. [49]. In comparison, using TPC's dE/dx pions and kaons can be distinguished up to momentum of $\sim$ 0.6 GeV/c; protons can be separated up to $\sim$ 1.0 GeV/c. As can be seen, the time of flight information increases the momentum at which we can achieve particle identification to a region where baryon to meson ratio enhancement is observed in central Au+Au collisions.

The PID capabilities at STAR are further enhanced by combining the TPC and TOF information as will be discussed in section 4.4.

Chapter 4

Analysis

4.1 Event Selection

The data used in the present work were recorded at STAR during the year 2010. On that year $\sim$ 400 million Au+Au collisions at $\sqrt{s_{NN}} = 200$ GeV were produced. The collisions used in the present analysis were required to have a high tower trigger which lowered the collisions amount to 57 million ($1.4\ fb^{-1}$). High tower triggered events must contain a single calorimeter tower with an energy deposition of at least 4.3 GeV. The STAR collaboration assigns different id numbers to each trigger configuration present during the same collision period. The trigger id's used for this analysis are: 260,504, 260,514 and 260,524. The high tower trigger biases our events towards events with at least one hard scattering collision present in them. For any kind of collision to the recorded, hits on both the west and east sides of the vertex particle detector are required. Simultaneous hits on both sides of the detector signal that a heavy ion collision has taken place inside of the detector (3.1). The way to make collisions occur inside the detector is by steering the beams that are coming in opposite directions of the main interaction region. Collisions closer to the center of the detector are preferred due to their uniform acceptance. In reality the collision data recorded has a collision vertex distribution centered

at the middle of the TPC. An extra cut on the collision's vertex position along the beam line (z direction) of ± 30 cm off-line was applied in order to avoid events too far away from the detector's center.

An extra cut of 5 GeV on the energy deposited on the high towers is imposed to avoid effects coming from the on-line trigger onset bias. The tracks can deposit energy in the calorimeter towers too. Most of them deposit their energy as MIPs (minimum ionizing particles) but electrons can lose close to 100% of their energy in a single tower. Tracks and tower hits are matched event by event and the total energy of a matched hadron is subtracted from the corresponding calorimeter energy recorded in order to avoid double counting at the jet reconstruction step. No attempt was made to correct for particles coming from decays of Λ and K_0^s. The collision's z vertex position can be simultaneously measured by the vertex particle detector and the time projection chamber. A cut of $|zV_{VPD} - zV_{TPC}| < 3.0$ cm was imposed as a quality assurance measure.

The tracks reconstructed at the TPC have to comply with certain quality cuts. A track's path is reconstructed by fitting a helix through all the hits recorded in the TPC that give the x,y,z position of the trajectory (see section 3.3). A maximum of 45 hits can be measured for a single track. Some hits can be so close together that they merge, this reduces the total number of hits that end up being used for the track reconstruction. Space charge build up inside the TPC can also create an extra Lorentz force that makes a hit reconstructed position to be displaced such that the track fitting algorithm does not recog-

nize it as part of its track. A way to avoid using these tracks is to require for a track to have at least 15 hits and to have used at least 52% of its hits to fit the tracks' helix. Finally, only tracks with a distance of closest approach (DCA) to the collision vertex of at most 1.5 cm are considered to avoid contamination from hadrons interacting with the beam pipe and to reduce the contamination from decaying daughters at high transverse momentum.

The analyzed collisions are further constrained to contain a high p_T jet on them. Please refer to section 4.3 for further details on jet selection. The events used in the analysis are divided in two centrality classes. The 0-20% and 20-80% most central events. This is done in order to look for particle production differences in events where the p/π enhancement is more pronounced (central events) and compare it to events where the enhancement is milder to non-existent (more peripheral events). The centrality separation is done by measuring the charge hadron multiplicity at mid-rapidity of the collisions (refmult) and comparing it with a Monte Carlo simulation using the Glauber model (more details on section 1.4). The required multiplicity cuts are $266 \leq refmult$ for the 20% most central events and $10 \leq refmult < 266$ for the 20-80% most central events. The final number of events that passed all the cuts and that contain a high p_T jet on them are shown on table 4.1.

Table 4.1: Events used in the analysis

Centrality	**Events after cuts**	**Jet-Triggered events**
0-20 %	9.4M	167k
20-80 %	3.2M	68k

4.2 Pile Up

While increasing an accelerator's luminosity is desired to accumulate enough statistics for rare processes, it also brings about some challenges. An undesired effect of higher luminosity is the decrease of the time between collisions so that it is smaller than the time required for recording a collision event. A TPC based detector working at close to 100% dead time will record track trajectories coming from different events in a single one under this high luminosity conditions. This effect is referred to as pile up. Every track that passes minimal quality cuts is labeled a global track. A vertex finding algorithm uses all global tracks to reconstruct their common vertex (the collision vertex). Once the most probable position of the vertex of an event is found, every track whose extrapolation passes through the vertex is labeled as a primary track and it is considered to be part of the event. In a pile up free event, most of the tracks will be labeled as primary. On a pile up rich event, most of the tracks will remain labeled as global.

The approach used to exclude events suspected to have pile up contamination was to plot the number of global tracks versus the number of primary tracks in a 2D histogram for all the events that passed the quality cuts criteria. The distribution shows a clear, almost linear, dependence of the number of global and primary tracks and many outliers events where the number of global tracks exceeds the number of primary tracks by an atypical amount. This can be seen on Fig. 4.1. The 2D histogram is projected into the number of global tracks axis using slices of size equal to 15 number of primary tracks.

The resultant distributions are fitted with a Gaussian on the left side of the distribution and then all the events whose number of global tracks was 3σ away from the Gaussian mean (as shown in Fig. 4.2) are cut out. This process was repeated for every single slice. The 2D histogram of number of global vs. number of primary tracks obtained after the cut is applied is shown on Fig. 4.3.

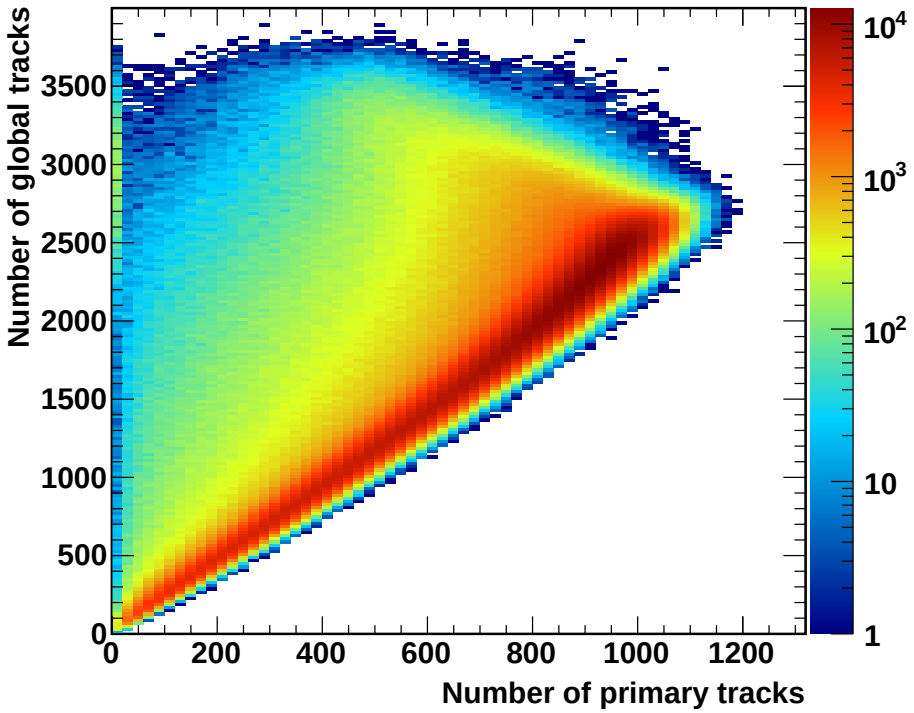

Figure 4.1: Events distribution of number of global vs. number of primary tracks before pile up cut

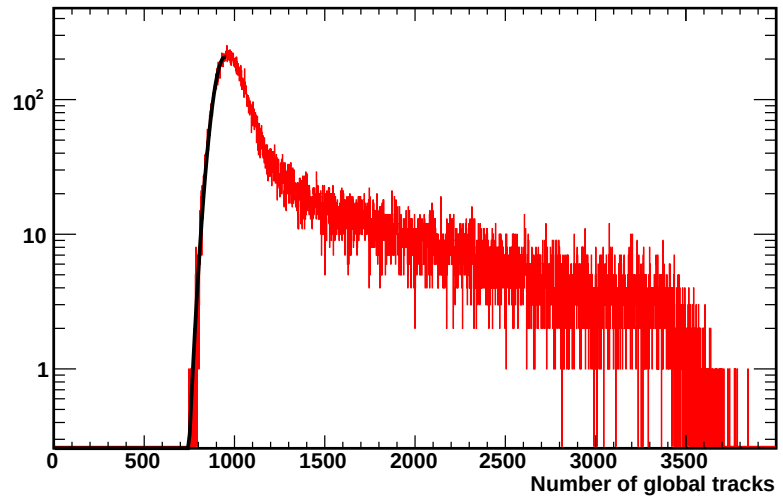

Figure 4.2: Projection of the global vs. primary distribution (Fig. 4.1) on the y axis (number of global tracks) for a particular bin (interval) of primary tracks

4.3 Trigger Jets

The jets used in this analysis were reconstructed using the $anti - k_t$ jet finding algorithm with a parameter R = 0.4. Only towers (tracks) with a transverse energy (momentum) above 3.0 GeV(/c) in every event were used for jet reconstruction. This reduces the amount of energy deposited in the jet neighborhood coming from the heavy ion collision background. Of course, the reconstructed jet energy is not equal to the energy of the hard scattered parton that originated it. We can, nevertheless, recover the approximate azimuth direction of the scattered parton and analyze particle production around the jet axis. The jets were selected to have the high tower (with transverse energy $>$ 5 GeV) that triggered the event as one of its constituent particles. It is

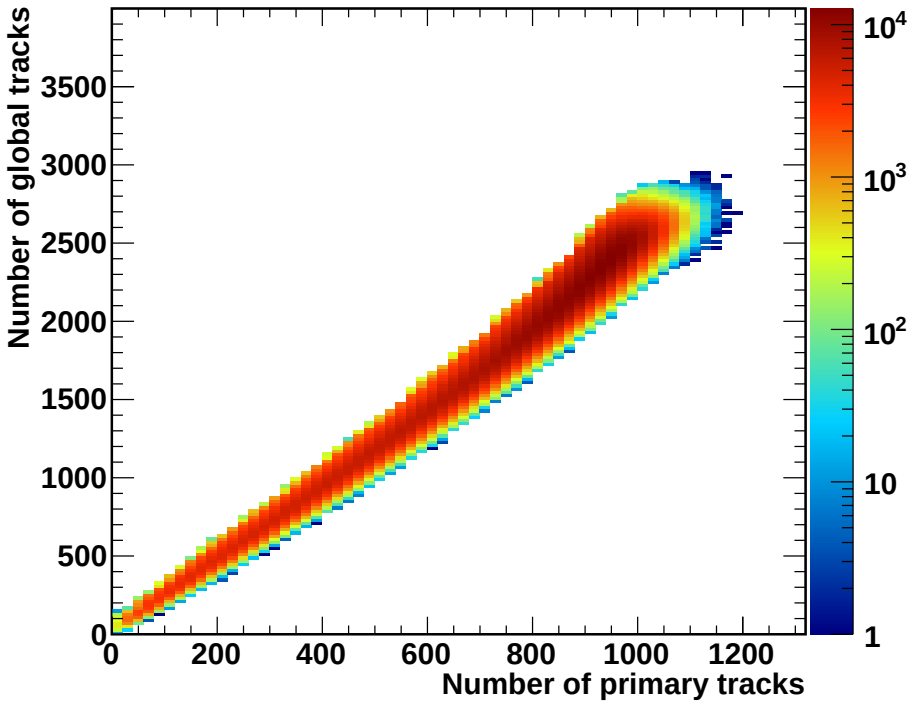

Figure 4.3: Events distribution of number of global vs. number of primary tracks after pile up cut

further required for the jets to have a reconstructed transverse momentum of $8 \leq p_T^{jet,reco} < 20$ GeV/c. The high p_T of the reconstructed tracks and the final jet presumably biases the jet sample towards jets that do not traverse the medium present in Au+Au collisions [16, 52].

The highly biased reconstructed jets are correspond to a single hard scattering in central and mid-peripheral Au + Au events. The recoil from the trigger jets can be used as a probe of the medium provided that the trigger jets have similar fragmentation. This will be the case if they are biased toward the collision surface and fragment in vacuum. Jets produced at the surface of a peripheral or a central Au+Au collision should not be different. The normalized $p_T^{jet,reco}$ distribution of central and peripheral events were compared. The central distribution is higher by ∼10% for $8 < p_T^{jet,reco} < 14$ lower by ∼ 20% for $15 < p_T^{jet,reco} < 20$. The trigger jets transverse momentum distribution can be seen in Fig. 4.4

4.4 Particle Identification

The TPC and TOF detectors can be used for proton, kaon and pion identification. The TPC measures the momentum of charged particles coming out of a collision. It also measures the amount of energy deposited in the chamber's gas via ionization by the charged particles as they traverse it. Each hit used for track reconstruction provides a measurement of the amount of energy lost per unit length (dE/dx). The hit's dE/dx distribution for each track (that can have up to 45 hits) is truncated (getting rid of the highest

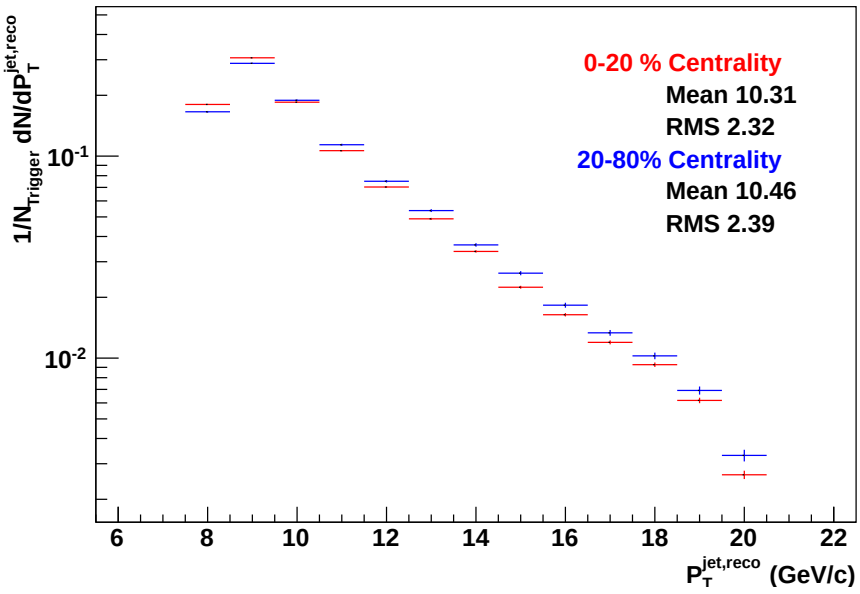

Figure 4.4: Pet trigger jet $dN/d(p_T^{jet,reco})$ distribution. Jets from 0-20% (20-80%) most central events are shown in red (blue).

values) and the mean of the remaining distribution is obtained. This gives the truncated mean for a giving track (<dE/dx>). The energy loss of a charged particle in a gas can be calculated using the Bichsel equation (A Bethe-Bloch equation for gases). The energy loss of a charged particle depends on its $\beta\gamma$ value. Therefore, a 2D plot of dE/dx versus momentum for different particle species gives rise to different bands. These bands can be used for PID purposes on a given momentum slice (interval). One way to estimate the chance of a particle to belong to a given species is to quantify how far away from the species' Bichsel band the measured <dE/dx> is. The separation of the logarithmic dE/dx measurement from the calculated/expected value given

as number of sigmas is used as PID metric at STAR. Eq. 4.1 defines this measurement where i corresponds to kaon, proton, pion , electron etc. The label "meas" ("exp") refers to the measured (expected) value. The difference in log(dE/dx) is divided by its resolution to obtain the number of sigmas away. The resolution is obtained from the measured distribution on a narrow momentum slice. The log measurement is preferred since its distribution on a given momentum slice is a Gaussian. This is not the case for the dE/dx variable.

$$n\sigma^{i}_{dE/dx} \equiv \frac{log(< dE/dx >^{i}_{meas}) - log(< dE/dx >^{i}_{exp})}{\sigma_{log(dE/dx)^{i}_{meas}}} \tag{4.1}$$

Fig. 4.5 shows the dE/dx distribution versus p_T for charged particles coming out of several 200 GeV Au+Au collisions at STAR. The color palette shows the counts in logarithmic scale. Clear bands of pions, protons and kaons can be observed for $p_T \leq 1$ GeV/c. The Bichsel energy loss expectation bands are also plotted.

STAR PID capabilities were extended with the addition of the TOF detector on 2009. The mass (and therefore identity) of a particle can be calculated if the momentum and velocity of the particle is known: $p = \gamma\beta m$. The momentum of the particle is measured by the TPC. The velocity of a charged particle is obtained by combining the time of flight measurement with the path length from the TPC. A 2D histogram of hits on inverse velocity (β^{-1}) versus momentum provides us with mass dependent bands allowing us

to extend PID to $\sim$ 1.6 GeV/c. Note that the dependence is on p and not p_T. Fig. 4.6 shows a histogram of momentum vs β^{-1} for charged hadrons coming out of several 200 GeV Au+Au collisions. The π,p,K and electron bands are clearly visible at low momentum and start to merge at high values of momentum.

The PID capabilities can be improved in the region of interest for this analysis. Namely the region where a p/π enhancement is observed, $p_T > 1.6$ GeV/c. To do so, it is necessary to use the TOF's β^{-1}_{TOF}, TPC's $n\sigma^{i}_{dE/dx}$ and calculated $\beta^{-1}_{TPC,i}$ (defined in Eq. 4.2) using a given mass assumption to define the quantity $\Delta\beta^{-1}_{i}/\beta^{-1}$ (see Eq. 4.3). This quantity is preferred to m^2 due to the fact that the resolution is suppressed at high momentum. On the other hand, the mean is momentum dependent and has to be found for each momentum bin interval used in the analysis.

$$\beta_{TPC,i} = \frac{1}{\sqrt{1 + (m_i^2/p^2)}} \tag{4.2}$$

$$\Delta\beta^{-1}_{i}/\beta^{-1} = \frac{\beta^{-1}_{TOF} - \beta^{-1}_{TPC,i}}{\beta^{-1}_{TOF}} \tag{4.3}$$

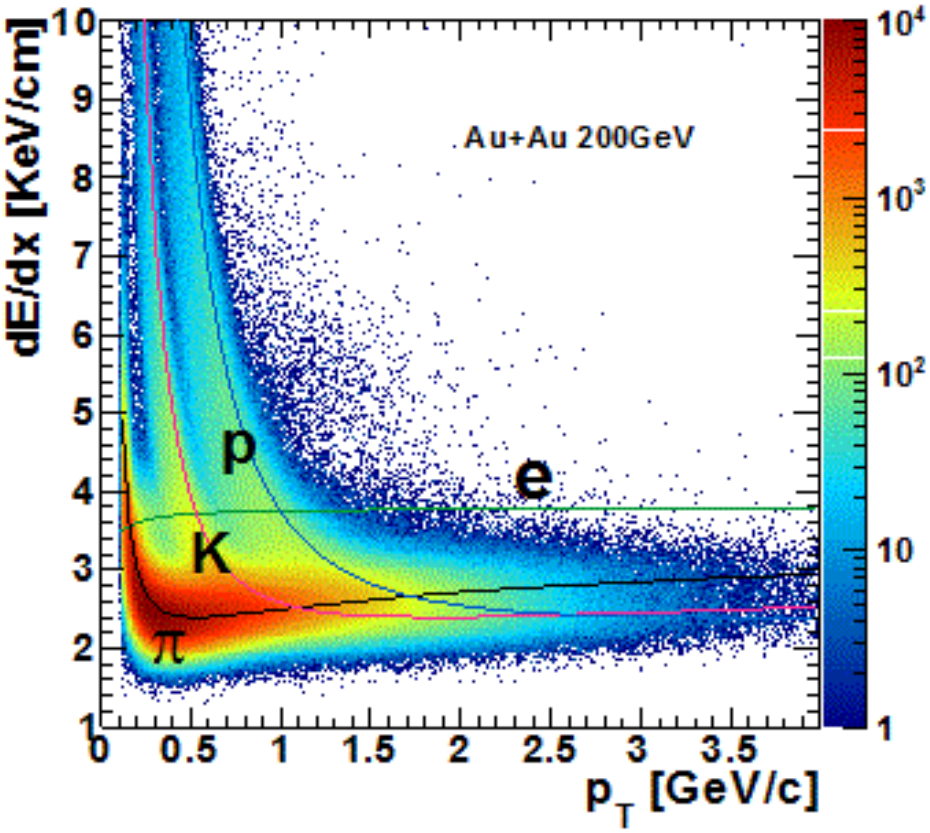

Figure 4.5: dE/dx versus p_T distribution in 200 GeV Au+Au collisions. The black line is the Bichsel expectation value for pions. The green line is the Bichsel function for electrons, the pink one corresponds to kaons and the blue one to protons.

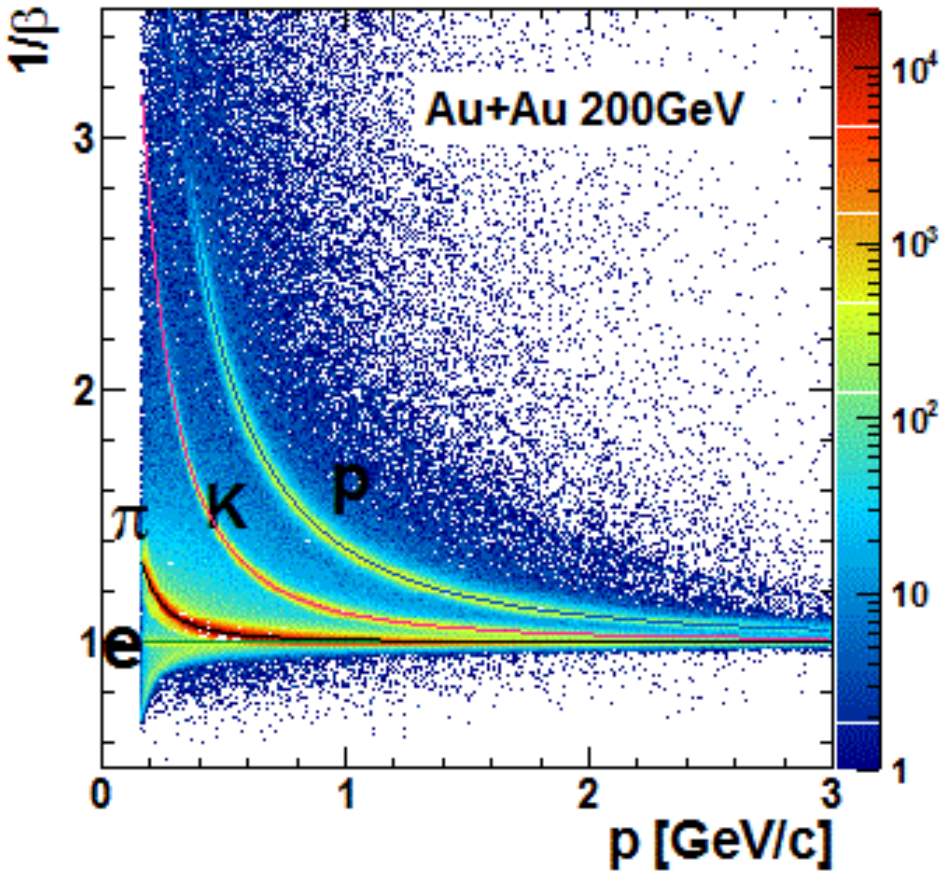

Figure 4.6: β^{-1} versus momentum in 200 GeV Au+Au collisions. The expected value for pions, kaons and protons are plotted for comparison.

A range of p_T values in a histogram bin can have different p values due to the relationship $|p| = p_T cosh(\eta)$ and since particles are recorded in pseudo-rapidity intervals of $\pm$ 1 for this analysis. The final results will be reported as a function of p_T but the variables used for PID are functions of momentum ($\beta\gamma$). Therefore, track distributions coming from similar momentum and pseudorapidity intervals which will correspond to particles with similar p_T have to be considered . The tracks are divided into five different η intervals of width 0.2. The intervals are: $|\eta| = [0.0, 0.2), [0.2, 0.4), [0.4, 0.6), [0.6, 0.8)$ and $[0.8, 1.0)$. The momentum intervals are split with 5 $|p|$ intervals of width of 0.1 in the range of 0.1 - 0.6 GeV/c and 14 intervals of width 0.2 in the range 0.6 - 3.4 GeV/c.

The first step on the particle identification method is to use Au+Au collisions data with the centrality cuts used in the analysis to get distributions of $n\sigma^i_{dE/dx}$ vs $\Delta\beta_i^{-1}/\beta^{-1}$ on each pair momentum and pseudorapidity intervals separately. The $n\sigma^\pi_{dE/dx}$ distribution of pions is a Gaussian centered at zero if our sample consists of pions entirely. Two other Gaussian peaks with their means shifted from zero (at low momentum at least) are seen if kaons and protons are added to the sample. The means of the Gaussians for all particles move closer to zero if the momentum of the particles being considered increases from $\sim$ 1 to $\sim$ 1.5 GeV/c and start to deviate from zero again at higher values (due to the relativistic rise of the Bichsel function). The distribution of $\Delta\beta_\pi^{-1}/\beta^{-1}$ turned out to be better described by a Student's t distribution. If a sample consists of protons, pions and kaons three peaks will be seen with the

one centered at 0 corresponding to the pions and the ones shifted from zero corresponding to other particle species. Plotting both variables in 2D allows to differentiate the peaks (consisting of a Gaussian x Student's t distribution) at a higher momentum.

The 2D distributions can be composed of one, two or three peaks depending on momentum. At higher momentum both $n\sigma^{i}_{dE/dx}$ and $\Delta\beta_{i}^{-1}/\beta^{-1}$ start to merge and the three peaks get closer to zero. At low momentum the different particles peaks are clearly distinguishable and the choice was made to use a proton mass assumption for proton identification (and similarly with kaon and pion) such that the distribution will be centered $\sim$ (0,0). Once the peaks start to merge, it is necessary to model the distributions with a suitable function that can be used to assign a probability of a particle to be of a certain species. Whenever the different particle peaks started to merge, a pion mass assumption is used to plot the 2D distributions (this choice is arbitrary and the method would work identically if one prefers to use a kaon or proton mass assumption instead). At momentum above 1.0 GeV/c (for all η intervals) the pion and kaon peaks were so close together that a 2D model consisting of two Gaussian x Student's t functions was necessary, one corresponding to the pions and one to the kaons. At momentum above 1.8 GeV/c (for all η intervals) a third function had to be included for the protons. These momentum intervals were used both in the central and mid-peripheral data. The Student's t distribution normalized to 1 is shown on Eq. 4.4 where ν is the degrees of freedom, μ is the location parameter and λ is the inverse scaling parameter.

$$\text{Student}(x) = \frac{\Gamma\left(\frac{\nu+1}{2}\right)\sqrt{\left(\frac{\lambda}{\nu\pi}\right)}}{\Gamma\left(\frac{\nu}{2}\right)}\left(1+\frac{\lambda(x-\mu)^2}{\nu}\right)^{-\left(\frac{\nu+1}{2}\right)} \tag{4.4}$$

As an example of how the 2D distributions look like in 0-20% most central Au+Au collisions, Fig. 4.7 shows the distribution from the momentum interval 2.0 - 2.2 GeV/c and $|\eta| < 0.2$. This plot corresponds to a pion mass assumption as can be seen by the fact that the pions (the most prominent particle in Au+Au collisions) are closer to the plot's origin.

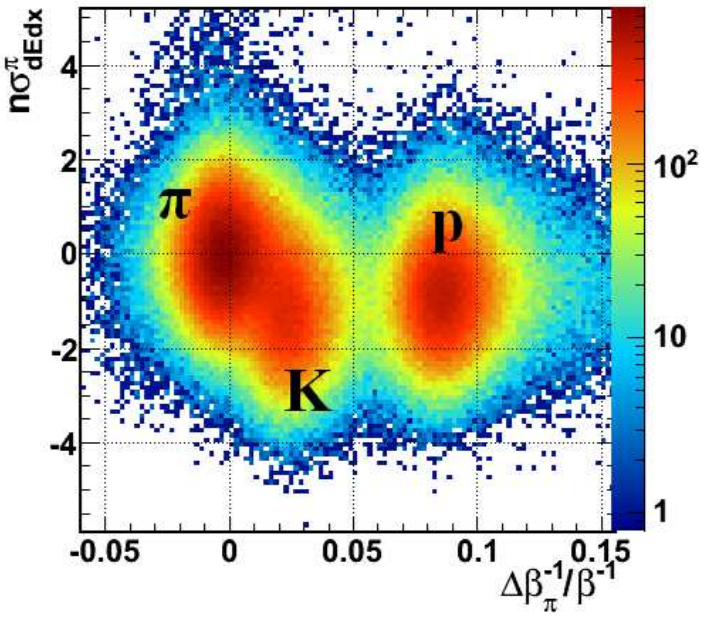

Figure 4.7: 2D histogram of $\Delta\beta_{\pi}^{-1}/\beta^{-1}$ vs $n\sigma^{\pi}_{dE/dx}$ (pion mass assumption) from 0-20% most central 200 GeV Au+Au collisions on the $|\eta| < 0.2$ and 2.0 $\leq$ momentum $<$ 2.2 GeV/c intervals. The pion, kaon and proton peaks are labeled on the plot. Pions and kaons are partially merged.

The next step after obtaining the histograms with these distributions for all of the η and p intervals is to fit them with the Gaussian x Student's t model. Eq. 4.5 shows how this model is constructed for the case when there are three particles present in the distribution. The model is the sum of three products of two probability density functions (pdf's) one being a Gaussian and the other a Student's t distribution. Each of these pdf's are normalized to one, as well as their product. The subscript of each 2D pdf labels the particle to which they belong. Each 2D pdf is multiplied by the fraction of total entries (N) that correspond to the contribution of that particle to the total, that is, $f_K + f_\pi + f_p = 1$.

$$\begin{aligned} F(p, \eta, \Delta\beta_\pi^{-1}/\beta^{-1}, n\sigma^\pi_{dE/dx}) = N(&f_\pi \mathrm{Gauss}_\pi(n\sigma^\pi_{dE/dx})\mathrm{Student}_\pi(\Delta\beta_\pi^{-1}/\beta^{-1}) \\ &+ f_K \mathrm{Gauss}_K(n\sigma^\pi_{dE/dx})\mathrm{Student}_K(\Delta\beta_\pi^{-1}/\beta^{-1}) \\ &+ f_p \mathrm{Gauss}_p(n\sigma^\pi_{dE/dx})\mathrm{Student}_p(\Delta\beta_\pi^{-1}/\beta^{-1})) \end{aligned} \tag{4.5}$$

The 2D distributions have to be fit for each η and p intervals. Furthermore, positive and negative tracks with the two magnetic field configurations used in Run 10 were modeled separately. Table 4.2 shows the number of events as well as the TOF and TPC data cuts used to get the 2D distributions.

The model function of Eq. 4.5 is used to fit the measured distributions obtained from data (histograms like the one shown in Fig. 4.7). This fits make it possible to get the parameters that define each particle's pdf and their contribution to the model function. The RooFit toolkit was used to fit

Table 4.2: QA cuts and events used to create 2D distributions for PID

Au + Au at $\sqrt{s_{NN}}$ = 200 GeV		
	0-20%	**20-80%**
Evts FF	3.7M	1.4M
Evts RFF	5.6M	1.8M
$\|zVertex\|$(cm)	<30	<30
Fit/Max	0.52	0.52
DCA(cm)	1.5	1.5
Min Fit	15	15
$\|zV_{TPC} - zV_{VPD}\|$(cm)	6	6
$\|\eta\|$	1.0	1.0
β	>0.05	>0.05
TOF	>1.0	>1.0

the 2D distributions [53]. Every momentum and pseudorapidity bin has a set of pdf's parameters that can be used to define a probability function as in Eq. 4.6. Using this equation it is possible to use the fitted model function to assign each track with a probability of being a pion (or kaon or proton). This probability can be used to get a sample of a given purity for each particle species. The probability cut to select pions for further analysis was set to $\geq$ 0.75 (according to Eq. 4.6). The same probability cut is used for protons. It is worth noting at this point that the choice of 0.75 is almost completely arbitrary. Different values of the cut give different purity of pions (or protons) at a given momentum. The cut efficiency also depends on the number chosen.

$$P(p,\eta,\pi,\Delta\beta_{\pi}^{-1}/\beta^{-1},n\sigma_{dE/dx}^{\pi}) = \frac{f_{\pi}\mathrm{Gauss}_{\pi}(n\sigma_{dE/dx}^{\pi})\mathrm{Student}_{\pi}(\Delta\beta_{\pi}^{-1}/\beta^{-1})}{\sum_{i=\pi,K,p} f_i\mathrm{Gauss}_i(n\sigma_{dE/dx}^{\pi})\mathrm{Student}_i(\Delta\beta_{\pi}^{-1}/\beta^{-1})} \tag{4.6}$$

The efficiency of the probability cut is calculated by using the fit models to create a toy Monte Carlo of the particles' distributions and then counting the number of particles that survive the cut as will be explained in more detail in the following pages.

A pion is considered for further analysis if it passes the cut $P(p,\eta,\pi,\Delta\beta_{\pi}^{-1}/\beta^{-1},n\sigma_{dE/dx}^{\pi}) \geq 0.75$, similarly for protons. It is therefore necessary to estimate the number of particles that are missed due to that cut. Another cut applied both during the model parameters fitting and the actual analysis consist on ignoring any particles whose hits in the $n\sigma_{dE/dx}^{i}$ vs $\Delta\beta_{i}^{-1}/\beta^{-1}$ histogram lie outside of the set of ellipses that correspond to kaons, pions or protons. The axis of the ellipses are 3σ in the Gaussian and 3 standard deviations in the Student's-t distribution (standard deviation $= \sqrt{\frac{\nu}{(\nu-2)\lambda}}$ for $\nu > 2$).

The PID cut efficiency is computed in following steps.

1.- Loop over each pair of η and momentum bins.

2.- Use the corresponding momentum and η bin model parameters to generate pion, kaon and protons $n\sigma_{dE/dx}^{i}$ vs $\Delta\beta_{i}^{-1}/\beta^{-1}$ distributions and save them on a 2D histogram. The particles' distributions are generated by the Monte Carlo sampling of the model functions procedure in RooFit [54].

3.- Cut out any particles outside the ellipses described in previous paragraphs. This step gives the number of generated particles from each species: N^i_{gen}.

4.- Cut out any particles that have a probability of being a pion (or proton) less than 0.75.

5.- Count the number of particles that survive the cut to obtain the number of accepted particles: N^i_{acc}.

6.- Finally, obtain the PID cut efficiency for each particles species and each momentum and η bin as: $eff^i = N^i_{acc}/N^i_{gen}$.

Using a cut probability of 0.75 a purity of pions (protons) of $\geq 90\%$ (95%) was obtained on both the 0-20% and 20-80% centralities of Au+Au 200 GeV collisions for momentum ≤ 3.4 GeV/c and all $|\eta| < 1.0$. Pion and protons that pass all the PID cuts are weighted by $1/eff^i$ when filling a histogram to be used in the analysis.

4.5 TPC Efficiency

The Time Projection Chamber efficiency was studied. Track reconstruction can be affected by tracks that are too close together (so that the track reconstruction algorithm merges them). Ionic space charge accumulation in the TPC volume can also contribute to distortions of the hits' final positions used to reconstruct the tracks. If the distortion is big enough tracks can be split at the middle. Finally, TPC acceptance (for example the dead sector regions in azimuth) also contributes to TPC inefficiencies.

A Monte Carlo simulation is run to create a distribution of particles over a wide range of transverse momentum (0.2 - 5.0 GeV/c). The particles are then embedded in minimum bias (MB) Au + Au collisions and processed by the same reconstruction software that is used in the real events. The efficiency is then computed as the number of tracks (as a function of any desired track variables) matched after reconstruction (reco tracks) divided by the number of simulated input tracks (mc tracks) before embedding. Samples of p, $\bar{p}$, π^+ and π^- were embedded to get the particle dependent TPC efficiencies.

The simulated track parameters used for TPC efficiency measurement are summarized on table 4.3. The events used for embedding the simulated tracks have to be matched to the reference multiplicity and z vertex distribution of the jet triggered events that are used in the present analysis. This is required since different distributions sample the TPC acceptance differently.

There are two ways to match the reference multiplicity vs. z vertex distributions of the Au+Au MB embedded data with the high tower jet triggered Au+Au data. The first method consists on filling the efficiency histograms using all events but weighting each entry. The weight is a function of the embedded event's z vertex and reference multiplicity and its obtained by dividing the triggered events' z vertex vs. reference multiplicity histogram by the corresponding histogram from the embedded events. The second method consists on discarding events from the embedded ones such that the normalized z vertex vs. reference multiplicity distribution of the accepted events is equal to the normalized distribution of the jet triggered events.

The probability distribution that the embedded events have to follow has to be defined. Lets label the reference multiplicity as y and z vertex as x for simplicity. The probability is obtained from the normalized jet-triggered events distributions (call it $P(x, y)$). Pick a reference point (say (x^*, y^*)) it can be used to define a condition that the embedded events have to fulfill as follows. Label the distribution of the embedded evens as $Dist(x, y)$, it has to follow the condition described in Eq. 4.7. Therefore, a cut probability can be defined as in Eq. 4.8. During the analysis a random number(r) between 0 and 1 is generated and an event is accepted only if r $>$ cut probability. This procedure ensures that the distributions of z vertex and reference multiplicity (once normalized) for embedded and jet triggered events are matched.

One pending issue is how to pick the reference point x^*, y^*, this can be done by ensuring that there are enough events at each (x,y) bin in the embedded distribution so as to fulfill the condition from Eq. 4.7. First pick (x^*, y^*) to be the point at which $P(x, y)$ has its maximum content. Loop over the bin contents and define α for each bin as shown at Eq. 4.9. If $Dist(x, y) < \alpha$ keep looping if not then set $(x^*, y^*) \rightarrow (x, y)$ The final value assigned to x^* and y^* are to be used to build the cut probabilities referred to in the last paragraph.

The reference multiplicity and z vertex distribution for the embedded and jet triggered events for two different centrality cuts are shown in figures 4.8, 4.9 and 4.10,4.11 respectively. These plots correspond to the events used to embed the anti-protons, similar plots are obtained for protons and positive

and negative pions.

The TPC correction for the p/π ratio can applied by scaling this ratio by $eff^{\pi}_{TPC}/eff^{p}_{TPC}$. Where eff^{π}_{TPC} (eff^{p}_{TPC}) is the pion (proton) efficiency. The calculated efficiencies ratios are shown in table 4.4. As can be seen the correction is small (negligible compared to systematic errors discussed in section 5) and was therefore not applied to the data.

$$\frac{P(x,y)}{P(x^*,y^*)} = \frac{Dist(x,y)}{Dist(x^*,y^*)} \tag{4.7}$$

$$P_{cut} = 1 - \frac{P(x,y)}{P(x^*,y^*)}\frac{Dist(x^*,y^*)}{Dist(x,y)} \tag{4.8}$$

$$\alpha = \frac{Dist(x^*,y^*)P(x,y)}{P(x^*,y^*)} \tag{4.9}$$

4.6 TOF Efficiency

Every hit in TOF is matched (if possible) to a TPC track by extrapolating the track trajectory. This TPC track-TOF hit matching has its own efficiency. If the matching efficiency differs between protons and pions, then their ratio has to be corrected. It is expected that the TOF matching efficiency is particle independent at high p_T (> 1 GeV/c).

The PID dependency of the TOF matching efficiency was explored by studying pion rich and proton rich particle samples. The particle identifica-

Table 4.3: Simulated tracks parameters for TPC efficiency measurement

Simulated tracks parameters	
Embbeding	AuAu 200 GeV MB RFF
impact parameter	0-20 (MB)
Production	P10ik
Geometry	simu y2010b
Evts	300k
particles/event	0.05
p_T flat (GeV/c)	0.2 - 5.0
ϕ	0 - 6.29
$\|zVertex\|$(cm)	<30
Fit/Max	0.52
DCA(cm)	1.5
Min Fit	15
$\|\eta\|$	1.0

Table 4.4: π/p TPC efficiency values

Jet Triggered Au + Au Events at $\sqrt{s_{NN}}$ = 200 GeV			
0-20%			
$p_T^{min}(GeV/c)$	$p_T^{max}(GeV/c)$	$\langle p_T \rangle\,(GeV/c)$	$eff_{TPC}^{\pi}/eff_{TPC}^{p}$
1.2	1.8	1.42	0.998 ± 0.012
1.8	2.4	2.03	0.999 ± 0.014
2.4	3.0	2.62	0.983 ± 0.012
20-80%			
1.2	1.8	1.42	0.998 ± 0.012
1.8	2.4	2.03	0.996 ± 0.007
2.4	3.0	2.62	1.004 ± 0.012

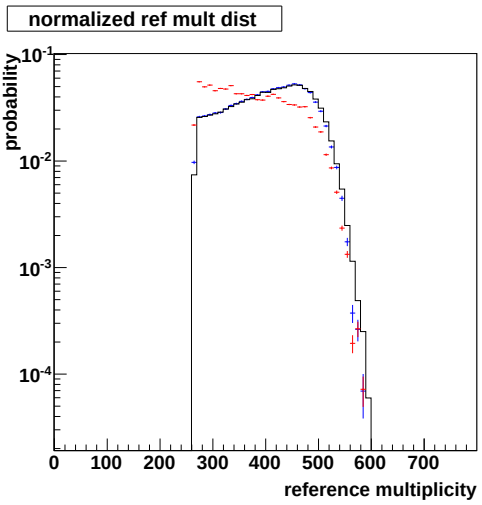

Figure 4.8: Normalized reference multiplicity distributions for jet triggered data (black), embedded minbias data (red) and embedded data after matching (blue) with a 0-20% centrality cut

tion method used to get the samples was based on TPC's energy deposition (dE/dx). This PID method can differentiate between protons and pions up to 1 GeV/c of transverse momentum. The $(\pi^+ + \pi^-)$ and $(\mathrm{p} + \bar{p})$ matching efficiencies below 1 GeV/c were measured and it was assumed that they are the same above 1 GeV/c.

It was necessary to measure the pion and proton matching efficiency eff^{π}_{TOF} (eff^{p}_{TOF}) in a region where the dE/dx PID methodology can be trusted. The value of eff^{π}_{TOF} $/eff^{p}_{TOF}$ used for correction of p/π was evaluated at $p_T = 0.8$ GeV/c and also at $p_T = 0.7$ GeV/c and 1.0 GeV/c in order to look for systematic variations (see section 5.1). TOF matching efficiencies were obtained for the 0-20 % centrality and 20-80 % centrality data sets

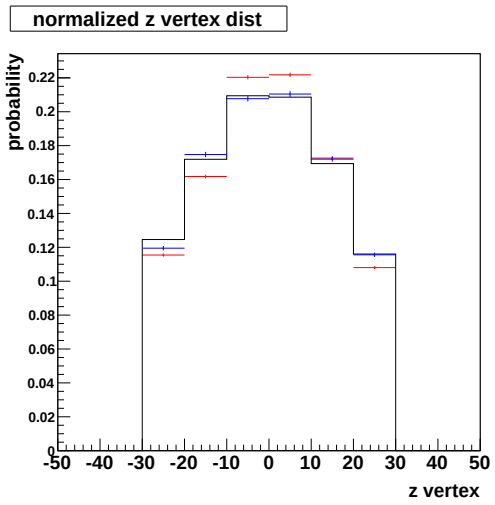

Figure 4.9: Normalized z vertex distributions for jet triggered data (black), embedded minbias data (red) and embedded data after matching (blue) with a 0-20% centrality cut

independently.

The TOF matching efficiency is obtained as follows: All good quality tracks are looped over; a PID decision is made based on the $n\sigma^{i}_{dE/dx}$ value of the track where i corresponds to either pions or protons. Then, a TOF-match decision is made by requiring that the extrapolated TPC track passes through the pad that recorded the TOF hit signal. The TOF hit has to comply with the analysis quality cuts as well. Every TOF hit considered has to fulfill a $\beta >$ 0.01 and time of flight $>$ 1.0 ns cut. The track QA cuts are the same as the ones used throughout the analysis.

Two sets of momentum dependent $n\sigma^{i}_{dE/dx}$ cuts were used in order to quantify the method stability. The cuts are summarized on table 4.5. The

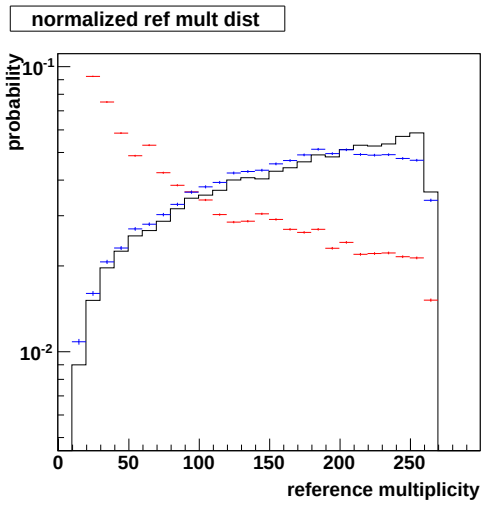

Figure 4.10: Normalized reference multiplicity distributions for jet triggered data (black), embedded minbias data (red) and embedded data after matching (blue) with a 20-80% centrality cut

same cut values worked for 0-20% and 20-80% centralities. Plot 4.12 shows the $\Delta\beta^{-1}/\beta^{-1}$ with a proton mass assumption as a function of momentum for negative protons on 0-20% events. The red band centered at zero corresponds to negative protons. It can be seen that pion contamination below 1.0 GeV/c is small (of the order of less than 10%). Plot 4.13 shows the same plot for pions. In this case the band centered at zero corresponds to pions. Very small contamination coming from electrons and muons can be appreciated below 0.5 GeV/c and contamination from Kaons can be also seen around 1.0 GeV/c. The contamination is at the few percent level though.

Using the tracks that pass the TOF cuts and the ones that pass the TPC quality cuts plots of $eff^{\pi}_{TOF}/eff^{p}_{TOF}$ as function of momentum were

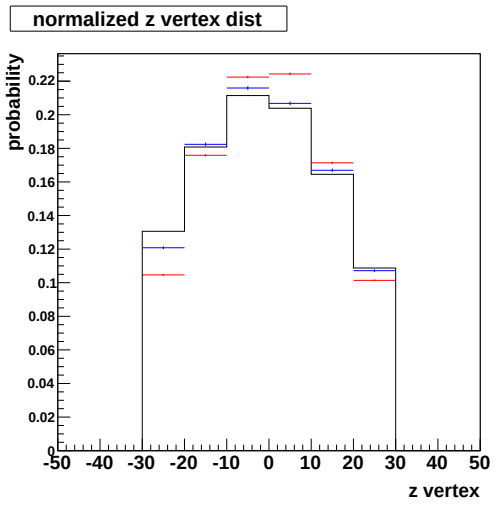

Figure 4.11: Normalized z vertex distributions for jet triggered data (black), embedded minbias data (red) and embedded data after matching (blue) with a 20-80% centrality cut

obtained (see figures 4.14 and 4.15). The ratio of efficiencies is not 1.0 close to 1 GeV/c. The decision was made to approximate the value of the efficiency correction at high p_T by choosing the measured value of $eff^{\pi}_{TOF}/eff^{p}_{TOF}$ at 0.8 GeV/c for the correction of p/π. The plots of eff^{π}_{TOF} $/eff^{p}_{TOF}$ at $p_T > 1.0$ GeV/c show an increase and convergence at 1.0, nevertheless, this is due to the fact that PID capabilities are lost at that high p_T and what is being shown are basically the efficiencies of the same set of particles in both the proton or pion histograms.

The final correction due to TOF matching efficiency is 0.968 at 0-20 % centrality and 0.97 at 20-80 % centrality.

Table 4.5: $n\sigma^{i}_{dE/dx}$ cuts for TOF efficiency measurement

$n\sigma^{\pi}_{dE/dx}$ cuts		
Set 1		
momentum (GeV/c)	max cut	min cut
p < 1	-0.9	-0.5
p > 1	-1.9	-1.5
Set 2		
p < 1	-0.7	-0.5
p > 1	-1.7	-1.5
$n\sigma^{p}_{dE/dx}$ cuts		
Set 1		
momentum (GeV/c)	max cut	min cut
p ϵ 0.2 - 3.5	0.5	1.5
Set 2		
ϵ 0.2 - 3.5	0.5	1.0

4.7 Jet-PID hadrons relative azimuth distributions

One of the goals of this analysis is to extract the jet's near and away side particle yields for comparison. A single heavy ion collision (such as Au+Au, Cu+Cu, Pb+Pb, etc) can include several hard and soft scatterings. A central Au+Au collision (such as the ones studied in this thesis) can produce thousands of particles. It is impossible to completely distinguish the few particles coming from a particular jet in such a rich environment. It is possible to localize high p_T hadrons and even attempt to reconstruct jets although these are only approximations. The only way to extract information of the fragmentation products at lower p_T (say below 2 GeV/c) is statistically.

The hadrons fragmenting from a jet (quark or gluon) in p+p collisions

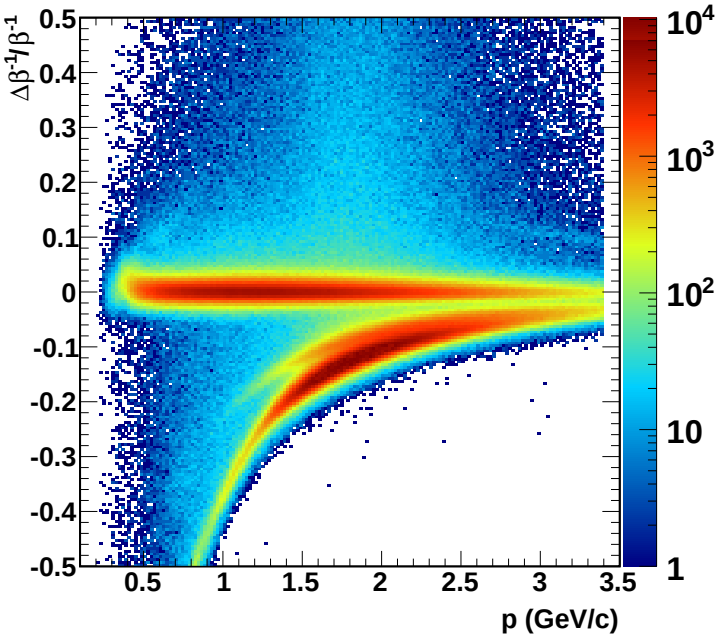

Figure 4.12: Negative Protons $\Delta\beta^{-1}/\beta^{-1}$ vs. momentum plot after set 1 of $n\sigma^{p}_{dE/dx}$ cuts; the η range is 0.6 - 0.8. This plot corresponds to a 0-20% centrality.

are correlated in η, ϕ space with respect to the jet direction. Plotting a distribution of $\Delta\phi \equiv \phi_{trigger} - \phi_{associated}$ for hadrons coming out a p+p collisions results in peaks centered at $\Delta\phi = 0$ and at $\Delta\phi = \pi$. The $\phi_{trigger}$ is the azimuth direction of a trigger chosen based on high p_T cuts and $\phi_{associated}$ is the azimuth direction of all particles in the event fulfilling other cuts. Usually $p_T^{trigger} \geq p_T^{associated}$. This distribution shows the tendency of fragmentation products to move preferably in the jet direction. This does not mean that there are no jet components at wider angles; it is just preferable for them to

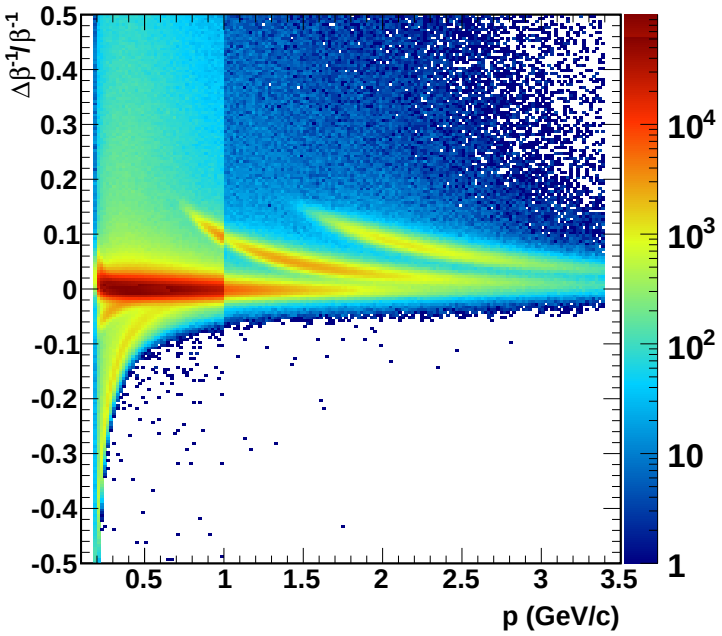

Figure 4.13: Negative Pions $\Delta\beta^{-1}/\beta^{-1}$ vs. momentum plot after set 1 of $n\sigma^{\pi}_{dE/dx}$ cuts; the η range is 0.6 - 0.8. This plot corresponds to a 0-20% centrality.

move close to the jet axis.

The situation is much more complicated in Au+Au collisions since you have to identify the jets' constituents on top of an uncorrelated background. The jet might be correlated with background particles if there is re-scattering of the hadrons, medium induced gluon bremsstrahlung of the parton (jet) or other interactions. Other hard and soft scatterings present in the collision are uncorrelated with the jet and become part of the background in any $\Delta\phi$ distribution.

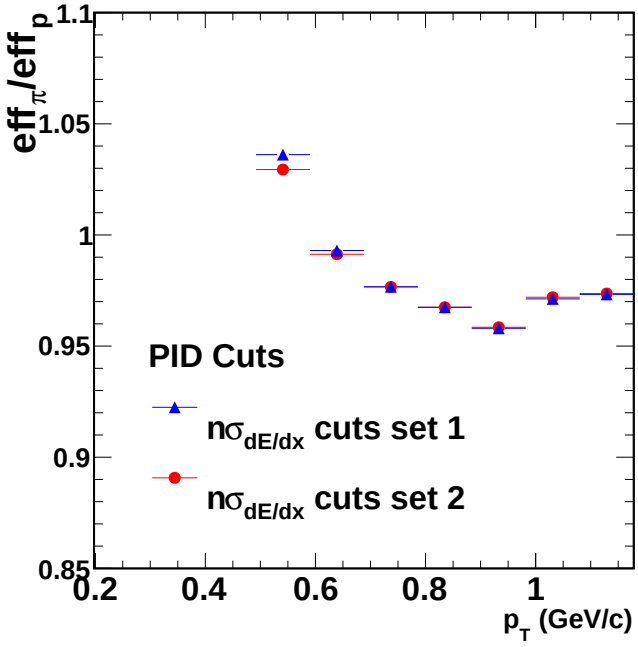

Figure 4.14: $eff^{\pi}_{TOF}/eff^{p}_{TOF}$ versus transverse momentum for the two $n\sigma_{dE/dx}$ cuts used in the analysis. Only the region were PID using dE/dx can be trusted is shown. This plot corresponds to a 0-20% centrality.

There are several ways to extract jet signals in such high multiplicity environment. One approach is to calculate the Pearson's correlation on $\Delta\eta$ vs $\Delta\phi$ using either all the particles in an event or selecting windows of p_T. This 2D correlations have the advantage of disentangling the $\Delta\eta$ and $\Delta\phi$ contributions to the jet signal. These correlations are compared to similarly constructed ones from p+p collisions [55]. Other, similar approach, is to trigger on a high p_T hadron using it as a proxy of a jet. The hadron's azimuth direction is used to reconstruct a per trigger $\Delta\phi$ distribution using all other particles in

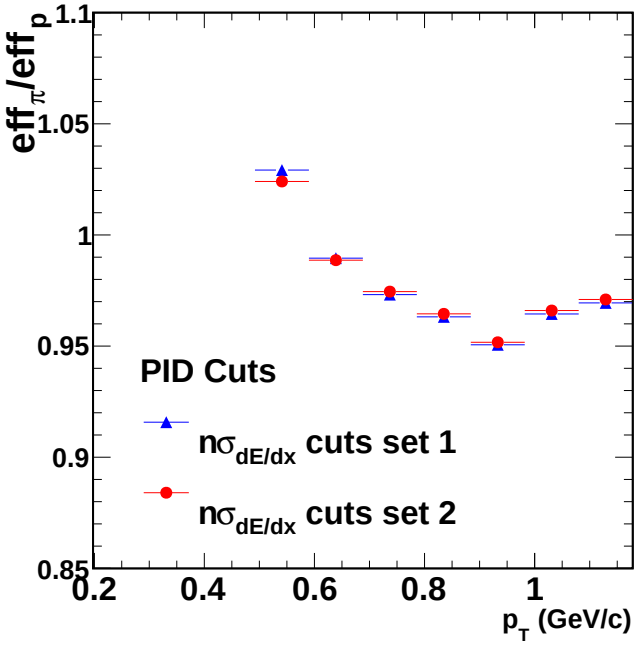

Figure 4.15: $eff^{\pi}_{TOF}/eff^{p}_{TOF}$ versus transverse momentum for the two $n\sigma_{dE/dx}$ cuts used in the analysis. Only the region were PID using dE/dx can be trusted is shown. This plot corresponds to a 20-80% centrality.

the event that fulfill some p_T cut condition. This approach shifts the focus to the high momentum part of a jet's signal. It has been shown that the $\Delta\phi$ distribution yield on the away side from the trigger on central Au+Au collisions gets reduced compared to the signal on p+p collisions. The momentum cannot disappear and a full study of the $\Delta\phi$ distribution to the lowest possible p_T in STAR's TPC acceptance has to be done to see where the energy goes. A third approach, the one chosen by the author, is to enhance the kinematic reach of the trigger particle by reconstructing a jet using a jet finding algorithm

first [11,16,56]. This gives a handle on the jet axis at higher energies than when using a high momentum track as a jet proxy. A per trigger jet $\Delta\phi$ distribution is obtained using different p_T cuts in the associated particles to study the jet yield content as a function of momentum. The jet trigger conditions used in this analysis might create a surface bias. This bias, in turn, biases the recoiling jet (from a back to back hard scattering) to traverse the medium created in Au+Au collisions (see section 4.3).

4.7.1 High Tower

This analysis benefited from the on line High Tower trigger to bias the selected event sample to contain events where at least one hard scattering took place. The on line trigger requires 4.3 GeV of energy deposition on a single tower of the BEMC (see Section 4.1). In this study an off line trigger of 5.0 GeV was further required. This allows to avoid the trigger onset bias in the jets distribution. The new trigger particle is obtained by looping over all calorimeter towers that got hit in an event after quality assurance cuts. The energy deposited by MIPs (minimum ionizing particles) and electrons in the towers was subtracted before the 5 GeV trigger is looked for in order to avoid double counting.

4.7.2 Trigger Jet

The jet finding algorithm and cuts were discussed in section 4.3. The trigger jets were required to contain the High Tower as one of their constituent

particles. This jet has to be found event by event since the Jet Finding Algorithm returns a list of candidate jets present on an event. Every jet contains a list of tracks and towers that are associated with the given jet. It is necessary to loop over the jets present on an event by starting with the most energetic one and look for a particle that matches the High Tower η and ϕ coordinates. Matching is defined by the inequalities: $\phi_{i \in jet} - \phi_{HighTower} \leq 0.001$ and $\eta_{i \in jet} - \eta_{HighTower} \leq 0.001$.

4.7.3 $\Delta\phi$ distribution

One of the objectives of the present study is to obtain a per trigger jet $\Delta\phi$ distribution for several p_T bins. Where $\Delta\phi \equiv \phi_{jet} - \phi_{assoc}$. The maximum p_T that could be analyzed was constrained by the jet statistics and PID methodology capabilities. Protons and pions can be identified by the methodology describe in section 4.4 up to a momentum of 3.4 GeV/c and η = 1.0. Note that all tracks with pseudorapidity less than 1.0 are taken into account. This produces a non uniform distribution on transverse momentum. Therefore, the per trigger jet $\Delta\phi$ distributions shown in this analysis are not to be taken as a final measurement by themselves as they suffer from the acceptance deficiencies due to the non uniform distribution. The ratios (of proton yield over pion yield) that will be obtained from those $\Delta\phi$ distributions are not going to be affected by this inefficiency since it cancels. The underlying assumption for the cancellation is that the pion and proton production does not have a very strong and different η dependency for the same p_T.

After a trigger jet is identified in an event histograms of $\Delta\phi$ vs. p_T^{assoc} are filled out with tracks that fulfill all of the QA cuts. The difference in pseudorapidity between the jet and an every associated particle is obtained to correct for a geometric acceptance at fill time as will be further described in the next section. The $n\sigma^i_{dE/dx}$ and $\Delta\beta^{-1}/\beta^{-1}$ values for each particle are computed to decide whether the corresponding histogram for particle "i" is to be filled. The $\Delta\beta^{-1}/\beta^{-1}$ is obtained by using an "i" mass assumption below 1.8 GeV but using pion mass assumption for momentum above 1.8 GeV. The final decision regarding whether a particle belongs to the "i" species comes from the probability distribution (as function of p and η) defined at Eq. 4.6. A probability cut of 0.75 is used in the analysis since it results in 90% or more purity of protons and pions as discussed previously. The histogram entry is weighted by $1/eff^i$ defined in section4.4 to correct for the cut probability inefficiency.

The final $\Delta\phi$ distribution for a p_T bin is obtained by projecting the 2D $\Delta\phi$ vs. p_T^{assoc} histograms into the specific p_T window and dividing it by the number of jet triggers and bin width.

4.7.4 Mix Event Correction

The per trigger jet $\Delta\phi$ distributions of each particle suffer from acceptance inefficiencies. A complete sector from the TPC (section 3.3) was disabled on Run10. This "hole" in the acceptance creates an artificial asymmetry on the $\Delta\phi$ distributions. These detector effects can be corrected for by taking

the ratio of the distribution coming from the events and a distribution where the jet comes from one event and the associated particles come from another event (i.e. they are uncorrelated). The mix event distributions will have all of the detector acceptance inefficiencies without the jet signal that one is hoping to extract.

The events used to select a jet and associated particles should have similar collision vertex. This is done to replicate the sibling events distributions as close as possible. A jet is only mixed with another event if the condition $|zV_{jetevent} - zV_{mixevent}| < 5$ cm is fulfilled. The difference in x and y position of the collision vertex for the mix event was ~ 400 microns. Also, a single jet is mixed with 30 different events to increase the statistics. The steps to be followed to correct for detector inefficiencies by using mix events are outlined below:

The first step is to fill histograms on $\Delta\phi = \phi_{jet} - \phi_{track}$ vs p_T for each zVertex bin being considered. This is done for all of the jet triggered events and for up to 30 mix events. The mix events histograms are filled by saving the information of a given event's jet trigger and using it to obtain $\Delta\phi$ with tracks from other similar events. The similarity of events was discussed in previous paragraphs.

Every entry of the $\Delta\phi$ histograms is weighted by a $\Delta\eta = \eta_{jet} - \eta_{track}$ dependent correction. The correction is needed to get rid of the trivial geometrical acceptance on $\Delta\eta$. The tracks used from the TPC extend to one unit of $|\eta|$ and the jets to 0.6. Therefore, there are more combinations of $\Delta\eta = 0$

than $\Delta\eta = 1.6$.

The pseudorapidity geometric correction can be understood as follows. A $\Delta\eta = 0$ entry can be obtained by placing the jet at an η position that goes from -0.6 to 0.6 (the cuts imposed in the trigger jets) and placing the track at the same η. On the other hand, the maximum value $\Delta\eta$ can have comes form placing a track at $\eta = 1.0$ and a jet at $\eta = -0.6$, that is, only one possibility. Putting it in a more mathematical way, take the η_{jet} and η_{track} as flat distributions. Then, the number of possible pairs that give a particular $\Delta\eta$ is obtained by convolving the distributions.

$$N_{pairs}(\Delta\eta) = \int_{-\eta_{jet}^{max}}^{\eta_{jet}^{max}} d\eta_{jet} \int_{-\eta_{track}^{max}}^{\eta_{track}^{max}} d\eta_{track} \delta((\eta_{jet} - \eta_{track}) - \Delta\eta) \tag{4.10}$$

$$f(\Delta\phi) = \begin{cases} 1/1.2 & \text{if } \Delta\eta \leq 0.4 \\ 1/(1.6 - \Delta\eta) & \text{otherwise} \end{cases} \tag{4.11}$$

The inverse of the functional form obtained by Eq. 4.10 is used to weight both the sibling and mix event $\Delta\phi$ vs. p_T distributions at fill time. The inverse function for this particular analysis η cuts takes the form given in Eq. 4.11. This correction gets ride of the geometrical $\Delta\eta$ acceptance correlation.

After the $\Delta\eta$ correction and once the $\Delta\phi$ vs. p_T histograms are filled, they are projected on the $\Delta\phi$ axis using slices on the p_T corresponding to the region of interest (p/π enhancement). After this step $\Delta\phi$ distribution histograms for each particle (proton and pions), for each transverse momentum

bin considered, for mix and sibling events, and for each z vertex bin considered are left. For the sake of simplicity, lets pick one p_T bin and one particle species to describe the mix event correction scheme. Call the sibling(mix) histograms $Hist_{sib}\left(\Delta\phi\right)_{z_i}$ ($Hist_{mix}\left(\Delta\phi\right)_{z_i}$).

The following normalization scalers will be used:

$$\begin{aligned} Norm &= \sum_{z_i}\sum_{\Delta\phi} Hist_{mix}\left(\Delta\phi\right)_{z_i} \\ Norm_{z_i} &= \sum_{\Delta\phi} Hist_{mix}\left(\Delta\phi\right)_{z_i} \\ Sib_{raw} &= \sum_{z_i}\sum_{\Delta\phi} Hist_{sib}\left(\Delta\phi\right)_{z_i} \end{aligned} \tag{4.12}$$

The Norm normalization scaler (from Eq. 4.12) is the sum over all z vertex bins used in the analysis of the integral of the mix event $\Delta\phi$ histograms. The $Norm_{z_i}$ scaler defined on the same equation is the integral of the mix event $\Delta\phi$ histograms for each vertex z bin. The Sib_{raw} scaler from Eq. 4.12 is the total number of counts from the same event $\Delta\phi$ histograms and for all z vertex bins considered. This last scaler will be used to scale the histograms once a corrected $\Delta\phi$ distribution is obtained in order to recover the original number of counts.

The first two scalers shown at Eq. 4.12 are used to define a weight probability: $w(z_i) = Norm_{z_i}/Norm$. This weight represents the relative contribution coming from a given z vertex to the mix histograms if all of the z vertex bins are added. It can also be thought of as the probability that a given mix event histogram belongs to a given z vertex. This weight is necesary since the z vertex distribution of the jet triggered events is not flat.

The next step is to normalize each histogram to one and take the sibling over mix ratio. It is at this step were the detector acceptance effects get canceled. After this ratio is taken the correct shape of the $\Delta\phi$ distribution is gotten but not the right scale yet.

$$\begin{aligned} Hist^{'}_{sib}\left(\Delta\phi\right)_{z_i} &= \frac{Hist_{sib}\left(\Delta\phi\right)_{z_i}}{\sum_{\Delta\phi} Hist_{sib}\left(\Delta\phi\right)_{z_i}} \\ Dist\left(\Delta\phi\right)_{z_i} &= \frac{Hist^{'}_{sib}\left(\Delta\phi\right)_{z_i}}{Hist^{'}_{mix}\left(\Delta\phi\right)_{z_i}} \end{aligned} \tag{4.13}$$

The contributions to the $\Delta\phi$ distributions over all z vertex bins have to be added. The distributions defined on Eq. 4.13 are first normalized to one. Then, they can be taken as a probability of finding a track (whether it is part of the uncorrelated background or the jet signal) at a relative azimuth ($\Delta\phi$) with respect to the jet axis. Multiplying the weight ($w(z_i)$) with each $Dist\left(\Delta\phi\right)_{z_i}$ results on a multiplication of probabilities: Probability of being part of the event from the z vertex bin labeled z_i times the probability of being a track with $\Delta\phi$. The probability distribution from the weighted sum is computed as shown on Eq. 4.14. This is the z vertex weighted probability of having a track at $\Delta\phi$ from the jet axis.

$$Dist\left(\Delta\phi\right) = \sum_{z_i} w(z_i) Dist^{'}\left(\Delta\phi\right)_{z_i} \tag{4.14}$$

Finally, to recover the geometric acceptance corrected sibling distribution, the $\Delta\phi$ distributions have to be scaled by the original raw distributions

integral and divided by the number of trigger jets. The final per trigger jet $\Delta\phi$ distribution formula is shown on Eq. 4.15 where NumJetTrigger is the number of trigger jets, $binsize_{\Delta\phi}$ is the bin size of the $\Delta\phi$ distributions histograms and Sib_{raw} is the normalization constant defined at 4.12. The $\Delta\phi$ distributions at this stage contain contributions from both background and jet signal particles.

$$\frac{1}{N_{jet}}\frac{dN}{d\Delta\phi} = \frac{Sib_{raw} \cdot Dist\,(\Delta\phi)}{NumJetTrigger \cdot binsize_{\Delta\phi}} \tag{4.15}$$

4.8 Azimuth distributions model

The proton and pion $\Delta\phi$ distributions (Eq. 4.15) described in the previous section are used to obtain the jet yields from them. The $\Delta\phi$ distribution is assumed to include contributions from jet fragments and uncorrelated background. One way to extract the jet-related fragments is to model the distributions with a given signal + background model and then integrating the signal part over the full azimuth difference range.

The p_T intervals analysed are: $[1.2, 1.8)$, $[1.8, 2.4)$ and $[2.4, 3.0)$ wich correspond to average transverse momentum($\langle p_T \rangle$) of 1.42, 2.03 and 2.62 GeV/c respectively.

The mathematical function that is used to represent the $\Delta\phi$ distribution consists of a constant offset, two Gaussian peaks and, optionally, a quadrupole term. The two Gaussian peaks represent the near side (towards the trigger jet) and away side (recoiling from the trigger jet) jet contributions to the

$\Delta\phi$ distributions. These contributions can come from back to back jet pairs and isolated jets. The constant offset term models combinatoric background contributions to the distribution. The parameters of the Gaussian components of the model are obtained by fitting the distributions. These Gaussians can then be integrated to obtain the jet yields on the near and away sides.

The $\Delta\phi$ distribution model used in this analysis is shown in Eq. 4.16. $Y_{near}(Y_{away})$ represents the near(away) side jet yield and B the uncorrelated background. Eq. 4.17 shows an alternative model which allows for the possibility of a quadrupole contribution ($2VCos(\Delta\phi)$) term. The quadrupole term is a novel functional form that has been found in minimum bias $\Delta\eta$ vs. $\Delta\phi$ correlations in Au+Au collisions at RHIC energies [57]. This term is not found in p + p collisions and is usually attributed to elliptic flow [58]. One way to measure whether the term is necessary in our $\Delta\phi$ distributions is to fit them with the quadrupole component included and look for a statistical significant contribution of this term. The difference in proton an pion yields while including a quadrupole term are taken into account in the systematic errors section 5.

$$\frac{1}{N_{jet}}\frac{dN}{d\Delta\phi} = Y_{near}e^{-\frac{1}{2}(\frac{\Delta\phi}{\sigma_{near}})^2} + Y_{away}e^{-\frac{1}{2}(\frac{\Delta\phi-\pi}{\sigma_{away}})^2} + B \tag{4.16}$$

$$\frac{1}{N_{jet}}\frac{dN}{d\Delta\phi} = Y_{near}e^{-\frac{1}{2}(\frac{\Delta\phi}{\sigma_{near}})^2} + Y_{away}e^{-\frac{1}{2}(\frac{\Delta\phi-\pi}{\sigma_{away}})^2} + B(1 + 2VCos(\Delta\phi)) \tag{4.17}$$

The $\Delta\phi$ distributions (for each p_T bin and particle species) are fit with the model (4.16) a minimum of 50 times. The fit is done using ROOT's chi squared minimization fitting method [59]. The errors given by the minimization routine are computed using the MINOS technique. Each time the model is fitted, the initial parameters (5 or 6 if quadrupole is included) are chosen randomly from a uniform distribution between suitable maximum and minimum values. The set of parameters giving the minimum $(\chi)^2$ are chosen to fit the distribution one last time.

4.9 Proton over pion ratios

Once the parameters of the model function are determined, the near and away side Gaussians from the model function are integrated over the complete $\Delta\phi$ range. The integration is done numerically using ROOT's Gauss-Legendre Method with 10,000 sampling points [59]. The Gaussian's parameters and its correlated errors as given by the fit are used to estimate the integral result errors. Each Gaussian's parameters' errors and covariant matrix elements are used to create 1000 samples of a multivariate normal distribution. This step is done by using the statistical computing language R [60]. Points in this distribution are sampled and used to define the Gaussian. The Gaussian is then integrated using R subroutine for numerical integration [60]. This gives a distribution of 1000 integrals. The standard deviation of the distribution is taken as the error in the integral (jet yield).

The proton yield is divided by the pion yield for each p_T bin to get

the p/π final results in the near and away sides. The p/π statistical errors are computed by taking into account each particles' yield errors and doing error propagation. The systematic errors are to be discussed in section 5.

Chapter 5

Systematics

The different systematic checks performed in this analysis are discussed in this section. They include the TOF efficiency correction, the PID methodology and the inclusion of a quadrupole term in the $\Delta\phi$ distributions model fits.

5.1 TOF efficiency systematic errors

The correction to the p/π ratio measurements due to differences in p and π TOF matching efficiencies was described earlier in this thesis (see section 4.6). The final correction values of $eff^{\pi}_{TOF}/eff^{p}_{TOF}$ where obtained by evaluating the efficiencies for each particle at $p_T = 0.8$ GeV/c. The ratio of efficiencies decreases going from $p_T \sim 0.2$ GeV/c up to 1.0 GeV/c. Even though it is expect that the value of the efficiencies ratio stabilizes at the higher p_T used for the p/π investigated in the present analysis it is not clear whether the final value is going to be 1.0

The inaccuracy of the estimation of the final value of $eff^{\pi}_{TOF}/eff^{p}_{TOF}$ is included in the final ratios systematic. Efficiency corrections are obtained by evaluating the matching efficiencies at $p_T = 0.7$ and 1.0 GeV/c. This interval

is chosen since these are the highest p_T values at which we can trust the PID using dE/dx (independent of TOF). The variation on the efficiencies ratio ($eff^{\pi}_{TOF}/eff^{p}_{TOF}$) provides an estimate of how well the PID dependent TOF matching efficiency correction is known.

Therefore, the final correction used in the analysis consist of $eff^{\pi}_{TOF}/eff^{p}_{TOF}$ evaluated at $p_T = 0.8$ GeV/c plus $eff^{\pi}_{TOF}/eff^{p}_{TOF}$ evaluated at $p_T = 1.0$ GeV/c and minus $eff^{\pi}_{TOF}/eff^{p}_{TOF}$ evaluated at $p_T = 0.7$ GeV/c. The final values of the correction for 0-20% centrality are shown in Eq. 5.1 and the final values for 20-80 % centrality are shown in Eq. 5.2:

$$\frac{eff^{\pi}_{TOF}}{eff^{p}_{TOF}} = 0.968^{+0.009}_{-0.012} \tag{5.1}$$

$$\frac{eff^{\pi}_{TOF}}{eff^{p}_{TOF}} = 0.97^{+0.02}_{-0.01} \tag{5.2}$$

5.2 Particle Identification systematic errors

In order to assign a PID systematic error to the p/π measurement, the PID cut probability ($P(p, \eta, \pi, \Delta\beta^{-1}_{\pi}/\beta^{-1}, n\sigma^{\pi}_{dE/dx}) \geq 0.75$) was varied from its default value of 0.75 to 0.65 and 0.85. The parameters that define each particle's pdf on Eq. 4.5 are the same that were obtained by fitting the jet-triggered events' data. There is a set of parameters for each centrality being considered. The new cut probabilities were used to calculate new PID cut efficiency corrections. The way the efficiency corrections are applied and constructed is

described on section 4.4. Once the efficiency corrections are obtained, the $\Delta\phi$ distributions are reproduced by using each of the two different PID cut probability values and their respective PID cut efficiency corrections (which are applied while filling the $\Delta\phi$ distribution histograms and are a function of the particle's momentum and η). Note that the pions and protons used to re-create the $\Delta\phi$ distributions come from slightly different samples due to the different PID cut. This is a great check that the final results do not depend on the chosen PID methodology. The different efficiency corrections (if properly calculated) should produce the same (correct) scaling in the $\Delta\phi$ distributions. Any difference in the final p/π ratios are considered part of the systematic errors.

After the newly generated $\Delta\phi$ distributions are obtained, the rest of the analysis steps remain unchanged. That means that the near and away side jet yields are modeled, fitted and extracted just as described in section 4.8. Similarly, the proton/pion ratios are still obtained following the procedure outlined in section 4.9.

In summary, the assigned error on the trigger jet's near and away side p/π ratios (as function of p_T) comes from the difference in final ratios obtained with the default PID cut probability (0.75) and the new/changed PID cut probabilities (0.65 and 0.85).

The p/π ratios for each centrality and p_T bins on the jet's near and away sides and for each PID probability cut are summarized on table 5.1.

Table 5.1: PID cut probabilities dependence of trigger jet's near and away sides p/π (errors quoted are statistical)

p/π **values**			
0-20% centrality jet's near side p/π			
p_T Bin (GeV/c)	prob = 0.65	prob = 0.75	prob = 0.85
$[1.2-1.8)$	0.23 ± 0.02	0.22 ± 0.02	0.21 ± 0.02
$[1.8-2.4)$	0.54 ± 0.03	0.51 ± 0.03	0.47 ± 0.03
$[2.4-3.0)$	0.53 ± 0.06	0.49 ± 0.03	0.48 ± 0.03
0-20% centrality jet's away side p/π			
$[1.2-1.8)$	0.41 ± 0.02	0.40 ± 0.02	0.40 ± 0.02
$[1.8-2.4)$	0.76 ± 0.03	0.76 ± 0.03	0.70 ± 0.03
$[2.4-3.0)$	1.06 ± 0.13	0.94 ± 0.05	0.93 ± 0.05
20-80% centrality jet's near side p/π			
p_T Bin (GeV/c)	prob = 0.65	prob = 0.75	prob = 0.85
$[1.2-1.8)$	0.26 ± 0.02	0.26 ± 0.02	0.26 ± 0.02
$[1.8-2.4)$	0.46 ± 0.03	0.46 ± 0.03	0.46 ± 0.03
$[2.4-3.0)$	0.32 ± 0.02	0.37 ± 0.02	0.35 ± 0.03
20-80% centrality jet's away side p/π			
$[1.2-1.8)$	0.35 ± 0.02	0.33 ± 0.02	0.34 ± 0.02
$[1.8-2.4)$	0.45 ± 0.02	0.46 ± 0.02	0.48 ± 0.02
$[2.4-3.0)$	0.47 ± 0.03	0.54 ± 0.02	0.52 ± 0.03

5.3 Azimuth distributions model systematics

The model used to fit the proton and pion $\Delta\phi$ distributions (see Eq. 4.16) consist of a near side Gaussian, away side Gaussian and a constant offset. This model is used for its simplicity and capacity to properly describe the $\Delta\phi$ distributions for protons, pions and charged hadrons in all the p_T bins analyzed. Based on previous results that demonstrate that there is an quadrupole component in two particle correlations in heavy ion collisions at STAR energies, it was decided to explore the possibility that the $\Delta\phi$ distributions measured in the present study can include a $cos(2\Delta\phi)$ component. This term could have a connection with the observed quadrupole in $\sqrt{s_{NN}} =$ 200 GeV Au + Au collisions particle correlations (see references [57, 58] and section 4.8). According to [61] the quadrupole component of $\Delta\phi$ distributions plus background can be parameterized as in Eq. 5.3 where $\nu_2(p_T^{trigger})$ and $\nu_2(p_T^{associated})$ are the coefficients of the Fourier expansion shown at 5.6 for the distributions of trigger particles(or jets) and the distributions of associated particles respectively. The background of Eq. 5.3 corresponds to $\Delta\phi$ distribution with $\Delta\phi = \phi^{trigger} - \phi^{associated}$. The quadrupole component is often attributed to elliptic flow in momentum space originating from a geometrical anisotropy of the collision; this anisotropy is thought to have its origins on the overlapping shape of the two colliding nuclei.

$$B\left(1 + 2\nu_2(p_T^{trigger})\nu_2(p_T^{associated})Cos(2\Delta\phi)\right) \tag{5.3}$$

The Lorentz - invariant particle distribution can be parameterized as shown in Eq. 5.4. Where ϕ is the particle's azimuth and Ψ_r the reaction plane angle. The reaction plane is the idealized plane defined by the idealized impact parameter (distance between the colliding ions centers) and the ions beam direction. It is estimated (and named event plane) by building flow vectors and then using Eq. 5.5. The event plane can be computed using any of the harmonics present on the distribution (n) but is generally constructed using the 2nd harmonic. The 2nd harmonic is a vector with components x_2, y_2 coming from the complete Fourier decomposition of any distribution in azimuth as shown in Eq. 5.6 [62].

$$E\frac{d^3N}{d^3p} = \frac{1}{2\pi p_T}\frac{d^2N}{d^2p_T dy}\left(1 + \sum_{n=1}^{\infty} 2\nu_n Cos(n\left(\phi - \Psi_r\right))\right) \tag{5.4}$$

$$\begin{aligned} X_n &= \sum_i w_i Cos(n\phi_i) \\ Y_n &= \sum_i w_i Sin(n\phi_i) \\ \Psi_n &= \left(tan^{-1}\frac{\sum_i w_i Sin(n\phi_i)}{\sum_i w_i Cos(n\phi_i)}\right)/n \end{aligned} \tag{5.5}$$

$$r(\phi) = \frac{x_0}{2\pi} + \frac{1}{\pi}\sum_{n=1}^{\infty}\left[x_n Cos(n\phi) + y_n Sin(n\phi)\right] \tag{5.6}$$

These concepts can be understood as follows. The azimuth distribution of particles produced in heavy ion collisions can be described by a Fourier expansion with cosine and sine terms. Each $cos(\phi_n)$ and $sin(\phi_n)$ pair (along

with its coefficients) define the n^{th} harmonic contribution to the expansion. The n^{th} harmonic is a periodic modulation with n maxima over the 2π period. Therefore, any distribution in full azimuth can be decomposed as a sum of one or more (infinite if necessary) of such harmonics. In heavy ion collisions it is assumed that the direction of the harmonic vector defined earlier points in the direction of the reaction plane due to geometrical reasons [62]. This way only cosine terms form Eq. 5.6 survive in Eq. 5.4.

The alternative $\Delta\phi$ fitting model including the quadrupole term is shown in Eq. 4.17. The coefficient V on this model is related to the $\nu_2^{trigger}$ and ${\nu_2}^{associated}$ as shown in Eq. 5.7. This equation implies that the trigger (a jet in our case) does have some ν_2 modulation as well. This is a jet-reaction plane correlation, not to be confused with a jet flow. The purpose to include the quadrupole term in the $\Delta\phi$ distributions model is to measure its possible contribution to the $\Delta\phi$ signal + background by means of the fit. This way, the near and away side jet yields (for protons and pions) can be obtained under the assumption that the quadrupole term does contribute to the background.

$$V = \nu_2(p_T^{trigger})\nu_2(p_T^{associated}) \tag{5.7}$$

The quadrupole term coefficient is obtained from the model fit by constraining its value to be within limits coming from proton, pion and jets ν_2 that have been measured in Au + Au collisions [63]. The jet ν_2 is constrained to be smaller than 0.12 at all centralities [64]. The pion v_2^{π} is constrained to be

≤ 0.12 (0.2) for the 0-20% (20-80%) most central events. [63]. The limits imposed in ν_2's translate to limits of V such that V ≤ 0.014 (0.024) in the central (peripheral) events. Once the values of the V = $(\nu_2^{jet})(\nu_2^{\pi})$ are obtained from the fits, they are used to set the values of the V = $(\nu_2^{jet})(\nu_2^{p})$. For the 0-20% centrality $\nu_2^{\pi} = \nu_2^{p}$ for all p_T bins. For the 20-80% centrality $\nu_2^{p} = (0.9)\nu_2^{\pi}$, $\nu_2^{p} = \nu_2^{\pi}$ and $\nu_2^{p} = (1.1)\nu_2^{\pi}$ for $\langle p_T \rangle$ bin equal to 1.4, 2.0 and 2.6 respectively [63]. The final values used can be read from the fits found in the appendix 1.

Once the quadrupole contribution to the background is obtained, the p/π ratios are measured from the Gaussian integrals after background subtraction. The difference is included as a systematic error in the final p/π plots.

It is important to point out that another option for model systematic evaluation is to use exact ν_2 values measured elsewhere. These measurements are usually obtained by first measuring the event plane using particles at high η. Unfortunately, the event plane could still have contamination coming from near side jets correlated particles. An attempt to resolve this issue is to perform four particle cumulants analysis. Several studies use an average of the two measurements as an estimate of the true ν_2 value. While this approach is valid, It was preferred to use those values as constrains for the fit model and then measure the $\nu_2^{trigger}\nu_2^{associated}$ from the fit. The reason to do that is that the ν_2 measurements elsewhere do not necessarily comply with all the cuts and jet-trigger bias particular of the present analysis and using minimum bias ν_2 measurements could lead to an overestimation of jet signal.

5.4 Track quality cuts systematic errors

The track quality cuts imposed in this analysis serve the purpose of rejecting tracks that do not represent a good measurement of the particle they belong to. The effect of the cuts on protons and pions is though to be similar (with the yield of both either increasing or decreasing as a response to changing the track cuts). The correlated error thus cancels in the p/π ratios as is not included in the final measurement.

Chapter 6

Results

The results are presented divided in two centrality sets. For each centrality, the $\Delta\phi$ distributions of protons and pions and for different p_T intervals are shown. The resulting standard deviations of the Gaussian distributions used to describe the near and away(recoiling) side jets are presented. The per trigger jet proton and pion p_T distributions (obtained by integrating the corresponding Gaussians from the model) are presented too. The results section concludes by showing the p/π ratios as function of p_T for each centrality in the inclusive (jet signal + background), near and away sides from the trigger jet.

6.1 Central events (0 - 20%)

Proton and pion $1/N_{jets}dN/d(\Delta\phi)$ distributions and p_T distributions of the jet yield for the near and away sides are shown in this section.

6.1.1 Protons

The proton $\Delta\phi$ distributions divided by the number of trigger jets $(1/N_{jets}dN/d(\Delta\phi))$ for the three p_T bins considered in the present analysis

and 0-20% centrality events are shown in Fig. 6.1. These distributions are fit with the flat background model (4.16). The Gaussian σ's are plotted in Fig. 6.2 where it can be seen that the away side Gaussians are wider than the near side ones, this suggests some medium induced broadening. The signal jet is defined as the yield computed by the integral of the jet Gaussian over all azimuth after background subtraction. The background model is used to get signal/background ratios as function of p_T for protons. The signal/background ratios are shown in Fig. 6.3 where an increasing trend with proton's p_T is observed in both the near and the away sides. This trend implies that the signal/background ratio improves with proton's p_T. Finally, proton p_T distributions normalized by the reciprocal of the number of trigger jets are shown in Fig. 6.4. The proton yields correspond to the jet signal in the near or away sides of the $\Delta\phi$ distribution model(refer to section 4.8). The near, away and incluside(all azimuth with jet + background signal) distributons are plotted in red, blue and black respectively. Note that the track cuts used in the analysis (momentum < 3.4 and $\eta < 1.0$) produced an inefficiency at high p_T that was not corrected for in those plots. The pions are affected by the same inefficiency and we only draw our physics conclusions from the p/π ratios shown later where this inefficiencies cancel.

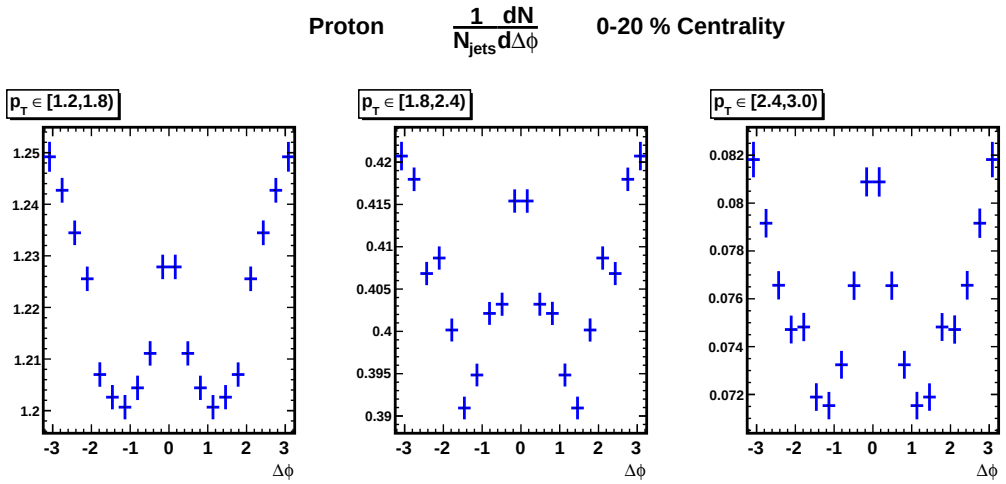

Figure 6.1: Per trigger jet $\Delta\phi$ distributions of protons for three p_T bins. Note the zero suppressed y axis

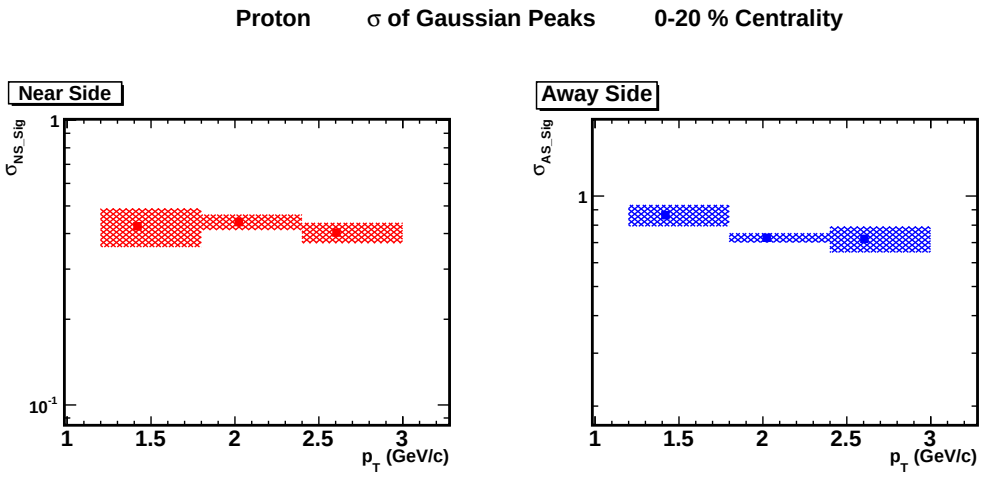

Figure 6.2: Protons Gaussian's σ for the near(shown in red) and away side(blue) jet directions for three different p_T bins. The errors are the statistical errors provided by the fit.

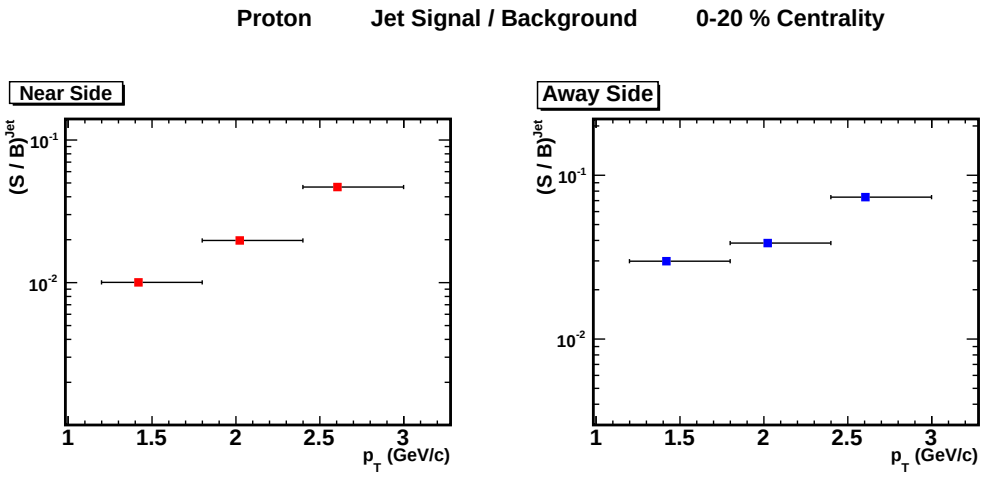

Figure 6.3: Protons's jet signal over background for the near(shown in red) and away side(blue) jet directions for three different p_T bins.

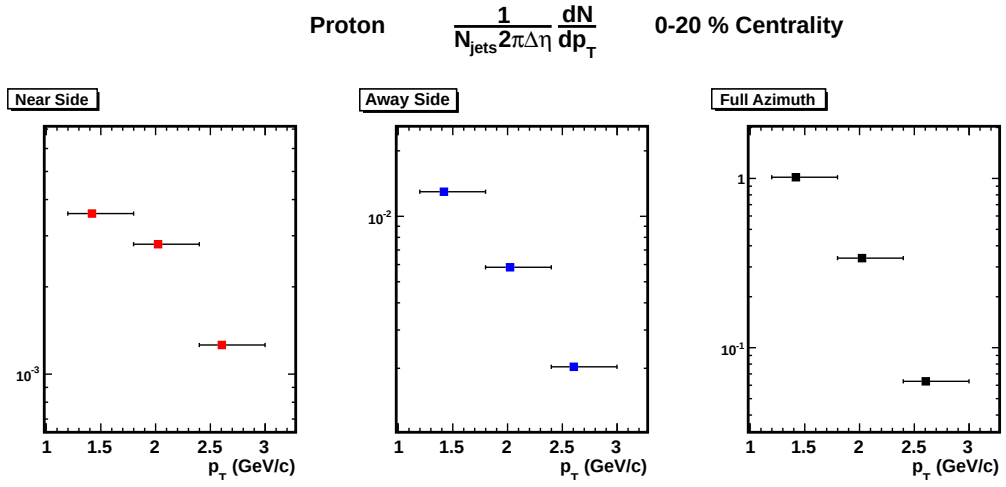

Figure 6.4: Protons' p_T distribution in all azimuth(black), the near side jet(red) and the away or recoiling side jet(blue).

6.1.2 Pions

This section includes the pions results. Per trigger jet pion $\Delta\phi$ distributions, Gaussian σ's and jet signal/background ratios for pions are shown in figures 6.5, 6.6 and 6.7 respectively. The away side Gaussians are wider than the near side ones just like in the proton's case but this time there is a p_T dependency. Both the near side and away side Gaussian's σ decrease with increasing momentum. Also, the pion p_T distributions are shown in Fig. 6.8. The near, away and incluside(all azimuth integrated jet + background signal) distributions are plotted in red, blue and black respectively.

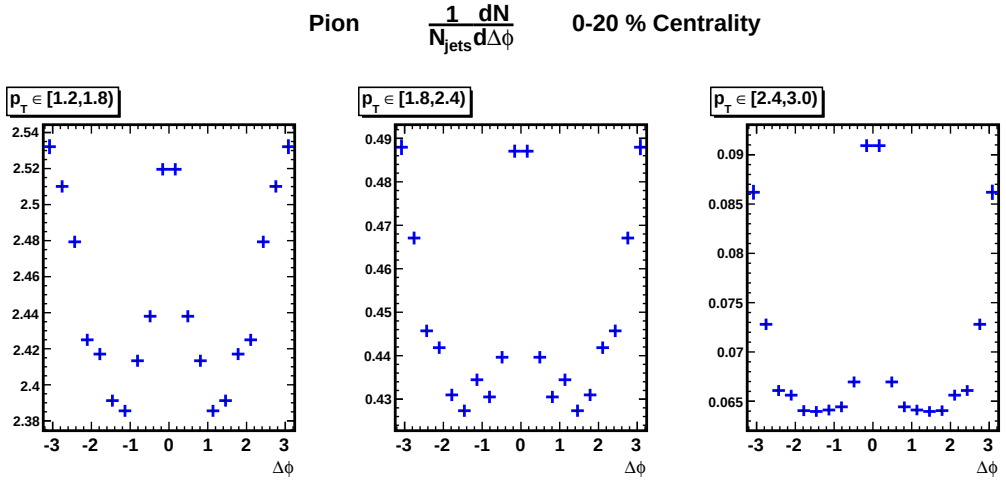

Figure 6.5: Per trigger jet $\Delta\phi$ distributions of pions for three p_T bins. Note the zero suppressed y axis

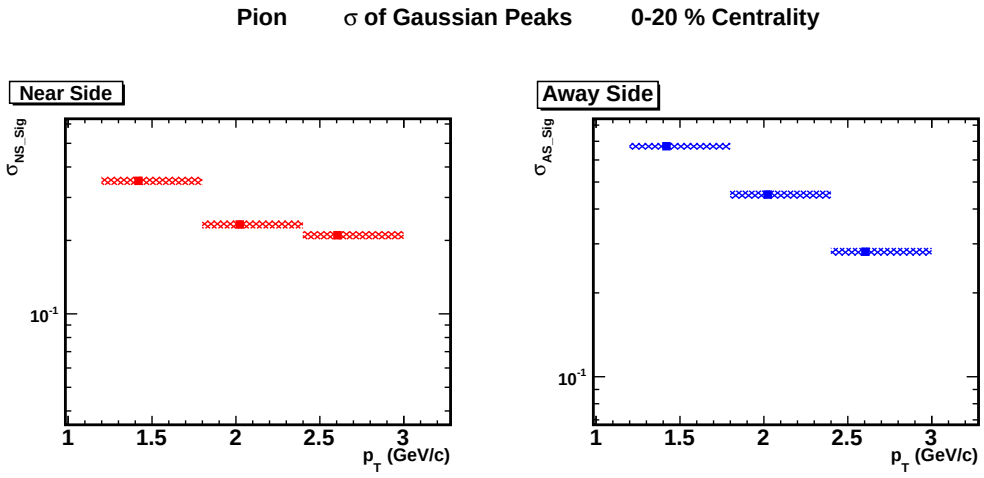

Figure 6.6: Pions Gaussian's σ for the near(shown in red) and away side(blue) jet directions for three different p_T bins. The errors are the statistical errors provided by the fit.

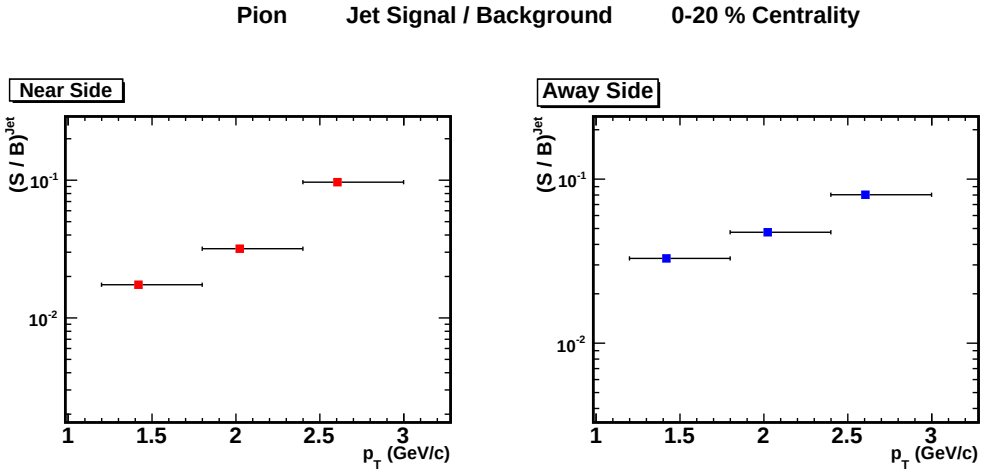

Figure 6.7: Pions's jet signal over background for the near(shown in red) and away side(blue) jet directions for three different p_T bins.

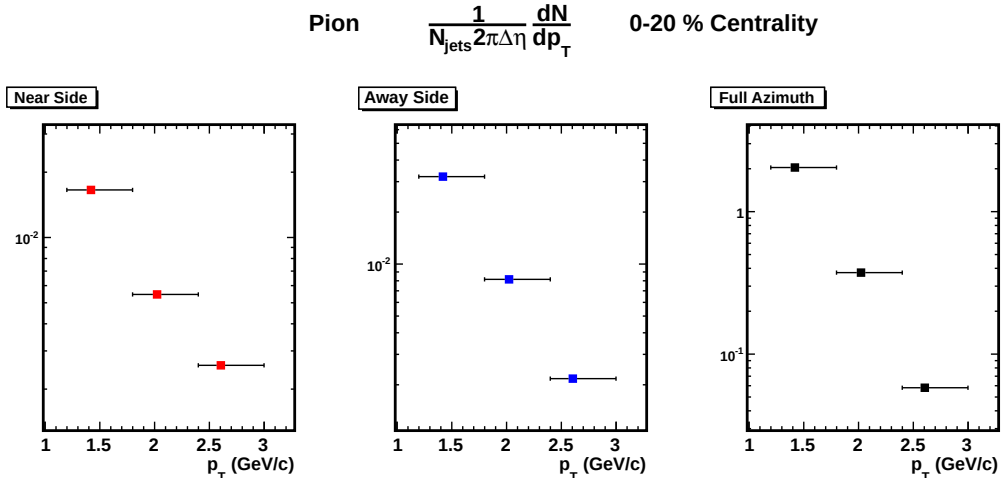

Figure 6.8: Pions p_T distribution in all azimuth(black), the near side jet(red) and the away or recoiling side(blue).

6.2 Peripheral events (20 - 80%)

The proton and pion results using the mid central to peripheral biased events are included in this section.

6.2.1 Protons

The final per trigger jet proton $\Delta\phi$ distributions as function of p_T bins in 20-80% centrality events are shown in Fig. 6.9. The near side and away side jet Gaussians's σ are shown in Fig. 6.10. It can be noticed that the protons's near side Gaussian σ are similar (within errors) in the central and peripheral events(see 6.1.1). On the other hand, the σ of the protons' away side Gaussians are higher in the central events compared to the peripheral. This indicates a mild enhancement of the broadening in the proton component of the jet yields on the away side in central events compared to peripheral ones. The jet signal/background ratios for protons and in peripheral events are shown in Fig. 6.11 and the proton p_T distributions in Fig. 6.12.

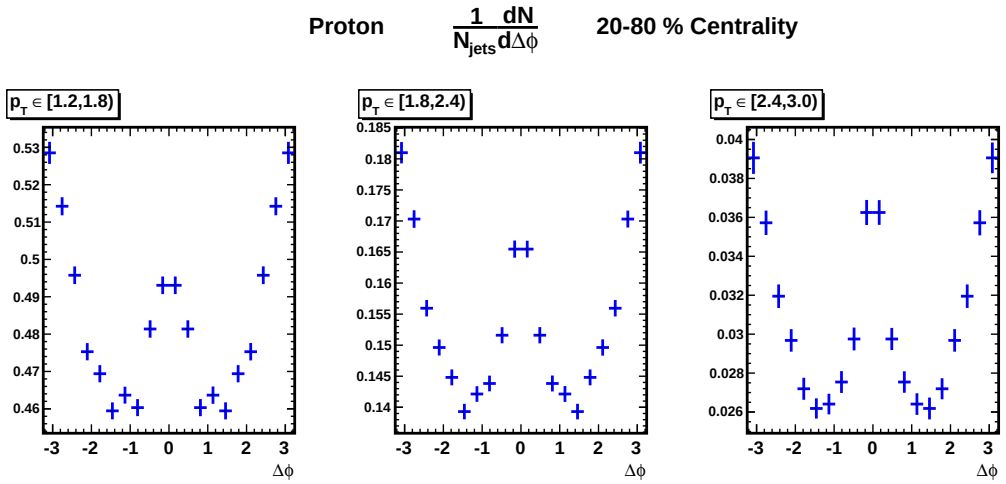

Figure 6.9: Per trigger jet $\Delta\phi$ distributions of protons for three p_T bins. Note the zero suppressed y axis

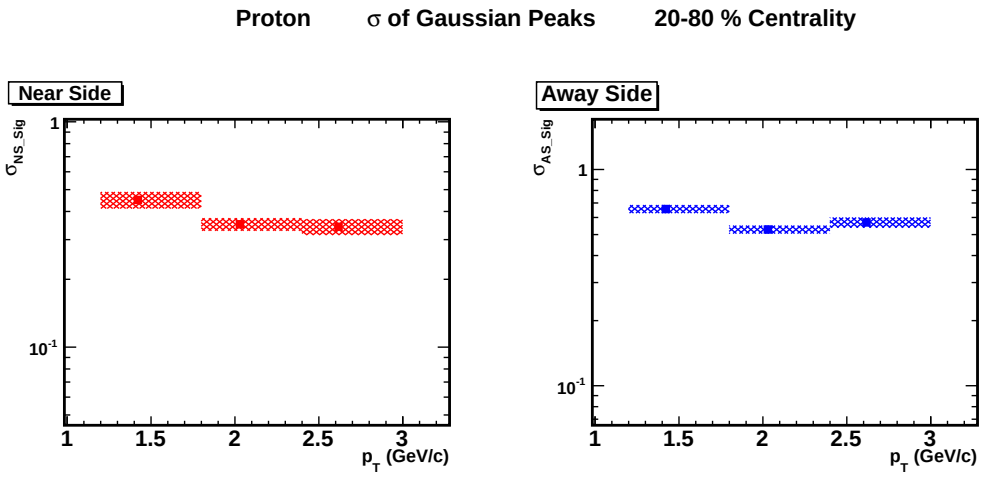

Figure 6.10: Protons Gaussian's σ for the near(shown in red) and away side(blue) jet directions for three different p_T bins. The errors are the statistical errors provided by the fit.

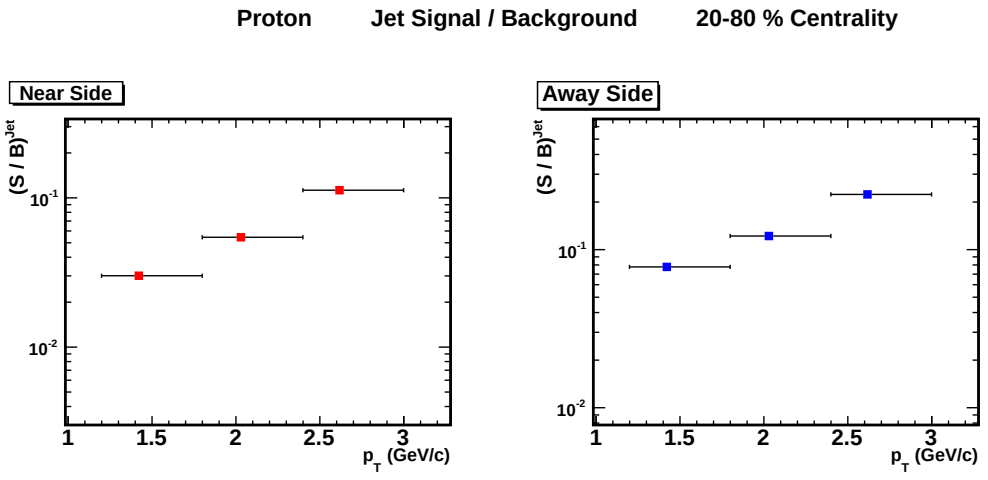

Figure 6.11: Protons's jet signal over background for the near side (shown in red) and the away side(blue) jet directions for three different p_T bins.

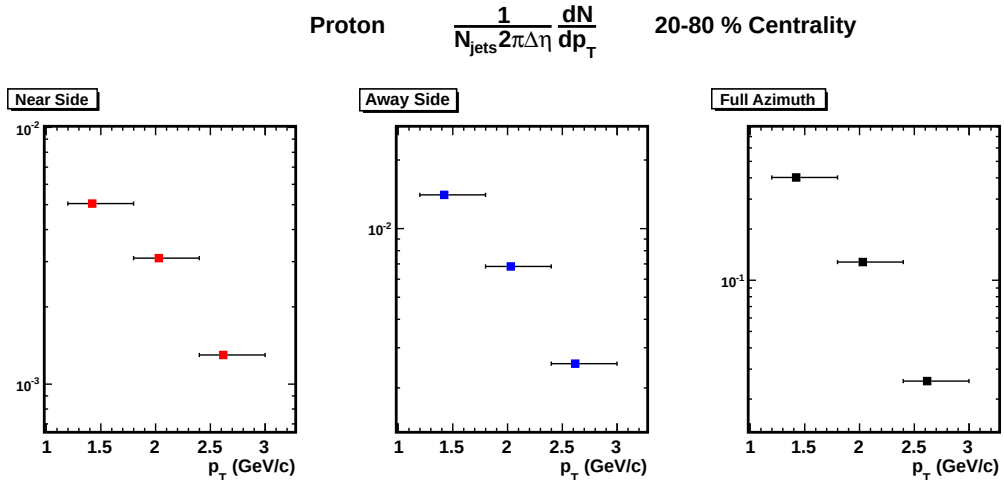

Figure 6.12: Protons' p_T distribution in all azimuth(black), the near side jet(red) and the away or recoiling side(blue).

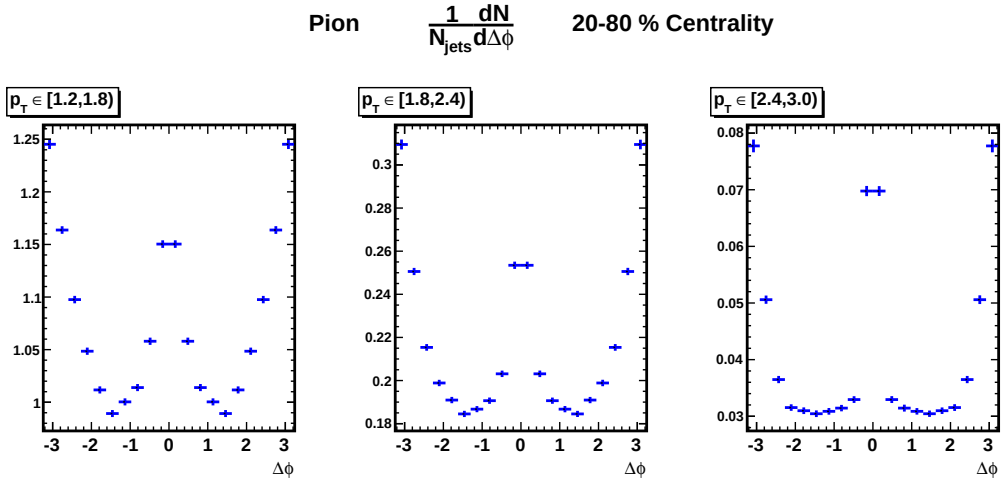

Figure 6.13: Per trigger jet $\Delta\phi$ distributions of pions for three p_T bins. Note the zero suppressed y axis

6.2.2 Pions

The pions results of peripheral events are shown in this section. Pion's $\Delta\phi$ distributions are shown in Fig. 6.13. The near and away side jet's Gaussians σ are shown in Fig. 6.14. The pions Gaussian's σ in the near side are similar for both peripheral and central events except for the highest p_T bin ($>$ 2.4 GeV/c) where the central Gaussian is wider. The away side Gaussian σ are higher in central events compared to peripheral ones except for the last p_T bin where they are similar. Again, this signals a different recoiling jet - medium interaction in central and peripheral events. The jet signal/background ratios for pions and in peripheral events are shown in Fig. 6.15. The pion p_T distributions can be seen on Fig. 6.16.

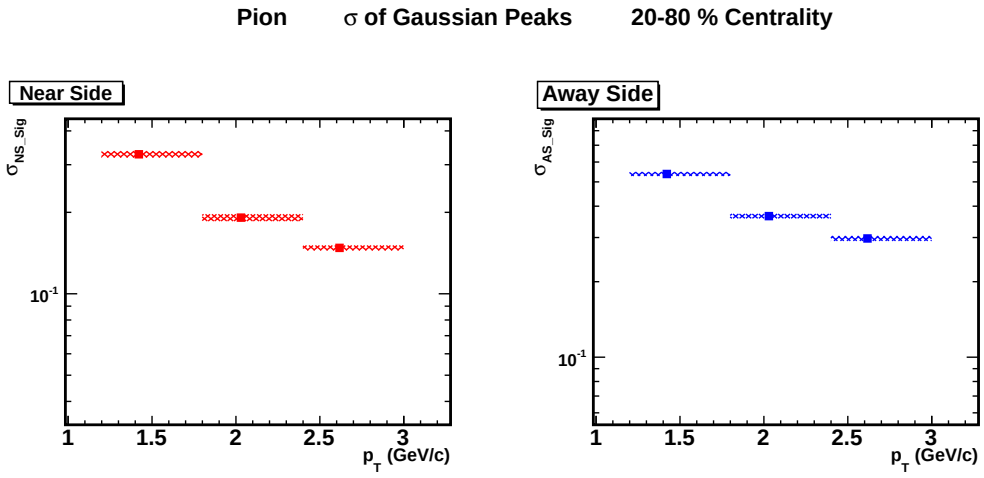

Figure 6.14: pions's Gaussian σ for the near(shown in red) and away side(blue) jet directions for three different p_T bins. The errors are the statistical errors provided by the fit.

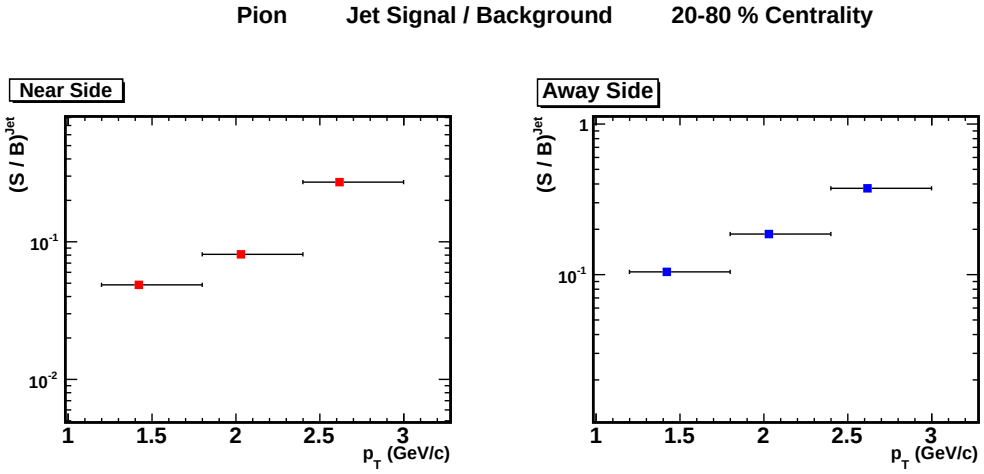

Figure 6.15: pions's jet signal over background for the near side (shown in red) and the away side(blue) jet directions for three different p_T bins.

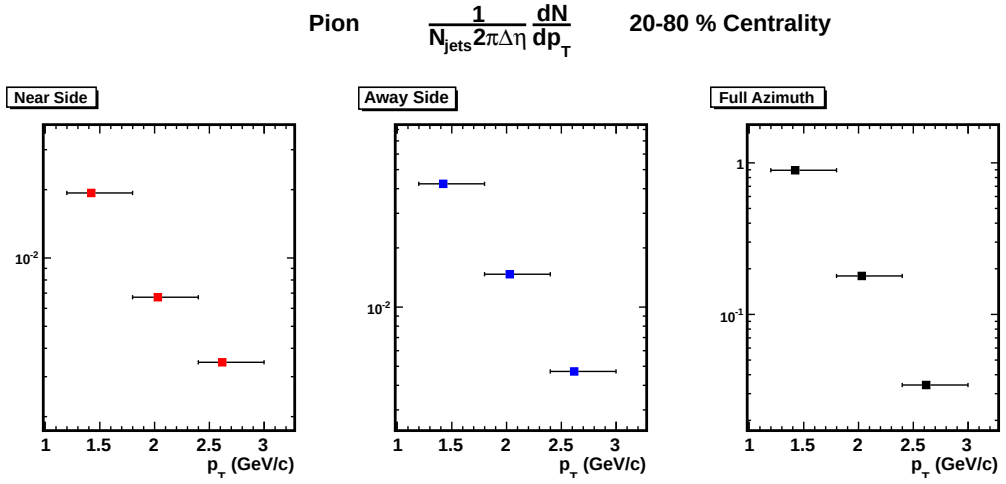

Figure 6.16: pions' p_T distribution in all azimuth(black), the near side jet(red) and the away or recoiling side(blue).

6.3 Proton/Pion ratios

The final p/π ratio measurements for the 0-20% and 20-80% most central events are shown on figures 6.17 and 6.19 respectively. The near side ratios are consistent in both centralities, indicating that the trigger jet population used in this analysis is similarly biased in both cases. The ratios are lower than the inclusive (shown in black) measurement and closer to the p/π seen in vacuum fragmentation (i.e. in p + p collisions). The away side's p/π is larger than the near side and it is smaller than the inclusive ratio (except for the highest p_T bin). A plot including both centralities is shown in Fig. 6.21. It can be seen that the away side ratio is enchanced compared to the near side ratio but smaller than the inclusive ratio. The away side enhancement is bigger in the central events. These two observations imply that the p/π anomalous enhancement is at least partially due to a medium induced modification of the recoiling jet fragmentation.

Other STAR measurements including p/π ratios in minimum bias d+Au and 0-12 % most central Au + Au collisions ar $\sqrt{s_{NN}} = 200$ GeV are shown in figures 6.18 and 6.20 for comparison [23]. These measurements do not allow a direct comparison and are shown to put the results obtained in perspective. The main difference comes from the centrality distributions of the events used in this dissertation. Even though the centrality cuts are set at 0-20% and 20-80%, the jet trigger condition biasses the distributions to be negatively skewed. As an example, the normalized distributions of minimum bias Au+Au collision events can be 70% higher than the normalized distributions of the jet

triggered events for centralities bigger than 20%.

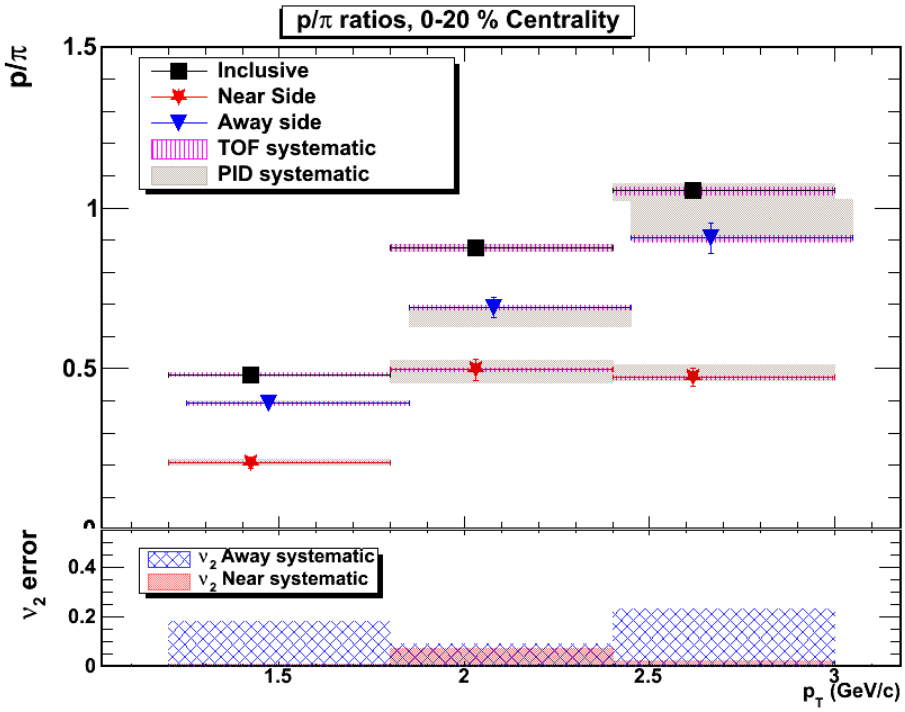

Figure 6.17: Inclusive, near, and away side p/π ratios as function of p_T. The systematic error due to the quadrupole component of the $\Delta\phi$ distributions model is shown in the bottom panel

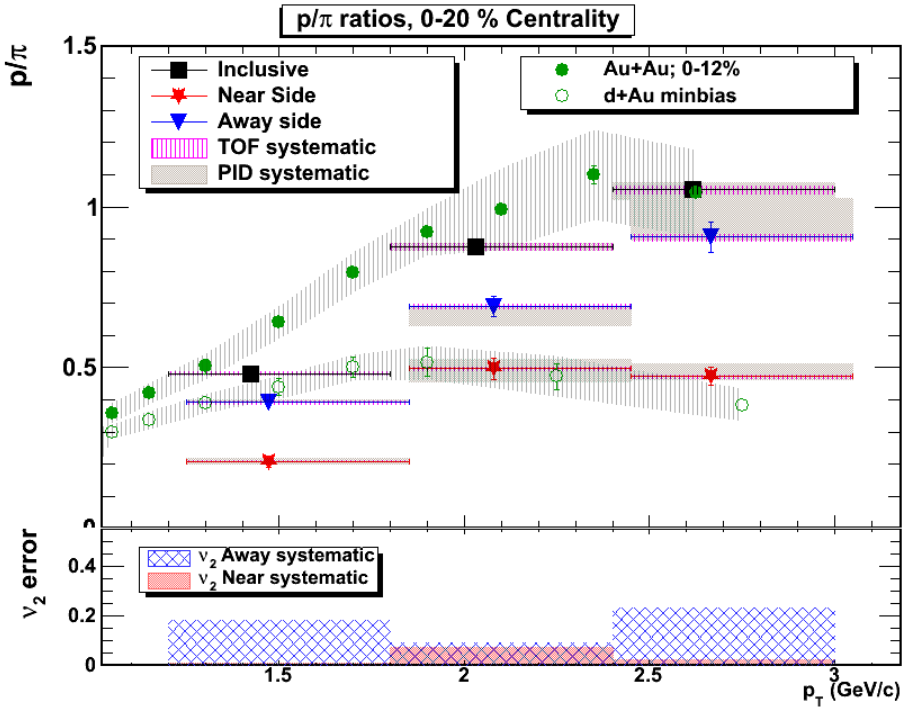

Figure 6.18: Inclusive, near, and away side p/π ratios as function of p_T. The systematic error due to the quadrupole component of the $\Delta\phi$ distributions model is shown in the bottom panel. The green solid circles correspond to 0-20% most central Au+Au inclusive ratios and the green hollow circles to minimum bias d+Au collisions

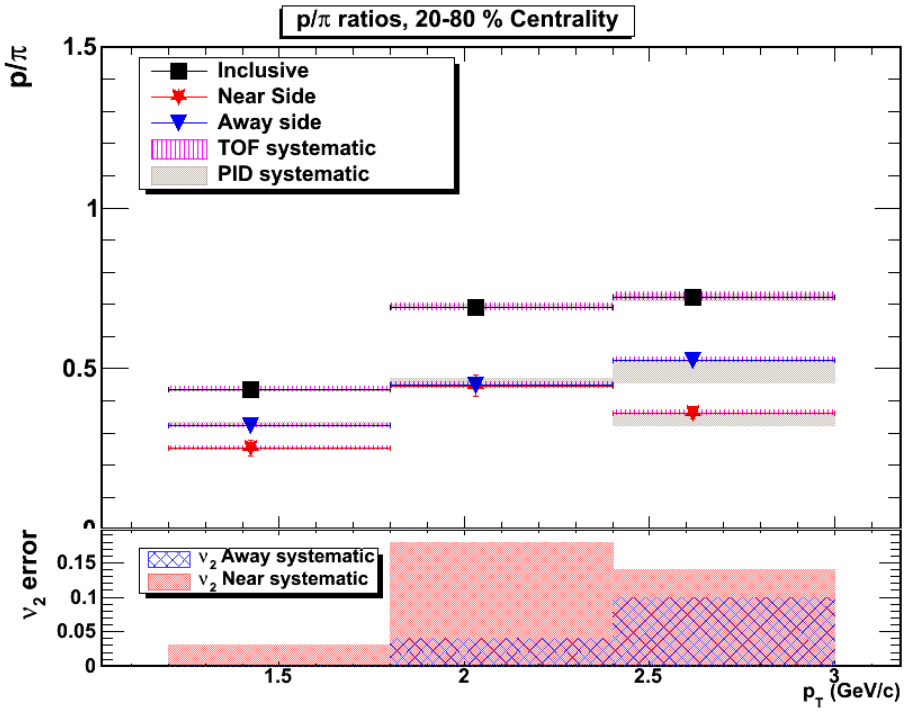

Figure 6.19: Inclusive, near, and away side p/π ratios as function of p_T. The systematic error due to the quadrupole component of the $\Delta\phi$ distributions model is shown in the bottom panel

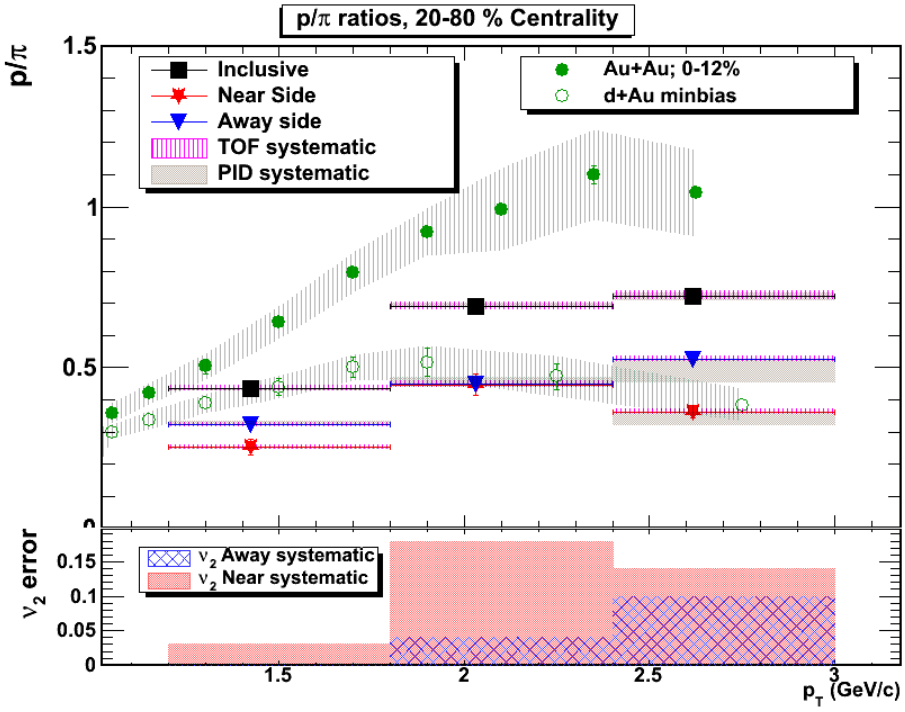

Figure 6.20: Inclusive, near, and away side p/π ratios as function of p_T. The systematic error due to the quadrupole component of the $\Delta\phi$ distributions model is shown in the bottom panel. The green solid circles correspond to 0-20% most central Au+Au inclusive ratios and the green hollow circles to minimum bias d+Au collisions

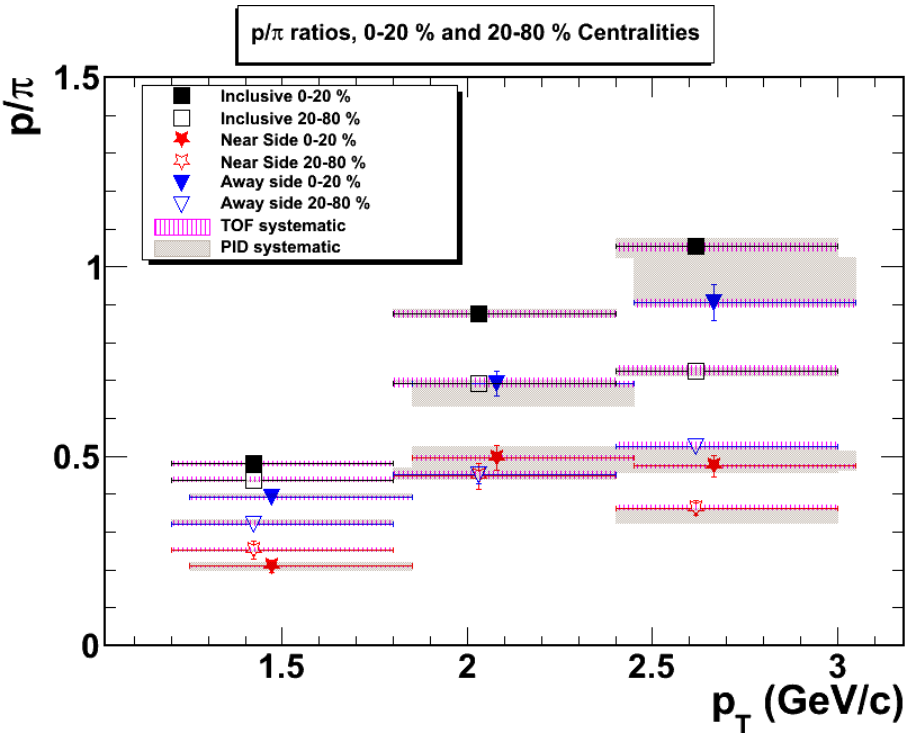

Figure 6.21: Inclusive, near, and away side p/π ratios as function of p_T for 0-20% and 20-80% centrality events.

Chapter 7

Conclusions and Future Work

7.1 Conclusion

Particle production in p + p collisions is calculated by a convolution of the parton distributions functions, hard scattering cross sections and fragmentation functions. The parton distribution functions give the probability of having a quark (gluon) of a given momentum inside the colliding proton. The fragmentation functions give the probability that a hard scattered parton creates a given hadron of a certain momentum and are usually measured in $e^+ + e^-$ or DIS collisions. The fragmentation or hadronization mechanism by which partons (quarks and gluons) coming out of a hard scattering form hadrons is not understood from first principles. The low energy momentum exchanges involved in hadronization cannot be calculated via perturbation theory in QCD. Therefore, fragmentation is treated phenomenologically and there are several models with free parameters that are obtained from fits to high energy collisions data.

The string fragmentation model describes hadron production via the breaking of a color flux tube that is generated when to partons coming out of a hard scattering move apart. The color flux tube is a consequence of

the gluon-gluon interaction that tends to merge flux lines and the asymptotic behavior of the strong interaction. The strong force tends to increase with distance. When the energy accumulated in the flux is high enough, the tube breaks generating a quark and anti-quark pair. These new color singlets might be moving apart form each other and if they have enough energy they might break too. This process is repeated with the newly created partons and a shower of quark and anti-quark pairs develops. Mesons (quark and anti-quark bound pair) are formed when the pairs get on-mass-shell ($E^2 - |\vec{p}^2| = m^2$). Baryon (bound state of three quarks) production in the string model can be explained by letting the flux or string break into diquark and anti-diquark pairs. A diquark is a hypothetical state of two quarks inside a baryon. Each diquark - quark connected string can produce a baryon [65].

The cluster fragmentation model explains hadron production via cluster formation. The hard scattered parton splits as the parton showers (via gluon emission) and the gluons at the end of the shower are split into quark and anti-quark pairs. These pairs form clusters that are considered excited hadron resonance states which can decay into the final hadrons. Heavy clusters might decay into lighter clusters before the final hadron formation. Cluster decay proceeds by creating quark and anti-quark pairs out of the vacuum and dividing the cluster into two lighter ones. Finally, each cluster decays into a pair of hadrons. A pair of mesons (baryons) is generated from a cluster decaying by popping a (di)quark and anti-(di)quark pair out of the vacuum [66].

The situation is much more complicated in a heavy ion collision environ-

ment. Many binary collisions can be present and, furthermore, a thermalized medium (QGP) could develop before hadronization. Hadron yield ratios can be well described using a thermal model. Hydrodynamic models exist that can reproduce RHIC's particles yields below $p_T = 2$ GeV as long as thermalization occurs before ~ 1 fm/c. Under the hydrodynamical picture, the partons are supposed to thermalize and then hadronize at a given chemical freeze out temperature. The resulting hadrons could potentially interact among themselves via inelastic collisions. The measured hadrons acquire their final state when they cease to interact at a given kinetic freeze out temperature. Jet quenching is supposed to occur before the chemical freeze out when a parton coming out of a hard scattering interacts with the gluons and quarks present in the heavy ion collisions. If the parton loses energy via gluon bremsstrahlung or collisions then the final jet energy is modified and that can have an impact on the jet fragmentation. Another possible cause of change in jet's hadronic composition is the hadron-hadron interaction before kinetic freeze out. The broadening of Jet-charged particles $\Delta\phi$ correlations in Au+Au compared to p+p seems to favor the parton-medium interaction over hadron-hadron interactions as source of fragmentation modification.

Hadron suppression (as measured by the reduced nuclear modification factor) and trigger-associated $\Delta\phi$ distributions' dilution at $\sim \pi$ are thought to be consequences of partonic energy loss in a QGP medium. If that is the case, it is plausible to look for the energy loss effect on final jet hadronic composition. A vacuum fragmenting jet base is necessary. In the present dissertation the

base triggers are jets in peripheral Au + Au collisions. These jets have a higher probability of fragmenting in vacuum (there is a non zero chance that the jets do not fragment in vacuum due to the wide range in centralities chosen; clean samples of vacuum fragmenting jets can only be obtained in e^++e^- collisions). Surface biased jets are selected in Au + Au central collisions and the bias is confirmed by comparing the particle ratios and $p_T^{reco,jet}$ distributions for central and peripheral trigger jets. The recoiling jet $\Delta\phi$ signal showed a broadening in the central events of different magnitude in protons and pions. This suggests that there is a medium-jet interaction (expected from previous STAR results mentioned earlier) and that the interaction does not affect both particles the same way.

The evolution with centrality of the p/π^+ and $\bar{p}/\pi^-$ ratios in $\sqrt{s_{NN}}$ = 200 GeV Au + Au collisions can be observed in Fig. 7.1. The data from an in vacuum fragmenting jet from e^++e^- collisions is also plotted for comparison. A similar evolution is seen in the recoiling jet side ratios at p_T >2.4 GeV/c. The p/π increased going from 20-80% to 0-20% centralities. On the other hand the ratios remained the same in the near (or trigger) sides for both centralities. Both trends can be observed in Fig. 6.21.

Measurements done at STAR [23] demonstrated that at $p_T > 5$ GeV the p/π ratio is the same for peripheral and central Au+Au and d+Au collisions at the same energy. This indicates that pQCD like fragmentation is the main hadron production mechanism at that region. Furthermore, the energy lost for quark and gluon jets has to be the same. At mid transverse momentum the

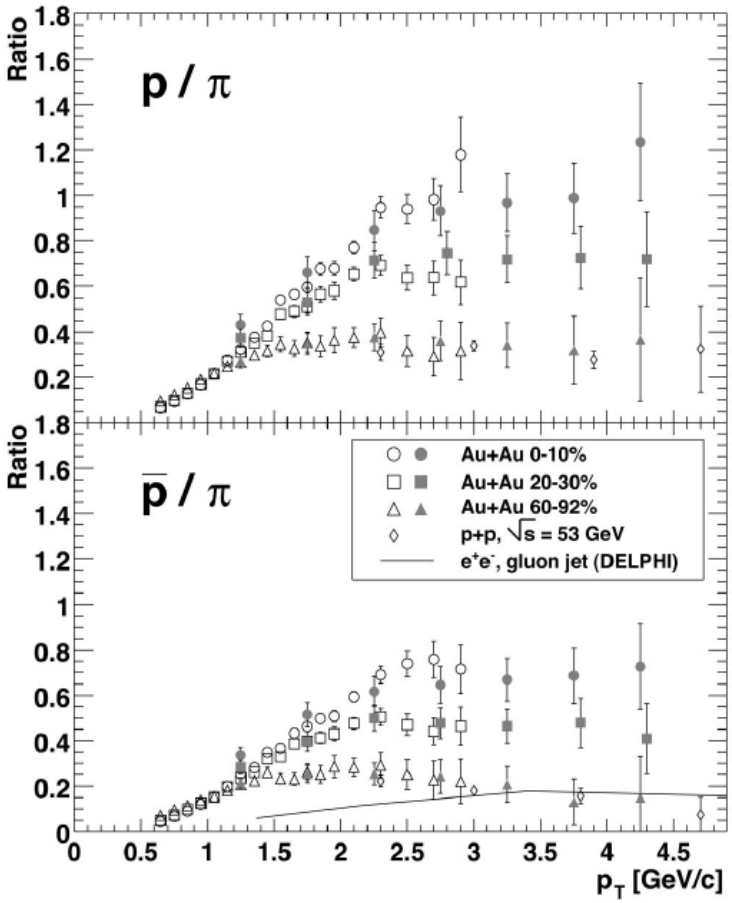

Figure 7.1: Proton over pion ratios at different centralities. The open(filled) markers correspond to charged(neutral) pions. The solid line corresponds to gluon jets [22]

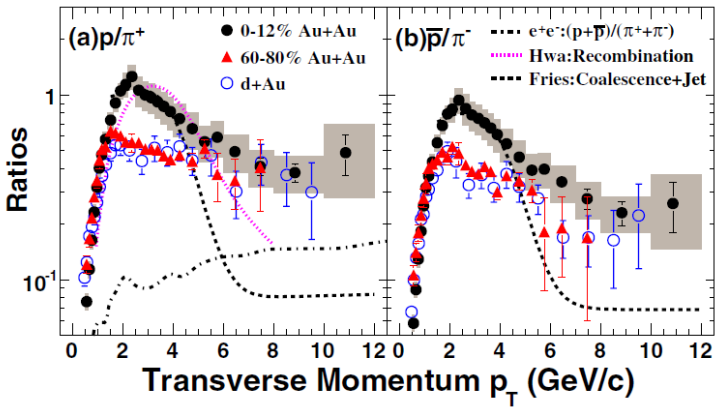

Figure 7.2: p/π ratios in peripheral and central Au + Au collisions and d + Au collisions at $\sqrt{s_{NN}} = 200$ GeV. Two theoretical models reproduce the data in at mid p_T. The e^+e^- data is for $\sqrt{s} = 91.2$ GeV [23]

Cronin effect enhances hadronic production in p + ion collisions and is thought to be caused by partonic scattering inside the ion nucleus. This scattering is previous to the hard scattering and it increases the transverse momentum of the scattered parton. The Cronin effect is not equal for pions and protons [67]. The fact that p/π enhancement is not observed in d+Au collisions provides evidence that the phenomenon is not just an initial partonic scattering effect. One can then consider other possibilities like modified fragmentation function and recombination models. The p/π^+ and $\bar{p}/\pi^-$ ratios extended to $p_T = 12$ GeV can be observed on Fig. 7.2.

The present analysis attempts to shed light into the origin of protons' and pions' similar yield at mid p_T ($\sim$ 2 - 4 GeV/c) in heavy ion collisions. This similarity is not expected from jet fragmentation alone. One way to make sense of these discrepancies is through the coalescence model [28]. In

a coalescence model, QGP partons follow an exponential momentum spectra while minijet fragmenting partons have a power law spectra. The partons coming from either the QGP or minijets are allowed to coalesce among each other without restrictions [24]. Coalescence models qualitatively predict the correct behavior of p/π enhancement at two different energies. The p/π^+ ratio is higher at lower energy while the $\bar{p}/\pi^-$ ratio is lower at lower energy. Fig. 7.3 shows the measured ratios along with the coalescence predictions for 62 and 200 GeV. The baryon junction+jet model seems disfavored [29]. The fact that neither the central or peripheral away(recoil) side p/π ratios reach the inclusive ones (black markers in Fig 6.17 and 6.19) can bee seen as evidence that some of the ratio enhancement does require recombination of partons present in the thermal QGP. A definite statement can't be made since there exists the possibility that the extra enhancement is produced by modification of fragmentation of minijets too. Further investigations going up and down in trigger p_T would be required to characterize the complete scenario.

Despite the success of coalescence/recombination models, they are not the only feasible explanation of the anomalous baryon/meson enhancement. Another suggested explanation of the p/π enhancement is the effect of parton energy loss on the hard component of particle spectrum of Au+Au collisions. The measured spectra are described by a soft (scaling with number of participant pairs) + a hard (scaling with number of binary collisions) components. The hard part is isolated and its modification with respect to number of binary collisions scaling is related to a negative boost in the hard component

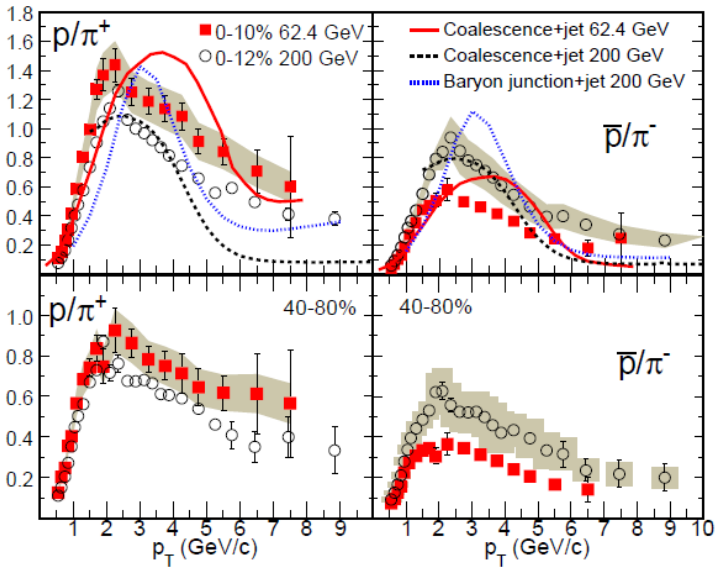

Figure 7.3: Coalescence and baryon junction model comparisons. The coalescence model for 200 GeV was adjusted to reproduce the data, the model line for 62 GeV is a prediction [29]

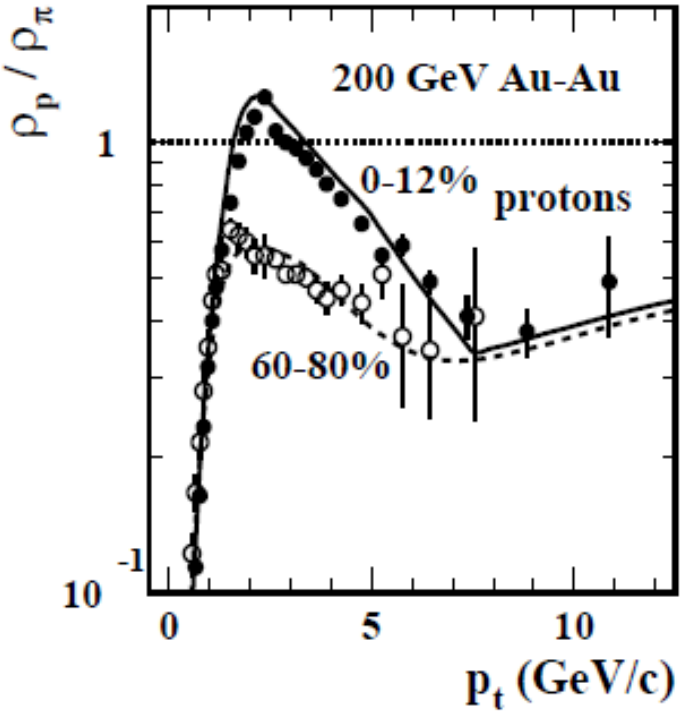

Figure 7.4: Data - model comparison for central and peripheral p/π ratios for the hard component of the particle spectrum in $\sqrt{s_{NN}}$ = 200 GeV Au+Au events [68]

hadrons p_T. The modification of the hard component shows up as an increase of protons in the p_T region of p/π enhancement. Fig. 7.4 shows the hard component proton over pion ratios in peripheral and central events obtained with this method [68].

The hypothesis that the p/π enhancement originates due to a medium induced modification of the parton fragmentation was tested. This dissertation presented p/π ratios in the p_T range 1.2 - 3.0 GeV/c for particles correlated

in azimuth with a jet trigger of p_T^{jet} = 8 - 20 GeV/c. These measurements were divided in two centrality bins, namely 0-20% and 20-80% most central events. The near (away) side ratio was obtained by fitting the relative azimuth distributions for protons and pions with respect to the trigger jets with a Gaussian peaked at $\Delta\phi \sim 0$ (π). The near side p/π ratios are similar in the central and peripheral events for all p_T suggesting similarly biased, vacuum fragmenting jets. In contrast, the away side p/π ratios are larger than the near side ones with the difference increasing as a function of p_T and centrality. This suggests that the anomalous p/π ratio can be at least partially attributed to a modified fragmentation function of the partons (jets) traversing the Au + Au collision environment.

It is important to point out that the recoiling jets are biased to maximize their path in the medium. This is desired in order to optimize the chances of observing any parton-medium fragmentation modification. In the other hand, this maximal bias might be the reason why the away side p/π signal could not match the inclusive signal. Think of the scenario where lower momentum jets suffer from a higher modification in the medium. Also, since $R_{CP} \sim 1$ at $p_T \sim$ 2-3 GeV/c it is hard to distinguish among the scenarios where protons are more copiously produced in central Au+Au collisions and the case where protons are less suppressed than pions.

In summary, the fact that the enhancement in the recoiling jet side increases with centrality seems to confirm the modified fragmentation function hypothesis. Nevertheless, since the inclusive (jet + background) ratios are

higher than the recoiling jet side ratios some recombination/coalescence might still be necessary to account for the total p/π enhancement. Yet, another possibility is that the minimum bias jets present in the events, that are not triggered on in the present analysis do suffer some modification in the Au+Au collision environment and that it accounts for the remaining enhancement too.

7.2 Future Work

The work presented in this dissertation can be extended to lower and higher proton and pion p_T by making use of the 2011 Au + Au data produced at RHIC which represents an increase of a factor of one and a half in statistics. This increase in statistics would make it possible to efficiently measure and fit $\Delta\phi$ distributions at lower and higher p_T. This, in turn, will permit to confirm that the trigger jets in central and peripheral collisions have the same fragmentation down to lower momentum.

The increase in statistics can also allow for a finer binning in centrality. Comparing the p/π ratios as a function of centrality would allow to reach a definite conclusion about the onset of the enhancement in these ratios. Figuring out whether this onset happens at the same centrality in inclusive measurements and jet - trigger biased events could help to quantify the extent to which medium modification of jets contributes to the anomalous p/π enhancement and mid p_T.

Finally, a similar measurement for p+p jet triggered events would provide a cleaner (than peripheral events) in vacuum fragmentation baseline of

the p/π measurement that can be compared to central Au + Au collisions.

Appendix

Appendix 1

Appendix $\Delta\phi$ Fits

This appendix includes the fits to the $1/N_{jets}dN/d(\Delta\phi)$ distributions of protons and pions. Each centrality and p_T bin is shown separately. The fits for the two models (with and without quadrupole component) are included in this appendix. The plots are divided in four pads. The upper left pad contains the $1/N_{jets}dN/d(\Delta\phi)$ data along with the fit (in red) and the 95% confidence band form the fit (yellow band). The upper right pad is showing the residuals (data - fit) as function of $\Delta\phi$. The lower left pad shows the fit parameters with errors and the $\chi^2 = ((data - fit)/\sigma_{data})^2$ for each $\Delta\phi$ bin. The parameter names correspondence is as follow: offset is the constant background offset, NS_Amp(AS_Amp) is the near(away) side Gaussian amplitude, NS_Sig(AS_Sig) is the near(away) side Gaussian σ and finally, for the model that includes quadrupole ν_2 (for the case of pions since the protons ν_2 is determined from the pion's) is the coeffient that multiplies the quadrupole term $2 * offset * cos(2\Delta\phi)$.

1.1 Central

This section includes the $1/N_{jets}dN/d(\Delta\phi)$ distributions and its fits results coming from the 0-20% most central events.

1.1.1 Proton

The first set of three plots correspond to the fit model consisting of a flat background and two jet peak Gaussians 4.16. The second set of three plots corresponds to the model that includes a quaduprole modulation of the background 4.17. The title labels for each plot specify the centrality , particle and p_T bin of the fits shown.

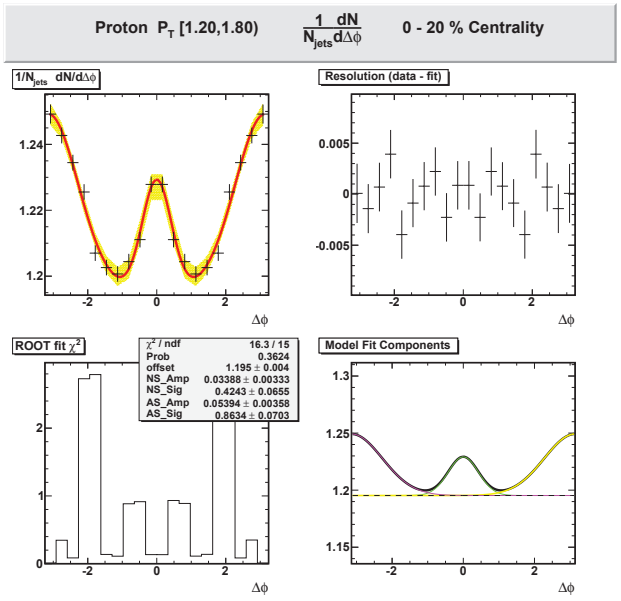

Figure 1.1: Fit results for first model (4.16)

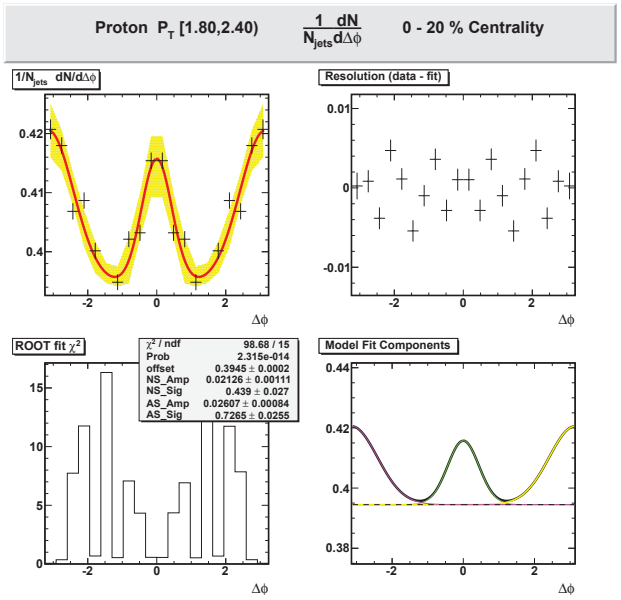

Figure 1.2: Fit results for first model (4.16)

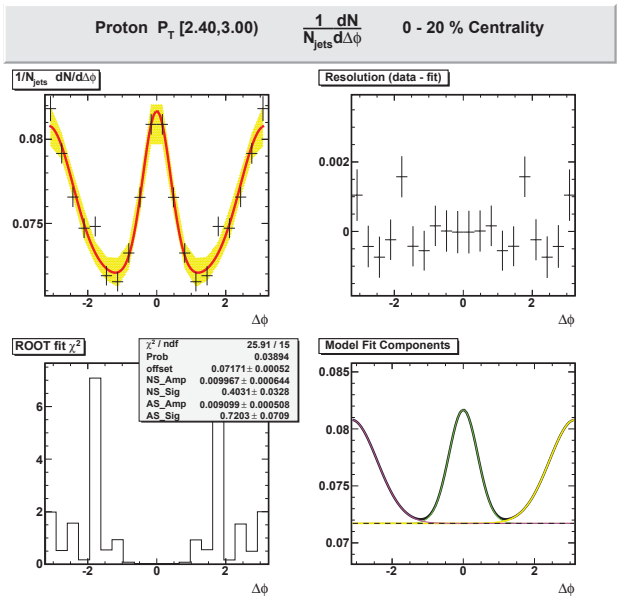

Figure 1.3: Fit results for first model (4.16)

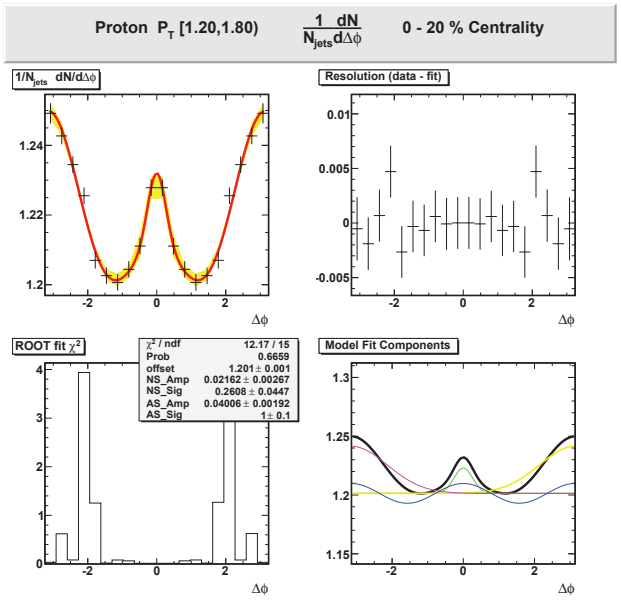

Figure 1.4: Fit results for second model (4.17)

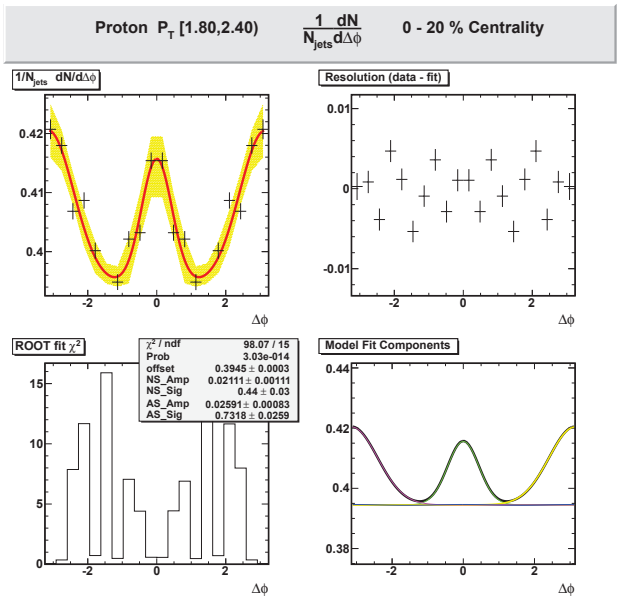

Figure 1.5: Fit results for second model (4.17)

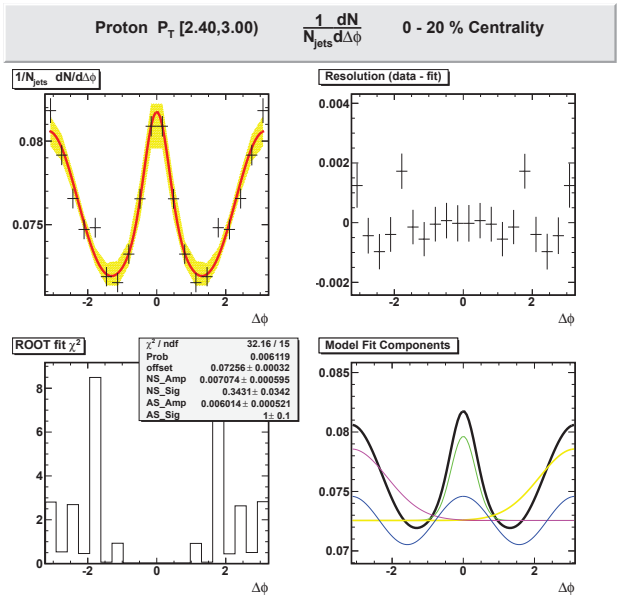

Figure 1.6: Fit results for second model (4.17)

1.1.2 Pion

Following the protons' example, the first set of three plots corresponds to the fit model consisting of a flat background and two jet peak Gaussians 4.16 and the second to the model that includes a quaduprole modulation of the background 4.17.

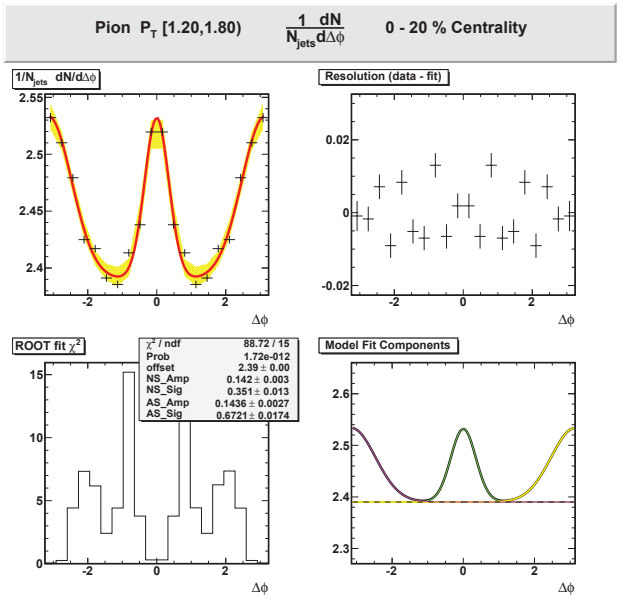

Figure 1.7: Fit results for first model (4.16)

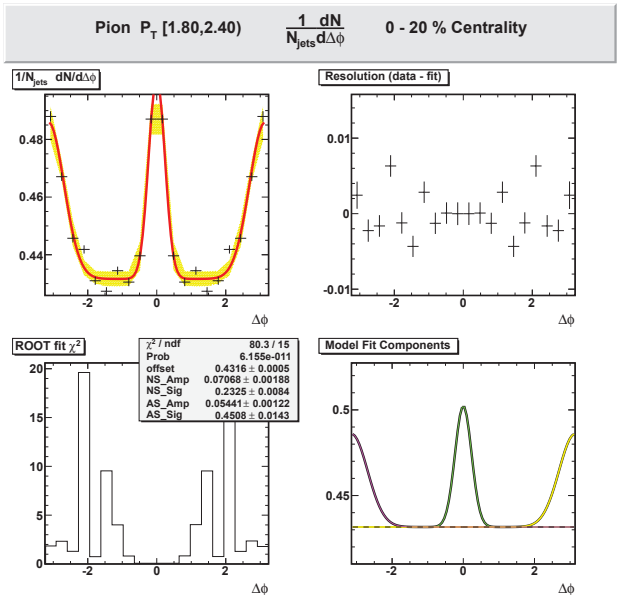

Figure 1.8: Fit results for first model (4.16)

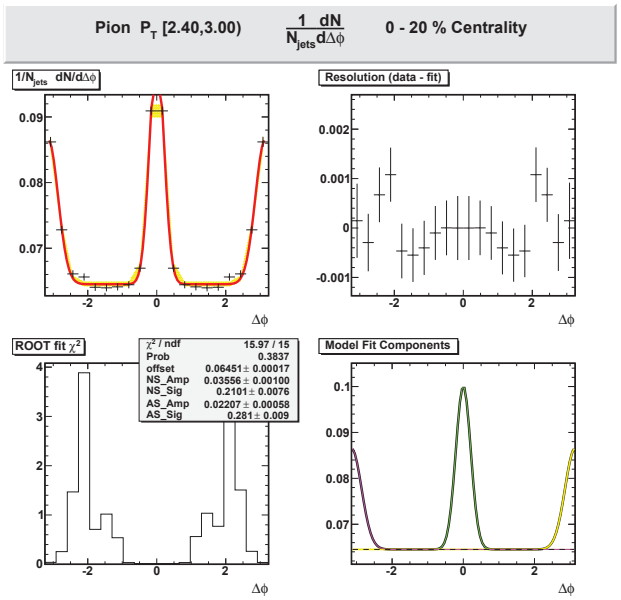

Figure 1.9: Fit results for first model (4.16)

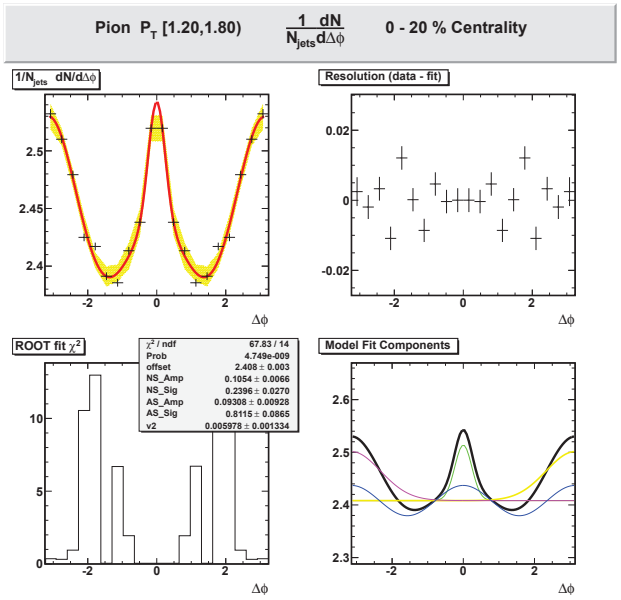

Figure 1.10: Fit results for second model (4.17)

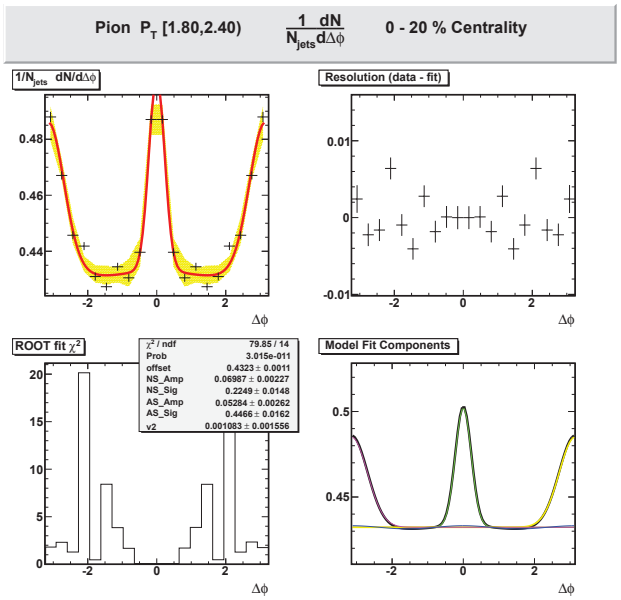

Figure 1.11: Fit results for second model (4.17)

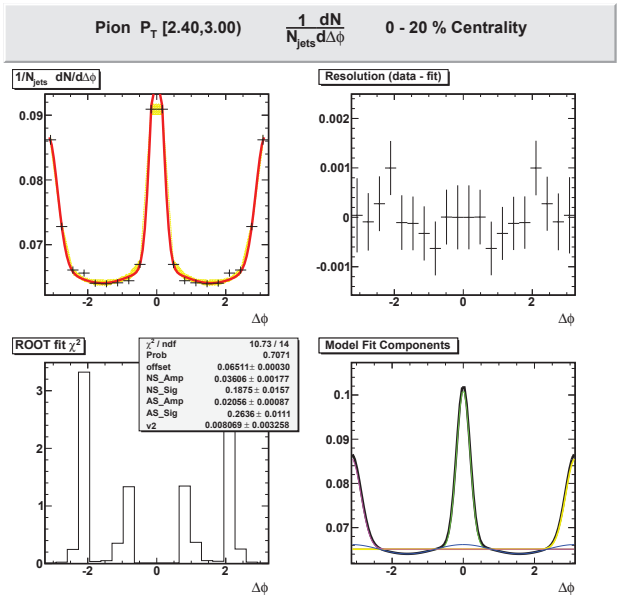

Figure 1.12: Fit results for second model (4.17)

1.2 Peripheral

The $1/N_{jets}dN/d(\Delta\phi)$ distributions and fits obtained in the 20-80% most central events are shown next.

1.2.1 Proton

The following set of plots show the fits to the distributions obtained by using identified protons in the 20-80 % most central, jet triggered events.

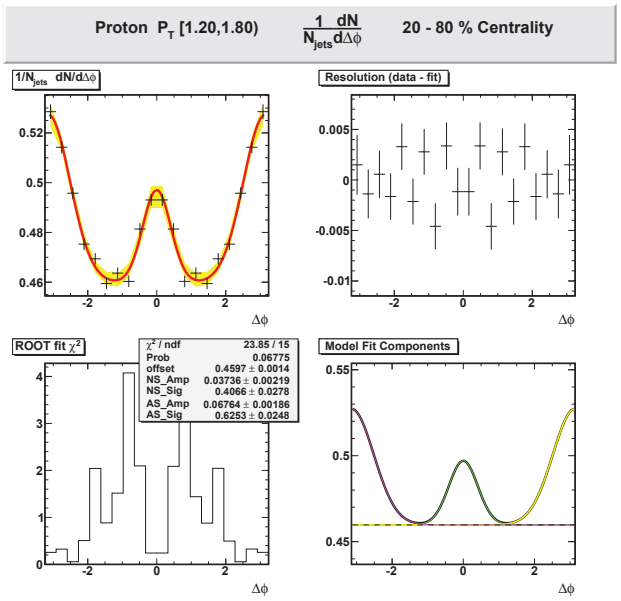

Figure 1.13: Fit results for first model (4.16)

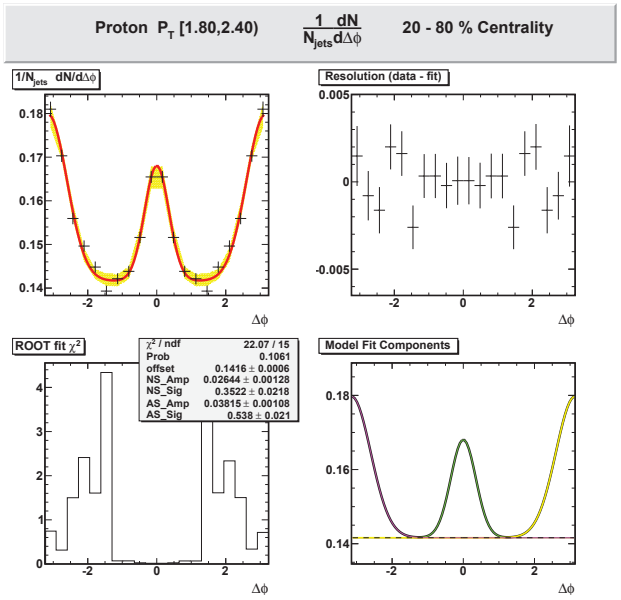

Figure 1.14: Fit results for first model (4.16)

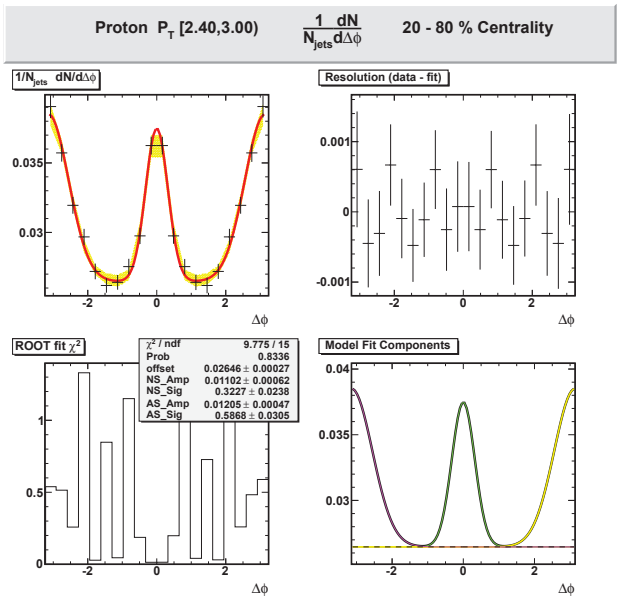

Figure 1.15: Fit results for first model (4.16)

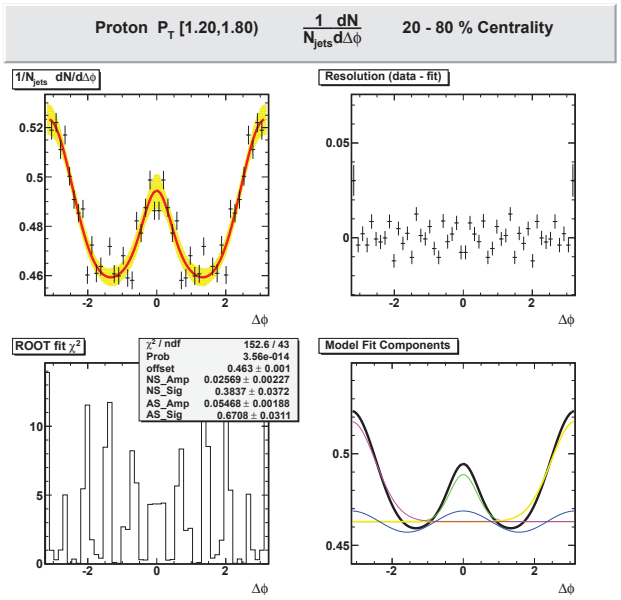

Figure 1.16: Fit results for second model (4.17)

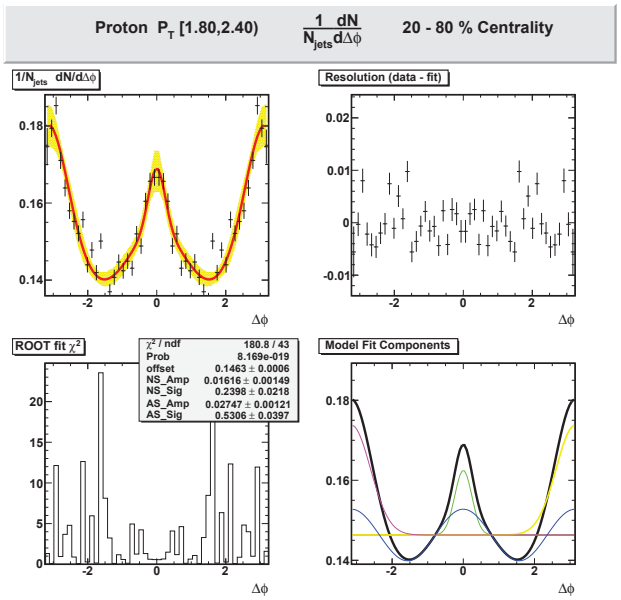

Figure 1.17: Fit results for second model (4.17)

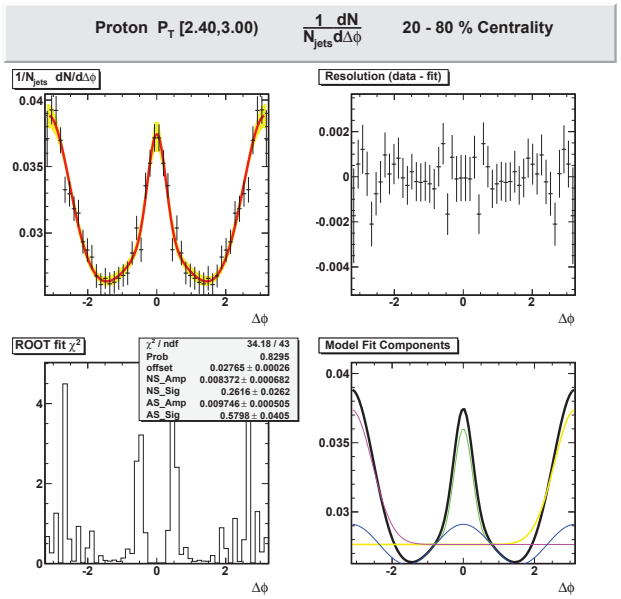

Figure 1.18: Fit results for second model (4.17)

1.2.2 Pion

Finally, the fits in the 20-80 % most central, jet triggered events for identified pions are included.

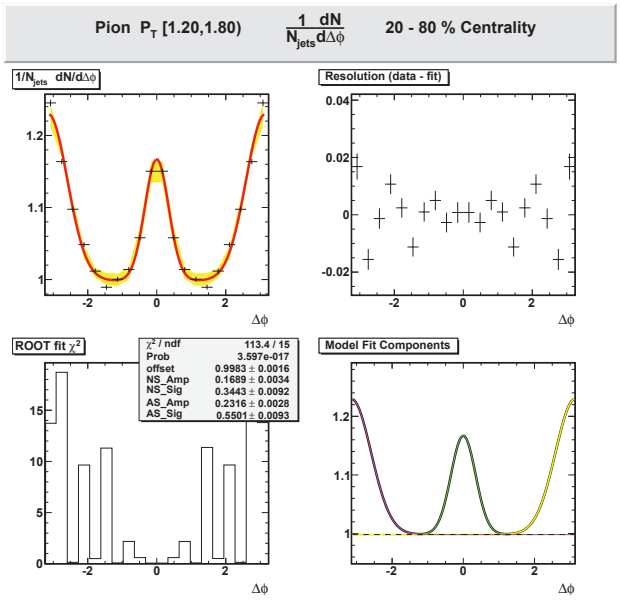

Figure 1.19: Fit results for first model (4.16)

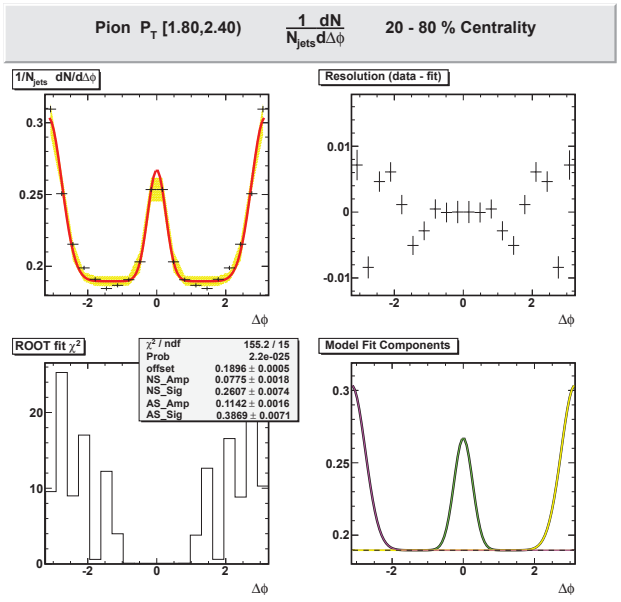

Figure 1.20: Fit results for first model (4.16)

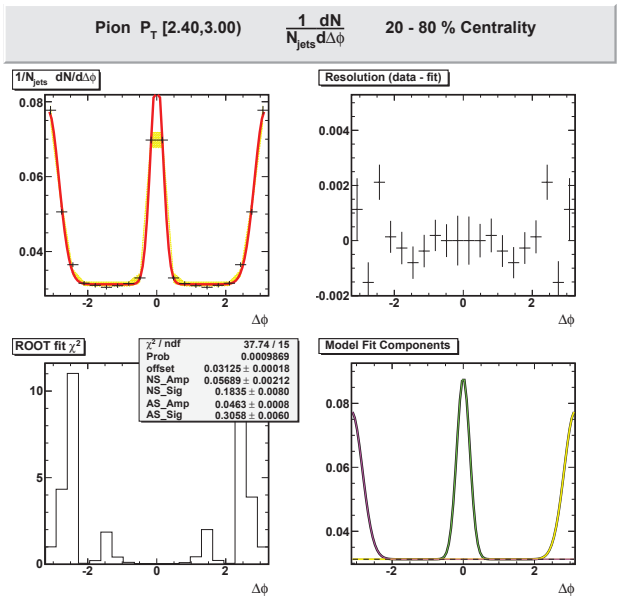

Figure 1.21: Fit results for first model (4.16)

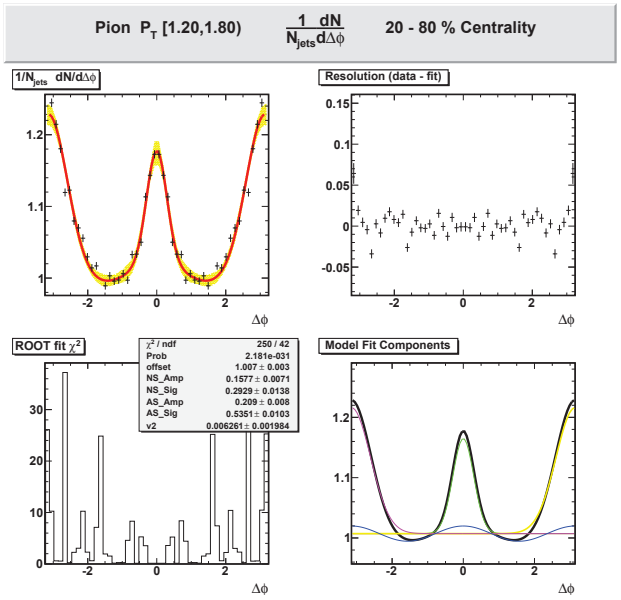

Figure 1.22: Fit results for second model (4.17)

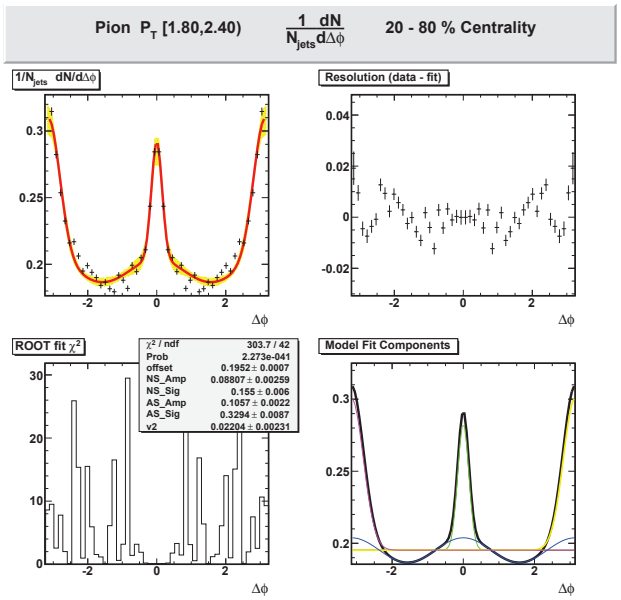

Figure 1.23: Fit results for second model (4.17)

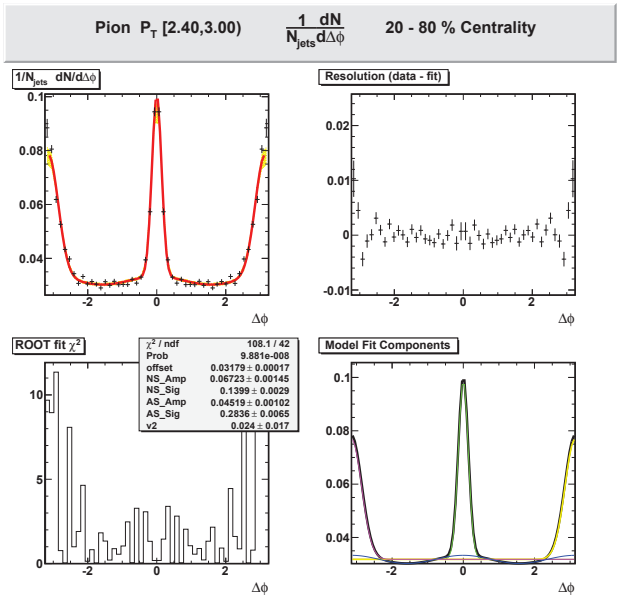

Figure 1.24: Fit results for second model (4.17)

Bibliography

[1] Collins, J. C. and Perry, M. J. *Phys. Rev. Lett.* **34**, 1353–1356 May (1975).

[2] Matsui, T. and Satz, H. *Physics Letters B* **178**(4), 416 – 422 (1986).

[3] Adare, A. and et al. *Phys. Rev. Lett.* **101**, 122301 Sep (2008).

[4] Agakishiev, G. and et al. *Phys. Rev. Lett.* **108**, 072301 Feb (2012).

[5] Tounsi, A., Mischke, A., and Redlich, K. *Nucl.Phys.* **A715**, 565–568 (2003).

[6] Adams, J. and et al. *Nuclear Physics A* **757**, 102 – 183 (2005).

[7] `http://www.bnl.gov/npp/`, (2012). The Case for Continuing RHIC Operations.

[8] Kliemant, M., Sahoo, R., Schuster, T., and Stock, R. *Lect.Notes Phys.* **785**, 23–103 (2010).

[9] Miller, M. L., Reygers, K., Sanders, S. J., and Steinberg, P. *Ann.Rev.Nucl.Part.Sci.* **57**, 205–243 (2007).

[10] Mirkes, E. `http://arxiv.org/abs/hep-ph/9711224`, (1997).

[11] Cacciari, M., Salam, G. P., and Soyez, G. *Eur.Phys.J.* **C72**, 1896 (2012).

[12] Jacobs, P. http://arxiv.org/abs/1012.2406, (2010).

[13] Salur, S. http://arxiv.org/abs/0910.2081, (2009).

[14] de Barros, G., Fenton-Olsen, B., Jacobs, P., and Ploskon, M. http://arxiv.org/abs/1208.1518, (2012).

[15] Cacciari, M., Salam, G. P., and Soyez, G. *JHEP* **0804**, 005 (2008).

[16] Adamczyk, L. et al. http://arxiv.org/abs/1302.6184, (2013).

[17] Sapeta, S. and Wiedemann, U. A. *Eur.Phys.J.* **C55**, 293–302 (2008).

[18] Borghini, N. and Wiedemann, U. A. http://arXiv:hep-ph/0506218, (2005).

[19] Adler, S. S. and et al. *Phys. Rev. Lett.* **96**, 202301 May (2006).

[20] Adams, J. and et al. *Phys. Rev. Lett.* **91**, 072304 Aug (2003).

[21] Adcox, K. and et al. *Phys. Rev. Lett.* **88**, 242301 May (2002).

[22] Adler, S. S. and et al. *Phys. Rev. C* **69**, 034909 Mar (2004).

[23] Abelev, B. I. and et al. *Phys. Rev. Lett.* **97**, 152301 Oct (2006).

[24] Greco, V., Ko, C. M., and Lévai, P. *Phys. Rev. Lett.* **90**, 202302 May (2003).

[25] Fries, R. J., Müller, B., Nonaka, C., and Bass, S. A. *Phys. Rev. Lett.* **90**, 202303 May (2003).

[26] Trainor, T. A. *International Journal of Modern Physics E (IJMPE)* **17**(08), 1499–1540 (2008).

[27] Fries, R. J., Müller, B., Nonaka, C., and Bass, S. A. *Phys. Rev. C* **68**, 044902 Oct (2003).

[28] Greco, V., Ko, C. M., and Vitev, I. *Phys. Rev. C* **71**, 041901 Apr (2005).

[29] Abelev, B. and et al. *Physics Letters B* **655**(34), 104 – 113 (2007).

[30] `http://www.bnl.gov/bnlweb/pubaf/fact_sheet/pdf/trifold_RHIC.pdf`, August (2007). Relativistic Heavy Ion Collider.

[31] `http://www.bnl.gov/bnlweb/pubaf/fact_sheet/pdf/fs_rhic.pdf`, April (2011). The Relativistic Heavy Ion Collider (RHIC).

[32] `http://www.bnl.gov/bnlweb/pubaf/fact_sheet/pdf/fs_rhic_numbers.pdf`, February (2010). RHIC by the Numbers.

[33] Wheeler, G. W. and et al. *Particle Accelerators* **9**, 1 (1979).

[34] Naab, F. and Toader, O. In *11th International Conference on Heavy Ion Accelerator Technology*, WE–14, (2009).

[35] Whitham, K. and et al. In *Particle Accelerator Conference, 1993., Proceedings of the 1993*, 608 –610 vol.1, may (1993).

[36] Alessi, J. and et al. Technical report, Brookhaven National Laboratory Conceptual Design Report BNL-73700-2005-IR, September. Electron Beam Ion Source Pre-injector project (EBIS).

[37] Höltermann, H. and et al. In *AIP Conf. Proc. Electron beam ion sources and traps and their applications: 8th International Symposium*, 165 vol.572, November (2000).

[38] Kponou, A. and et. al. *Rev. Sci. Instrum.* **69**, 1120 (1998).

[39] Pikin, A. and et al. In *JINST International Symposium on Electron Beam Ion Sources and Traps (EBIST2010)*, 5 C09003, September (2010).

[40] Technical report, Brookhaven National Laboratory, October (1988). Booster Design Manual, Rev 1.

[41] Technical report, Brookhaven National Laboratory Associated Universities Inc., December (1966). Alternating Gradient Synchrotron project construction completion report.

[42] Courant, E. D. and Snyder, H. S. *Annals of Physics* **281**, 360 – 408 (2000).

[43] Harrison, M. and et. al. *Annu. Rev. Nucl. Part. Sci.* **52**, 425–469 (2002).

[44] Technical report, Brookhaven National Laboratory Accelerator Division, Collider-Accelerator Department, November (2006). RHIC Relativistic Heavy Ion Collider Configuration Manual.

[45] Harrison, M., Ludlam, T., and Ozaki, S. *Nucl. Instrum. and Methods A* **499**(23), 235 – 244 (2003).

[46] Whitten, C. A. In *AIP Conference Proceedings*, 390, (2008).

[47] Beddo, M. and et al. *Nuclear Instruments and Methods in Physics Research Section A: Accelerators, Spectrometers, Detectors and Associated Equipment* **499**, 725 – 739 (2003).

[48] Anderson, M., , and et al. *Nuclear Instruments and Methods in Physics Research Section A: Accelerators, Spectrometers, Detectors and Associated Equipment* **499**, 659 – 678 (2003).

[49] Llope, W. and et al. *Nuclear Instruments and Methods in Physics Research Section A: Accelerators, Spectrometers, Detectors and Associated Equipment* **522**(3), 252 – 273 (2004).

[50] Fachini, P. and et. al. May (2004). Proposal for a Large Area Time Of Flight System for STAR.

[51] Bonner, B. and et al. *Nuclear Instruments and Methods in Physics Research Section A: Accelerators, Spectrometers, Detectors and Associated Equipment* **508**, 181 – 184 (2003).

[52] Renk, T. *Phys.Rev.* **C87**, 024905 (2013).

[53] Verkerke, W. `http://root.cern.ch/drupal/sites/default/files/roofit_quickstart_3.00.pdf`. RooFit quick start manual.

[54] Verkerke, W. and Kirkby D. `http://roofit.sourceforge.net/docs/roofit_phystat05.pdf`, (2009). RooFit data modeling.

[55] Agakishiev, G. et al. *Phys.Rev.* **C86**, 064902 (2012).

[56] Cacciari, M. and Salam, G. P. *Phys.Lett.* **B641**, 57–61 (2006).

[57] Agakishiev, G. and et al. *Phys. Rev. C* **86**, 064902 Dec (2012).

[58] Adams, J. and et al. *Phys. Rev. C* **72**, 014904 Jul (2005).

[59] Brune, R. and Rademakers, F. `http://root.cern.ch/drupal/content/users-guide`. ROOT User's guide.

[60] R Development Core Team. *R: A Language and Environment for Statistical Computing*. R Foundation for Statistical Computing, Vienna, Austria, (2011). ISBN 3-900051-07-0.

[61] Trainor, T. A. *Phys. Rev. C* **81**, 014905 Jan (2010).

[62] Poskanzer, A. M. and Voloshin, S. *Phys.Rev.* **C58**, 1671–1678 (1998).

[63] Adler, S. et al. *Phys.Rev.Lett.* **91**, 182301 (2003).

[64] Ohlson, A. `http://arxiv.org/abs/1210.8112`, (2012).

[65] Sjostrand, T., Mrenna, S., and Skands, P. Z. *JHEP* **0605**, 026 (2006).

[66] Bahr, M., Gieseke, S., Gigg, M., Grellscheid, D., Hamilton, K., et al. *Eur.Phys.J.* **C58**, 639–707 (2008).

[67] Adams, J. and et al. *Physics Letters B* **616**(12), 8 – 16 (2005).

[68] Trainor, T. In *Proceedings of the XL International Symposium on Multiparticle Dynamics (ISMD 2010)*, 159–164, (2010).